

POINT DEFECTS IN SILICON WITH A TITANIUM DISILICIDE FILM AND  
VACANCY/EXTRINSIC DISLOCATION LOOP INTERACTION

By

SCOTT BRAD HERNER

A DISSERTATION PRESENTED TO THE GRADUATE SCHOOL OF THE  
UNIVERSITY OF FLORIDA IN PARTIAL FULFILLMENT OF THE  
REQUIREMENTS FOR THE DEGREE OF DOCTOR OF PHILOSOPHY

UNIVERSITY OF FLORIDA

1996

Copyright 1996

by

Scott Brad Herner

## ACKNOWLEDGMENTS

This dissertation would not have been possible without help from many persons. The author is indebted to his mentor at Bell Labs, Dr. Hans-J. Gossman. Dr. Gossman not only developed and grew the doping superlattice samples used throughout this study, but also provided many key ideas and motivation for this work. During the author's two visits to Bell Labs (including the full summer of 1995), countless phone calls, and electronic mail, Dr. Gossman gave patient mentoring to a young scientist in many aspects, including lab techniques, the importance of quantifying error, Rutherford Backscattering, and so on. Dr. Gossman edited almost all of the papers that resulted from this work, and, in doing so, taught the author how to write a scientific paper. Dr. Gossman showed remarkable patience and self lessness throughout this work. Thanks are also due to several at Bell Labs, including Dr. John Poate, the chair of the Silicon Processing Department, Dr. Ray Tung, who performed the co-depositions, Dr. Conor Rafferty, who allowed the use of his PROPHET simulation program, and Dr. Henry Luftman, who performed the SIMS analysis. The author thanks Toshi Mogi of Cornell University, who also worked at Bell Labs on nitride films and vacancy diffusivity, for nitriding many samples and many helpful discussions.

At the University of Florida (U.F.), the author is indebted to his advisor, Prof. Kevin Jones, for providing the framework for this project and allowing the author much latitude in the direction it took. Prof. Jones'

enthusiasm for materials science and encouragement helped me maintain my motivation for this work. The author expresses his sincere appreciation to Dr. Wishy Krishnamoorthy for his friendship and advice. Wishy instructed the author in the use of the TEM and the high resolution X-ray system, and constantly offered many techniques in TEM and photo printing from his many years experience. Many ideas and approaches to this work were generated with Wishy, usually over the NY Times crossword and coffee. Wishy also edited many of the papers that came out of this work, as well as this dissertation. The author is grateful to the staff at the MAIC facility at U.F., particularly Eric Lambers for his help with the Auger measurements. The author also thanks lab mates Brent Gila and Ananth Naman for help and instruction on the AFM, and for making life inside and outside the lab more enjoyable. The author is grateful to the members of my committee, particularly Profs. Mark Law and Stephen Pearton, for their help with this dissertation. The authors thank the SEMATECH consortium, the National Science Foundation, and Lucent Technologies, all of which supported this work financially. Lastly, the author must also thank his parents, who continued to support the author's further education and for their unflagging faith during a long college career.

## TABLE OF CONTENTS

	<u>page</u>
ACKNOWLEDGMENTS.....	iii
LIST OF FIGURES.....	vii
LIST OF TABLES.....	xii
ABSTRACT.....	xiii
 CHAPTERS	
1 INTRODUCTION.....	1
1.1 Point Defects and Dopant Diffusion.....	5
1.2 Surface vs. Bulk Generation of Point Defects in Silicon.....	9
1.3 Thin Films and Point Defects.....	12
1.4 Extrinsic Dislocation Loops and Point Defects.....	20
1.5 Approach.....	23
2 SAMPLE PREPARATION AND CHARACTERIZATION TECHNIQUES.....	25
2.1 Doping Superlattices.....	25
2.2 Transmission Electron Microscopy.....	32
2.3 Auger Electron Spectroscopy.....	34
2.4 Atomic Force Microscopy.....	34
2.5 Rutherford Backscattering Spectroscopy.....	35
2.4 Wafer Curvature.....	35
3 POINT DEFECTS IN SILICON WITH A TITANIUM DISILICIDE FILM.....	37
3.1 Introduction.....	37

3.2	Antimony and Boron Diffusion in Silicon with Titanium as a Function of Temperature Annealed for One Hour.....	38
3.3	SIMS Artifacts and Chemo-Mechanical Polishing Procedure.....	49
3.4	Antimony and Boron Diffusion in Silicon with a 30 nm Titanium Film Annealed at 800°C as a Function of Time.....	57
3.5	Antimony and Boron Diffusion in Silicon with Different Thicknesses of Titanium Deposited and Annealed for One Hour at 850°C.....	65
3.6	Antimony and Boron Diffusion in Silicon Annealed at 850°C for One Hour with Co-Deposited Ti + Si or Co + Si .....	74
3.7	Morphology of the films from co-deposition.....	79
3.8	Summary.....	96
4	BEHAVIOR OF EXTRINSIC DISLOCATION LOOPS IN SILICON ANNEALED WITH A TITANIUM DISILICIDE OR SILICON NITRIDE FILM.....	97
4.1	Introduction.....	97
4.2	Antimony and Boron Diffusion Behavior in Ge <sup>+</sup> -implanted Silicon Annealed in NH <sub>3</sub> .....	98
4.3	Dislocation Loop Behavior in Silicon with a Thermally Grown Silicon Nitride Film.....	105
4.4	Dislocation Loop Behavior in Silicon with a Titanium Disilicide Film.....	121
4.5	Summary.....	129
5	CONCLUSIONS AND RECOMMENDATIONS.....	130
5.1	Conclusions.....	130
5.2	Future Work.....	134
	REFERENCES.....	137
	BIOGRAPHICAL SKETCH.....	144

## LIST OF FIGURES

<u>Figure</u>		<u>page</u>
1.1	Schematic of a CMOSFET.....	2
1.2	Various diffusion modes in silicon: (a) interstitial; (b) interstitialcy or "kick out;" and (c) vacancy.....	7
1.3	Estimates of (a) $C^*$ ; and (b) $C^*D^*$ values.....	11
2.1	Diffusivities as a function of temperature and doping level of (a) antimony; and (b) boron. The extrinsic diffusivities assume a doping level of $1 \times 10^{20}/\text{cm}^3$ .....	28
3.1	Cross sectional TEM micrograph of $\text{TiSi}_2/\text{TiO}_x\text{N}_{1-x}$ films on silicon annealed $840^\circ\text{C}/1 \text{ hr}/\text{forming gas}$ .....	41
3.2	Electron diffraction pattern of $\text{TiSi}_2/\text{TiO}_x\text{N}_{1-x}$ films on silicon annealed $840^\circ\text{C}/1 \text{ hr}/\text{forming gas}$ .....	41
3.3	Auger spectra of the sample annealed $800^\circ\text{C}/1 \text{ hr}/\text{forming gas}$ .....	42
3.4	SIMS depth profiles of doping superlattices annealed $840^\circ\text{C}/1 \text{ hr}/\text{forming gas}$ . (a) antimony; and (b) boron.....	44
3.5	Depth profiles of normalized antimony and boron diffusivities in doping superlattices annealed for one hour at various temperatures.....	45
3.6	Comparison of intrinsic diffusivities from the doping superlattices and literature values.....	48

3.7	AFM micrograph of the underlying silicon surface after 30 nm Ti deposition, 800°C/1 hr/forming gas anneal, and removal of the film by chemical etching. The root mean square roughness is 22.0 nm.....	51
3.8	SIMS boron depth profile from the unpolished sample annealed 800°C/1 hr/forming gas: (a) complete (Si lost is from TiSi <sub>2</sub> growth and consequent etching); and (b) detail from figure 3.3a.....	52
3.9	AFM micrograph of the underlying silicon surface after 30 nm Ti deposition, 800°C/1 hr/forming gas anneal, removal of the film by chemical etching, and CMP. The root mean square roughness is 0.1 nm.....	53
3.10	Cross sectional TEM micrograph of dislocation loop layer prior to CMP: (a) before CMP: and (b) after CMP.....	56
3.11	Silicon removal rate with CMP.....	56
3.12	Cross sectional TEM micrograph of TiSi <sub>2</sub> /TiO <sub>x</sub> N <sub>1-x</sub> films on silicon annealed 800°C/600 min/argon.....	59
3.13	Cross sectional TEM micrograph of TiSi <sub>2</sub> /TiO <sub>x</sub> N <sub>1-x</sub> films on silicon annealed 800°C/15 min/argon.....	59
3.14	SIMS depth profiles of antimony doping superlattices annealed 800°C/60 min/argon.....	60
3.15	SIMS depth profiles of antimony doping superlattices annealed 800°C/600 min/argon.....	60
3.16	Depth profiles of normalized antimony diffusivities in doping superlattices with 30 nm of titanium annealed at 800°C for various times.....	61
3.17	Average normalized antimony diffusivities in doping superlattices with 30 nm of titanium annealed at 800°C for various times.....	61
3.18	Gaussian depth profile of vacancies assuming a finite "pulse" of vacancies injected at t = 0.....	64

3.19	RBS spectra (glancing angle) for the co-deposited TiSi <sub>1.8</sub> film with nominal 312 nm Ti thickness before annealing.....	67
3.20	RBS spectra (glancing angle) for the co-deposited TiSi <sub>1.8</sub> film with nominal 4 nm Ti thickness before annealing.....	67
3.21	Cross sectional TEM micrograph of the annealed TiSi <sub>1.8</sub> film with nominal 4 nm Ti thickness.....	70
3.22	Cross sectional TEM micrograph of the annealed TiSi <sub>1.8</sub> film with nominal 312 nm Ti thickness.....	70
3.23	SIMS depth profiles of doping superlattices annealed 850°C/1 hr/argon with nominal 4 nm Ti (a) antimony; and (b) boron.....	71
3.24	Depth profiles of normalized antimony diffusivities in doping superlattices annealed 850°C/1 hr/argon with various thicknesses of Ti .....	72
3.25	Average normalized antimony diffusivities in doping superlattices annealed 850°C/1 hr/argon with various thicknesses of Ti.....	72
3.26	SIMS depth profiles in silicon doping superlattices annealed 850°C/1 hr/argon with 22 nm Ti: (a) antimony; and (b) boron.....	76
3.27	Depth profiles of normalized antimony and boron diffusivities in doping superlattices annealed 850°C/1 hr/argon.....	77
3.28	Cross sectional TEM micrograph of the as-deposited Ti (only) film on silicon.....	82
3.29	Auger electron spectra of the annealed TiSi <sub>0.8</sub> film.....	83
3.30	Auger electron spectra of the annealed TiSi <sub>2.2</sub> film.....	83
3.31	Auger electron spectra of the annealed CoSi <sub>0.8</sub> film.....	84

3.32	Cross sectional TEM micrograph of the annealed CoSi <sub>0.8</sub> film on silicon.....	84
3.33	Cross sectional TEM micrographs of the annealed films: (a) Ti (only) film; (b) TiSi <sub>0.8</sub> film; and (c) TiSi <sub>2.2</sub> film.....	86
3.34	AFM micrograph of the underlying silicon surface after deposition of TiSi <sub>0.8</sub> (30 nm nominal Ti thickness), annealed at 850°/1 hr/argon, and chemically etching off the film.....	88
3.35	Plan view TEM micrographs of the annealed films on the Ti (only) sample: (a) TiO <sub>x</sub> N <sub>1-x</sub> film; and (b) TiSi <sub>2</sub> film.....	89
3.36	Plan view TEM micrographs of the annealed films on the annealed TiSi <sub>2.2</sub> sample: (a) poly Si film; and (b) TiSi <sub>2</sub> film.....	90
3.37	Schematic cross section of the plan view TEM sample.....	92
4.1	SIMS depth profiles of doping superlattices annealed without an implant. (a) antimony; and (b) boron.....	100
4.2	SIMS depth profiles of doping superlattices annealed with an implant. (a) antimony; and (b) boron.....	102
4.3	Normalized antimony diffusivities in loop samples with anneal #2 in NH <sub>3</sub> .....	104
4.4	Cross sectional TEM (bright field, g <sub>220</sub> ) micrograph of the loop layer and silicon nitride film.....	104
4.5	Cross sectional high magnification TEM (bright field, g <sub>220</sub> ) micrograph of the silicon nitride film. Sample has been annealed 910°C/3 hrs/NH <sub>3</sub> .....	108
4.6	Plan view TEM (weak beam dark field, g <sub>220</sub> ) micrographs of samples annealed in various conditions. (a) 910°C/0.5 hr/Ar; (b) 910°C/3 hrs/Ar; (c) 910°C/0.5 hr/NH <sub>3</sub> ; and (d) 910°C/3 hrs/NH <sub>3</sub> .....	109
4.7	Size distributions of the loops in samples annealed in argon. (a) 810°C; and (b) 910°C .....	111

4.8	Size distributions of the loops in samples annealed in NH <sub>3</sub> . (a) 810°C; and (b) 910°C .....	112
4.9	Net interstitials bound by the loops annealed at (a) 810°C; and (b) 910°C.....	113
4.10	Average loop diameter normalized by the area of each loop in samples annealed at (a) 810°C; and (b) 910°C.....	114
4.11	Schematic of the point defect concentrations in loop samples. (a) vacancy; and (b) interstitial.....	117
4.12	Extracted $\frac{C_V}{C_V^*}$ values by the loop method in silicon annealed 910°C/NH <sub>3</sub> for various times.....	118
4.13	Cross sectional TEM (bright field, g <sub>220</sub> ) micrograph of the loop layer and TiSi <sub>2</sub> film.....	123
4.14	Plan view TEM (weak beam dark field, g <sub>220</sub> ) micrographs of the loops annealed at various times. (a) no film, 890°C/1 hr/forming gas; (b) no film, 890°C/4 hrs/forming gas; (c) TiSi <sub>2</sub> film, 890°C/1 hr/forming gas; and (d) TiSi <sub>2</sub> film, 890°C/4 hrs/forming gas.....	125
4.15	Net interstitials bound by the loops annealed at (a) 840°C; and (b) 890°C.....	126
4.16	Extracted $\frac{C_V}{C_V^*}$ values by the loop method in silicon with 30 nm titanium annealed for various times and temperatures in forming gas.....	128

## LIST OF TABLES

<u>Table</u>		<u>page</u>
1.1	Device dimensions for generations of ICs.....	3
1.2	Review of studies of point defects in silicon with a TiSi <sub>2</sub> film.....	21
3.1	Film properties with thickness variation.....	69
3.2	Surface roughness measurements of the annealed co-deposited samples.....	87
3.3	Residual wafer curvature of the annealed co-deposited films.....	91
4.1	Sample description for section 4.2.....	99
4.2	Comparison of point defect values measured by the loop method and antimony diffusion.....	116
4.3	Comparison of point defect values in silicon annealed with a TiSi <sub>2</sub> film measured by the loop method and antimony diffusion.....	127

Abstract of Dissertation Presented to the Graduate School  
of the University of Florida in Partial Fulfillment of the  
Requirements for the Degree of Doctor of Philosophy

POINT DEFECTS IN SILICON WITH A TITANIUM DISILICIDE FILM AND  
VACANCY/EXTRINSIC DISLOCATION LOOP INTERACTION

By

Scott Brad Herner

December 1996

Chairman: Professor Kevin S. Jones

Major Department: Materials Science and Engineering

The concentration of native point defects in silicon determines the diffusivity of substitutional dopant atoms. This concentration can be changed by the deposition or formation of thin films on a silicon substrate. In this dissertation, the concentration of native point defects in silicon with a titanium disilicide ( $TiSi_2$ ) film is studied. The two methods used to trace native point defect concentrations are dopant diffusion and the kinetics of extrinsic dislocation loops. Secondary ion mass spectrometry was used to monitor the diffusion of antimony (Sb) and boron (B) silicon doping superlattices. The diffusivity of antimony (boron) is proportional to the relative concentration of vacancies (interstitials). The extracted diffusivities of these dopants showed that silicon annealed with a  $TiSi_2$  film results in a relative vacancy supersaturation and an interstitial undersaturation. Three proposed mechanisms for how the  $TiSi_2$  film effects the change in native point

defect concentrations were investigated. Volume contraction at the interface, stress compensation, and the diffusing species during film growth were all found not to be significant factors in the point defect perturbation.

The behavior of extrinsic dislocation loops in silicon with a  $\text{TiSi}_2$  or  $\text{SiN}_x$  film was also investigated. Vacancy combination with extrinsic dislocation loops was found to be mostly diffusion rate limited and not reaction rate limited, showing the loops are sensitive detectors of vacancy supersaturations. End-of-range (EOR) loops were formed in silicon after an amorphizing  $\text{Ge}^+$  implant and re crystallizing anneal. Samples were further annealed with a Ti film in forming gas or in  $\text{NH}_3$ , which formed  $\text{TiSi}_2$  or  $\text{SiN}_x$  films, respectively. Transmission electron microscopy (TEM) analysis showed that samples annealed with either film resulted in enhanced dissolution of the loops compared to samples annealed without a film. The enhanced dissolution is attributed to combination of the excess of vacancies with the loops. Extraction of the relative supersaturation of vacancies in silicon with a  $\text{TiSi}_2$  or  $\text{SiN}_x$  film from loop measurements is in good agreement with measurements from antimony diffusion in doping superlattices.

## CHAPTER 1

### INTRODUCTION

The relentless advance in the manufacture of silicon integrated circuits (ICs) has allowed the industry to reduce the size of the transistor by a factor of two every three years or less, a pace that was described by Gordon Moore more than 20 years ago and has become known as Moore's Law. These advances in chip manufacturing have been accompanied by a high degree of complexity: an advanced IC in 1996 requires over 200 processing steps and has five or more layers of metallization. Each new generation of logic chips requires advances in materials processing that allows both economical fabrication and improved function.

Modern chips are based on complementary pairs of metal oxide semiconductor (CMOS) transistors. These CMOS circuits are the main transistor type in both memories and processors. Figure 1.1 shows a schematic of a typical metal oxide field effect transistor (MOSFET) with dimensions for 0.25  $\mu\text{m}$  gate lengths, which is state-of-the-art in 1996.<sup>1</sup> The gate region of the transistor, in which the flow or absence of flow of charge carriers from the source to drain defines the device as being "on" or "off," has been the defining length for each new generation of chips, although there are several critical dimensions. The junction depth defines the doped region of the chip where the material changes from p to n type, and vice versa. The cross sectional area of this junction, along with the intrinsic resistivity of the

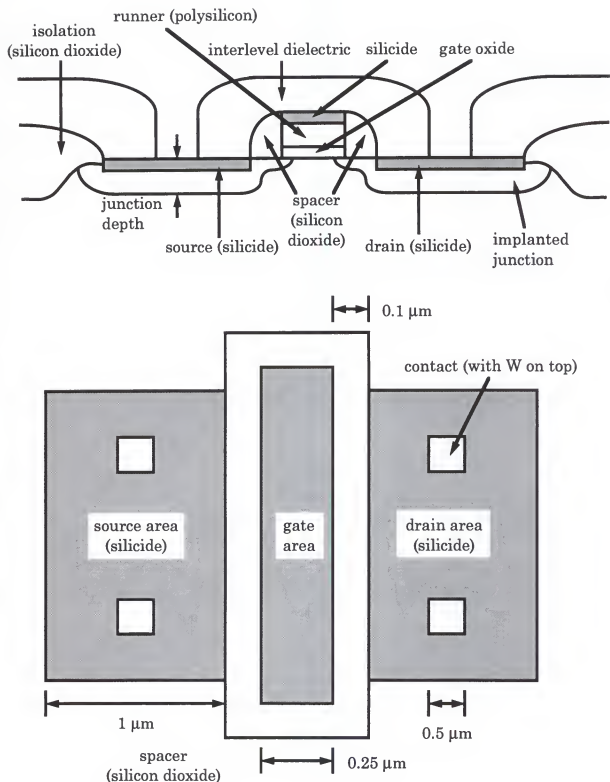


Figure 1.1. Schematic of a CMOS FET.<sup>1</sup>

material, defines the resistance to flow of current from the source to the drain. Table 1.1 shows critical dimensions for each successive generation of logic chips, as projected by the 1994 Semiconductor Industry Association Roadmap.<sup>2</sup>

Table 1.1. Critical device dimensions for generations of integrated circuits.

gate length (μm)	junction depth (μm)	bits/chip (DRAM)	year production
0.50	0.20	16 M	1992
0.35	0.15	64 M	1995
0.25	0.12	256 M	1998
0.18	0.10	1 G	2001
0.12	0.08	4 G	2004

As gate lengths decrease from 0.5 μm to 0.12 μm in 2007, junction depth must also decrease from 0.2 to 0.08 μm. The critical dimensions of the transistor must be reduced to maintain price (by increasing yield) and performance improvements that have come to be expected.

The enormity of this task has employed scientists and engineers from many disciplines. Material scientists play a key role in this enterprise by providing improvements in materials and processing. Defects in silicon, including point, line, and volume defects, have been and will continue to be a leading pre-occupation of material scientists in this endeavor. Understanding the origin, stability, and dissolution of these defects, their relationship to each other, and their relationship to the varying steps in processing and final

device performance will allow the industry to continue to provide the advanced ICs expected by the world.

Two of these kinds of defects, native point defects and dislocation loops, are of particular interest and will be the subject of this dissertation. The term native, or intrinsic, point defects is used to distinguish silicon from other possible point defects, such as a dopant. Native point defects, namely silicon vacancies and self interstitials, are the main contributors to dopant diffusion in silicon.<sup>3</sup> One factor that limits scaling is an understanding of dopant diffusion. Extrinsic dislocation loops are an agglomeration of silicon self-interstitials. They commonly form during source/drain fabrication. These loops can serve as sources and sinks for point defects, and if they occur in the active region of devices, can severely degrade device performance.<sup>4</sup> The study of both kinds of these defects and their interaction is thus of extreme practical importance.

With increasing chip complexity, it has become increasingly cost intensive to do a matrix of experiments with one variable in each step of the process. The semiconductor industry in general and researchers specifically have therefore turned to computer simulation programs to model and understand such processes as dopant diffusion. As computing power is cheap relative to human labor and capital equipment, these simulators provide an attractive alternative. However, these simulators can only predict diffusion solutions for unknown phenomena (e.g., smaller device dimensions) when the models are physically based. Information on the nature of native point defects produced during various steps of the fabrication process as well as interaction with extended defects from previous steps must be provided to maintain this physical basis. This can only be done with physical experimentation. It is the goal of this dissertation to provide that physical

basis in one area of processing, namely, the formation of a TiSi<sub>2</sub> ohmic contact, as well as information on the interaction between point defects and extrinsic dislocation loops.

### 1.1 Point Defects and Dopant Diffusion

During the early years of silicon IC fabrication, dopant diffusion in silicon was described macroscopically in the same way that most solid state diffusion processes are described, namely by Fick's second law:

$$\frac{\delta C(z, t)}{\delta t} = -D \frac{\delta^2 C(z, t)}{\delta (z)^2} \quad (1.1)$$

where C is the concentration of diffusing atoms, z is the distance, t is the time, and D is the diffusing constant, or diffusivity. Fick's second law began to be violated as silicon devices diminished in size. A study of diffusion in homojunction bipolar transistors, which are formed by multiple overlapping implants in silicon, displayed what was called the "emitter push effect."<sup>5</sup> The diffusion of one dopant was found to enhance the diffusion of the other dopants by the creation of non equilibrium concentrations of native point defects, namely vacancies (V) and self-interstitials (I).

Through many experiments, the diffusion of dopants in silicon have been shown to be mediated by native point defects. In the vacancy diffusion mechanism, a substitutional dopant atom exchanges position with an empty lattice site as it traverses through the material. In the interstitial mechanism, a dopant atom hops from one interstitial site to another. A variant of the interstitial mechanism is the interstitialcy, or "kickout"

mechanism. The interstitialcy process involves the "kickout" of a dopant atom by a silicon self-interstitial, which then diffuses to another lattice site and kicks out the lattice silicon atom. A schematic of these three processes is shown in figure 1.2. As it is impossible to distinguish between the interstitial and interstitialcy mechanisms, these two processes shall henceforth be referred to as "interstitial" mechanism.<sup>3</sup>

Dopants that occupy silicon lattice sites, such as antimony (Sb) and boron (B), have four bonds with silicon and, as such, can only move if there is a defect present. Therefore, the native point defect concentration controls the rate of diffusion. For a dopant atom A, the diffusivity can be expressed as:

$$D_A = D_{AI} + D_{AV} \quad (1.2)$$

where  $D_{AI}$  and  $D_{AV}$  represent the interstitial and vacancy components for diffusion. If  $D_A$  is defined to be the diffusivity under nonequilibrium point defect concentrations, and  $D_A^*$  is the diffusivity at equilibrium conditions, equation (1.2) can be expressed as:

$$\frac{D_A}{D_A^*} = \frac{D_{AV}}{D_A^*} + \frac{D_{AI}}{D_A^*} \quad (1.3)$$

Equation (1.3) can be rewritten as:

$$\frac{D_A}{D_A^*} = \frac{D_{AV}^*}{D_A^*} \frac{D_{AV}}{D_{AV}^*} + \frac{D_{AI}^*}{D_A^*} \frac{D_{AI}}{D_{AI}^*} \quad (1.4)$$

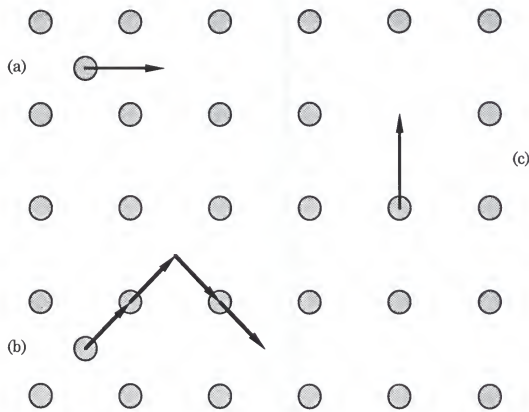


Figure 1.2. Various diffusion modes in silicon: (a) interstitial; (b) interstitialcy or "kick out," and (c) vacancy.

where  $\frac{D_{AV}^*}{D_A^*}$  is the fraction of atom A's diffusivity that occurs through the

vacancy mechanism under inert ambient conditions and  $\frac{D_{AI}^*}{D_I^*}$  is the fraction of

A's diffusivity that occurs through the interstitial mechanism. Defining  $\frac{D_{AV}^*}{D_A^*} = f_{AV}$  and  $\frac{D_{AI}^*}{D_A^*} = f_{AI}$ , then equation 1.4 becomes:

$$\frac{D_A}{D_A^*} = f_{AV} \frac{D_{AV}}{D_{AV}^*} + f_{AI} \frac{D_{AI}}{D_{AI}^*} \quad (1.5)$$

where  $f_{AI} = 1 - f_{AV}$ . Since  $\frac{D_{AV}^*}{D_A^*}$  and  $\frac{D_{AI}^*}{D_A^*}$  are proportional to the relative

concentration of each kind of native point defect, i.e.  $\frac{D_{AV}}{D_{AV}^*} \propto \frac{C_V}{C_V^*}$  and  $\frac{D_{AI}}{D_{AI}^*} \propto \frac{C_I}{C_I^*}$ , where  $C_V$  ( $C_I$ ) is the concentration of vacancies (interstitials) and  $\frac{C_I}{C_I^*}$

denotes equilibrium, equation (1.5) can be rewritten as:

$$\frac{D_A}{D_A^*} = f_{AV} \frac{C_V}{C_V^*} + f_{AI} \frac{C_I}{C_I^*} \quad (1.6)$$

Good approximations for  $f_{AV}$  and  $f_{AI}$  for many dopants have been obtained at high temperatures ( $> 1000^\circ\text{C}$ ) where I-V recombination is efficient. By saturating silicon with vacancies or interstitials by nitridation or oxidation, respectively, one kind of defect can be effectively eliminated by recombination and solutions for  $f_{AV}$  and  $f_{AI}$  can be obtained under these conditions. Reasonable estimates of these values have been made for most of the common dopants in silicon.<sup>3</sup> Antimony has been found to diffuse by a pure

vacancy mechanism ( $f_{SbV} \sim 1$  and  $f_{SbI} \sim 0$ ), while boron's diffusivity is dominated by an interstitial mechanism ( $f_{BI} \sim 0.8$  to 1.0).<sup>6,7</sup> These dopant species can now be used as indicators of the relative population of point defects. By observing changes in the diffusivities of these dopants in doping-superlattices (DSLs), one can obtain depth profile information of silicon vacancies (Sb) and self interstitials (B).<sup>8</sup> Direct observation of point defects in silicon by a method such as transmission electron microscopy is impractical. Another method, positron annihilation analysis, requires a nuclear power source and yields information on only vacancies.<sup>9</sup> Development of indirect methods, such as observation of dopant diffusion or the behavior of extended defects, are the only practical means of observing point defects.

### 1.2 Surface vs. Bulk Generation of Point Defects in Silicon

A brief discussion of the origin of point defects in bulk crystals without films is warranted, though this topic is not examined explicitly in this dissertation. Point defect annihilation ( $I + V \rightarrow 0$ ) as it applies to this work will be discussed in more detail in chapter three. Since the relative point defect concentrations,  $\frac{C_V}{C_V^*}$  and  $\frac{C_I}{C_I^*}$ , will be measured in chapter three,

knowledge of  $C_V^*$  and  $C_I^*$  values is not required. In chapter four, the value of  $C_V D_V$  will be measured, requiring an estimate of  $C_V^* D_V$  to extract an estimate of  $\frac{C_V}{C_V^*}$ . It is therefore instructive to review the relative point defect

equilibrium concentrations and estimates of  $C^* D$  values. Several estimates that vary over several orders of magnitude have been made of equilibrium native point defect concentrations and the concentration-diffusivity products.<sup>7,10-15</sup> In this dissertation, the  $C_V^* D_V$  estimates of Tan and Gösele<sup>7</sup>

will be used, and their estimates of this value and  $C_I^*D_I$ ,  $C_V^*$ , and  $C_I^*$  are plotted in figure 1.3 for reference. The Tan and Gösele estimates are one of the only sources that treat both vacancy and interstitial parameters in a self consistent manner, and in the author's opinion represents the most complete set of native point defect parameters available. Other estimates of individual native point defect parameters, such as  $D_V^*$ , will be drawn from other sources when that source is believed to be more accurate than the Tan and Gösele estimate. With a density of  $5 \times 10^{22}$  silicon atoms/cm<sup>3</sup>, it is interesting to note that such small concentrations of defects as shown in figure 1.3 are able to be a major influence on dopant diffusion.

The most obvious way to generate native point defects is for a silicon atom to move from a substitutional site to an interstitial site, creating a vacancy and an interstitial, or a Frenkel pair ( $I + V \leftrightarrow 0$ ). However, this involves breaking four silicon bonds and bending the bonds around both the vacancy and interstitial. It has been estimated that this requires 12-15 eV, making the possibility of point defect generation by Frenkel pair generation unlikely, or at least an inefficient source of native point defects.<sup>3</sup>

Since a finite concentration of native point defects exists in thermal equilibrium to minimize the free energy of the silicon lattice due to entropy, and no extended defects are present, native point defects must be generated at the crystal surface. A silicon atom can move from the surface to an interstitial site in the bulk to create an interstitial, and a bulk substitutional atom can move from the bulk to a surface site to create a vacancy. These defects can then diffuse from the near surface region to the bulk. Native point defects can also recombine at the surface. A recent study by Fang et al.<sup>16</sup> made qualitative estimates of the relative contributions of surface and bulk generation of native point defects. They employed box-shaped boron marker

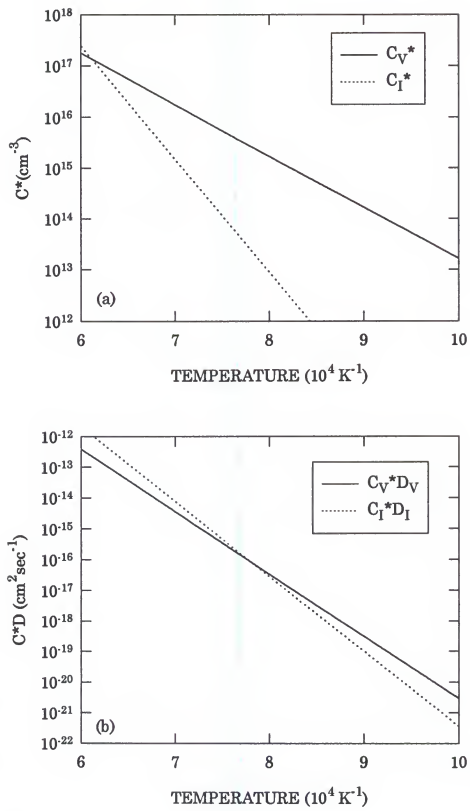


Figure 1.3. Estimates of (a)  $C^*$  values; and (b)  $C^*D^*$  values.<sup>7</sup>

layers in silicon that were isolated from native point defects from one side (depth wise) by dislocations that served as interstitial sinks. This allowed a determination of the relative contribution to the native point defect concentration of surfaces, oxygen precipitates, and bulk Frenkel pair generation. They found that surfaces and interfaces contribute far more to native point defect generation than bulk Frenkel pair generation.

Since the surface of silicon is, in all cases except for vacuum anneals, covered by a native oxide film of perhaps 2 nm thickness, the word "surface" in the discussion above can be replaced with "interface." This distinction is important since practically all measurements of equilibrium concentrations of native point defect parameters have been performed with a native oxide present. This dissertation will implicitly assume that measurements with a native oxide present, such as annealing silicon in an argon ambient, represent equilibrium measurements. One could alternately choose vacuum anneal measurements as equilibrium, since the low partial pressure of O<sub>2</sub> in a vacuum at high temperatures results in the desorption of the SiO<sub>2</sub> film via the intermediate formation of SiO, which then volatizes.<sup>17,18</sup> The scarcity of measurements done with vacuum anneals makes this impractical, but it is important to keep this fact in mind when discussing equilibrium concentrations of native point defects in silicon with other films, such as titanium disilicide.

### 1.3 Thin Films and Point Defects

There are several sources and sinks for native point defects in silicon, including high concentration diffusion,<sup>3</sup> ion implantation,<sup>19</sup> thin films,<sup>20-22</sup> extended defects,<sup>23,24</sup> and precipitates.<sup>16</sup> Ion implantation has been the

source of most technological interest because it results in an effect known as transient enhanced diffusion (TED). During ion implantation, energetic ions collide with silicon atoms and knock them off their lattice sites through momentum transfer. This creates a vacancy and an interstitial in the crystal for each atom knocked off its site. The interstitials can then transfer momentum to other atoms before coming to rest in the lattice, creating a damage cascade. This creates a supersaturation of vacancies and interstitials. With sufficient dose and energy, enough damage can accumulate to produce an amorphous layer at the surface of the crystal.<sup>25</sup> The projected range of the ions correlates with the depth of the amorphous layer. The two native point defect depth concentration profiles are spatially separated: vacancies are created near the surface and are essentially motionless during the implantation, while interstitials are concentrated deeper in the crystal due to momentum transfer.<sup>26</sup> The greater supersaturation of interstitials compared to vacancies is attributed to the simple fact that the implantation results in "excess" atoms added to the crystal that either become interstitials themselves or displace silicon atoms, which become native interstitials ("+1 model").<sup>26</sup> The high concentration of native point defects created by implantation increases the rate of Frenkel pair recombination during the subsequent anneal. Most of the native point defects created, excepting an amount of interstitials roughly equivalent to the implanted dose, are therefore rapidly annihilated, leaving an interstitial supersaturation when the vacancy concentration returns to equilibrium values. Also, the fact that the vacancies are concentrated closer to the surface means that they can rapidly recombine at the surface during annealing whereas the interstitials are further away from the surface and have a smaller probability of surface recombination.<sup>27</sup>

The supersaturation of interstitials creates greatly enhanced diffusion of boron (TED), which has a relatively high diffusivity among the common dopants in Si and is also the most common dopant for p type sources and drains. Transient enhanced diffusion has begun to limit device performance. The reverse short channel effect describes the anomalous increase in the shut off voltage for MOSFETS. The shut off voltage is a direct function of, among other parameters, the amount of dopants in the substrate region beneath the gate (figure 1.1). When a supersaturation of interstitials causes dopants to diffuse into this region, the effective gate length is shortened, increasing the shut off voltage. This has an undesirable effect on device performance.<sup>28</sup>

Other native point defect sources besides ion implantation can have a significant effect on dopant diffusion. Even subtle diffusion effects can have detrimental implications for predicting and controlling dopant profiles. The diffusion of phosphorus (a dopant in silicon) has been shown to create interstitials.<sup>3</sup> Arsenic clustering, which occurs at high concentrations exceeding the solid solubility, results in the emission of interstitials and arsenic precipitation results in the emission of vacancies.<sup>29</sup> Interfaces that arise from thin films that are in intimate contact with highly doped regions can influence the native point defect population, and thus dopant diffusion. As the main topic of this dissertation is changes in point defect population due to thin films, previous results in this subject will be henceforth discussed in greater detail.

### 1.3.1 Silicon Dioxide Thin Films

Silicon dioxide ( $\text{SiO}_2$ ) thin films are typically used in silicon integrated circuits for lateral device isolation, dielectric thin films, and as masks for ion

implants. Many studies have shown that thermal oxidation results in a supersaturation of interstitials and an undersaturation of vacancies in the bulk.<sup>3,20,21,30-32</sup> An estimate of  $\frac{C_I}{C_I^*} \sim 13$  after dry oxidation of silicon for 1

hour at 900°C was made by Packan and Plummer,<sup>20</sup> and is in line with other estimates. They found that the amount of interstitial supersaturation correlated well with the velocity of oxide growth.

Despite a large body of literature on the subject, a proven mechanism for why silicon dioxide thin films inject interstitials is lacking. Four proposed mechanisms for this behavior are briefly reviewed here: (1) Hu<sup>30</sup> proposed that during thermal oxidation, a small amount of the silicon ( $\sim 10^{-3}$ ) available is not oxidized. These "unoxidized" silicon atoms are then displaced from their lattice sites by the advancing  $\text{SiO}_2/\text{Si}$  interface, becoming interstitials. The interstitials assume substitutional sites at the interface only if there are kinks at the surface sites, which plausibly explains the dependence of the growth of stacking faults with the orientation of the substrate during oxidation that Hu observed. Stacking faults are interstitial extended defects that arise from an interstitial supersaturation. Planes with fewer kink sites such as {111} produced larger stacking faults than {100} planes. (2) Tan and Gösele<sup>33</sup> proposed that the volume increase associated with  $\text{SiO}_2$  growth ( $\sim 120\%$ ) is accommodated by viscoelastic flow of the  $\text{SiO}_2$  at the interface. This flow is driven by a compressive plane stress which gives rise to the supersaturation of interstitials. A detailed mechanism of how this stress generates the interstitials was not reported. (3) Tiller<sup>31</sup> proposed that oxidation initially occurs as a "...transitory crystalline layer containing interstitial species." These interstitials are then ejected into the bulk silicon instead of  $\text{SiO}_2$  due to their lower free energy in silicon. (4) Dunham and

Plummer<sup>32</sup> proposed that interstitials created by the oxidation process are accumulated in  $\text{SiO}_2$  near the interface due to the slow diffusivity of interstitials in  $\text{SiO}_2$ . These interstitials then diffuse into the bulk silicon due to imbalances between the rate of interstitial creation and the flux of interstitials into the oxide. Unfortunately, it is impossible with current techniques to prove or disprove any of these mechanisms. A variant of Tan and Göseles' mechanism in silicon with an  $\text{SiO}_2$  film is tested in silicon with a  $\text{TiSi}_2$  film and is discussed in detail in chapter three.

### 1.3.2 Silicon Nitride Thin Films

Silicon nitride ( $\text{SiN}_x$ ) thin films are also used as isolation materials and masks in addition to  $\text{SiO}_2$ . Although less studied in the area of native point defects than silicon dioxide thin films, it has been shown that silicon nitride films result in a vacancy supersaturation and an interstitial undersaturation in the underlying silicon substrate.<sup>21,34-36</sup> An estimate of  $\frac{C_V}{C_V^*} \sim 4$  after thermal nitridation in  $\text{NH}_3$  after 1 hour at  $910^\circ\text{C}$  was measured

by Mogi et al.<sup>36</sup> It is important to keep the relative effects of oxide and nitride films on native point defect concentrations in mind when discussing the effect of  $\text{TiSi}_2$  films.

Two mechanisms have been proposed to account for this behavior: (1) Ahn et al.<sup>21</sup> proposed that stress in deposited  $\text{SiN}_x$  films (on both sides of the substrate) was relieved by silicon atom migration into the film. As the film becomes more silicon-rich, stress in the stretched silicon nitride network is relieved. They postulated that these migrating silicon atoms leave behind a vacancy, creating the observed supersaturation. The silicon

absorption/vacancy generation rate is then a function of stress in the  $\text{SiN}_x$  films, and the stress was found to be a strong function of composition. (2) Osada et al.<sup>35</sup> proposed that the tensile nitride film stress leaves the region of the substrate near the interface in compression. This compressive stress is then relieved by the generation of Frenkel pairs at the interface, which can have lower energies of creation than Frenkel pairs generated in the bulk due to the irregular bond network at the interface. They posited that vacancies diffuse into the substrate, increasing the lattice parameter and relieving the compressive stress, and interstitials diffuse into the film, relieving its' tensile stress. Thicker films deposited on only one side of the substrate result in larger stresses, resulting in greater vacancy supersaturations. The mechanism of Osada et al. for native point defect generation in silicon with a silicon nitride film is tested in silicon with a titanium disilicide film. Silicon nitride and titanium disilicide films are both in tension on silicon at elevated temperatures and result in the same type of point defect perturbation.

### 1.3.3 Titanium Disilicide Thin Films

Titanium disilicide has become the ohmic contact of choice for many CMOS applications at  $0.5 \mu\text{m}$  gate lengths and smaller. It has several advantages over single metal or metal alloys, despite having a higher resistivity than many of them. As junction depth decreases, the total resistance of the contact increases since there is a limit to the number of dopants that are soluble in a given volume of silicon. By depositing titanium on the source and drain regions and annealing,  $\text{TiSi}_2$  is formed. Since this process results in the silicide being below the plane of the surface of the wafer, it is known as a self aligned silicide, or salicide. This silicide shunts the

resistance of the doped silicon and is less sensitive to lithographic misalignment tolerances. The solid solubility of titanium in silicon is very low and therefore does not interfere with the semiconducting properties.<sup>2</sup> This is in contrast to aluminum contacts, which aluminum and silicon are soluble in one another, leading to the well known problem of "spiking" into the silicon substrate. Titanium can reduce  $\text{SiO}_2$ , which means perfect cleaning of the native oxide prior to metal deposition is not critical. Titanium disilicide is also stable at elevated temperatures (to 800°C) and can "self passivate," forming a protective  $\text{SiO}_2$  surface barrier that prevents further attack during processing.<sup>37</sup>

Three potential problems with using  $\text{TiSi}_2$  are worthy to note. The desired low resistivity C54 phase of  $\text{TiSi}_2$  forms only after several precursor phases form, including the high resistivity C49 phase. It has been shown that the C49 to C54 phase transition temperature increases as the thickness of  $\text{TiSi}_2$  decreases, portending a potential scaling limit for  $\text{TiSi}_2$ .<sup>38</sup> However, significant progress has been made in lowering this transition temperature in the past year, and it appears this problem is well on its way to being solved.<sup>39,40</sup> Another problem is the rough interface, or thermal "grooving," that is typically produced by titanium silicidation. The elements in the polycrystalline  $\text{TiSi}_2$  film diffuse to present low energy interfacial planes in each of the grains to silicon. These planes are those that produce epitaxial, or as close as possible to epitaxial, relationships between the substrate and film. For silicon, these  $\text{TiSi}_2$  planes are parallel to the (111) planes.<sup>41</sup> For long or high temperature annealing, this will finally result in islanding of the film. The trend toward lower thermal budgets appears to be reducing this problem.

A third area which has been of much debate is how the formation and anneal of a  $\text{TiSi}_2$  contact affects the diffusion of dopants underneath. This problem is of keen interest, as the contacts are in intimate contact with the heavily doped source and drain regions, and limitation of dopant diffusion is critical to maintain shallow junctions. A determination of the change in native point defect concentrations in silicon, if at all, during and after the formation of a  $\text{TiSi}_2$  film will be the main area of discussion in this dissertation. It is also important to understand the mechanism by which the film effects this change if the process physics community is to develop dopant diffusion simulators that are truly predictive in their capability. A recent report by Honeycutt and Rozgonyi<sup>42</sup> estimated that  $\text{TiSi}_2$  formation at 800°C for 5 minutes caused a vacancy supersaturation on the order of  $\frac{C_V}{C_V^*} \sim 10^7$ ,

measured by antimony diffusion in a buried marker layer in the substrate. If true, this result would have grave implications for dopants that have even a small component of their diffusivity determined by the vacancy concentration. Other studies have also found changes in dopant diffusivity in silicon with a  $\text{TiSi}_2$  film.<sup>43,44</sup> Some authors have examined the influence of  $\text{TiSi}_2$  films on buried dopant marker layers and found no enhanced or retarded diffusion, leading them to conclude that  $\text{TiSi}_2$  does not change the point defect concentration by a measurable amount.<sup>45,46</sup> Still others have examined the behavior of extrinsic dislocation loops in silicon underneath a  $\text{TiSi}_2$  film and found that  $\text{TiSi}_2$  either greatly enhances their dissolution,<sup>47-53</sup> or has little or no effect on them.<sup>54-55</sup> Another study using deep level transient spectroscopy (DLTS) found that  $\text{TiSi}_2$  formation resulted in the removal of defects in the underlying silicon substrate, and this removal was believed to be due to a vacancy injection from the film.<sup>56</sup> These studies have different conclusions on

the type and magnitude of the effect that  $\text{TiSi}_2$  has on point defect concentrations in silicon. The varying studies are listed in Table 1.2. Three proposed mechanisms for point defect generation in silicon with a  $\text{TiSi}_2$  film are discussed in detail in chapter three.

It is significant to note that Wittmer et al.<sup>57</sup> has postulated that the formation of  $\text{Pd}_2\text{Si}$ , a transition metal silicide used for Schottky contacts in silicon, can cause anomalous diffusion of dopants in silicon based on large enhancements found in the diffusivity of antimony. They found that after only a 10 minute anneal at 250°C, buried antimony marker layers had shown significant asymmetric diffusion (towards the  $\text{Pd}_2\text{Si}$  film and not on the "backside" of the doping spike), which would indeed be anomalous. Antimony is a relatively slow diffuser in silicon, with an estimated  $\sqrt{4D_{\text{Sb}}^{\text{int}} t}$  diffusion length of 1.5 nm after 1 hour at 800°C, not measurable with the resolution of most secondary ion mass spectrometry (SIMS) instruments.<sup>58</sup> Therefore significant diffusion at 250°C would indeed be anomalous. As will be shown in chapter three, this measurement as well as the aforementioned one by Honeycutt and Rozgonyi<sup>42</sup> are the result of SIMS depth profiling errors caused by sputtering through the rough interface. To the author's knowledge, the SIMS measurements in this dissertation were the first to eliminate artifacts arising from the rough  $\text{TiSi}_2/\text{Si}$  interface by chemically etching off the silicide and chemo-mechanical polishing the silicon surface prior to SIMS analysis.

#### 1.4 Extrinsic Dislocation Loops and Point Defects

Extrinsic dislocation loops are metastable extended defects consisting of interstitial silicon atoms. They can arise from amorphizing implants of a

Ti thickness	post dep. anneal	characterization	result	yr.	ref.
37 nm	600°C 10, 35, 150 min	RBS of As dopant	no redistribution of As in the bulk	'84	45
30-100 nm	400-1100°C 10 sec	RBS of As dopant	As snowplow but no enhanced diffusion	'86	46
30 nm	600-650°C 10 sec	XTEM of loops	elimination of loops	'87	47
30 nm Ti with 10 nm Si cap	500-1000°C 1 hour	XTEM of loops	loops reduced	'88	49
30 nm	600°C 20 sec	SIMS B and As dopants	TiSi <sub>2</sub> is a B and As sink, enhanced diff. of B	'88	43
	600-1050°C 10 sec	XTEM of loops	elimination of loops	'89	49
30 nm	600-650°C 10 sec	XTEM of loops	elimination of loops	'89	48
30 nm	800-850°C 10 sec	XTEM of loops	elimination of loops	'89	50
30 nm	600-1000°C 1 hr	XTEM of loops	reduction of loops	'89	51
50 nm Ti + 50 nm Si cap	400-1000°C 1 hr	XTEM of EOR loops	no change	'89	
not given	1100°C 1 sec	PTEM of loops	EOR loops reduced	'91	53
Ti + Si cap	650°C/30 min @ 700, 900, or 1050°C/10 sec	DLTS spectra	removal of defects	'91	56
23 nm	900°C 5 min	PTEM of loops	EOR loops reduced	'92	52
18 nm	650°C 120 sec	SIMS B and As dopants	enhanced diffusion of B and As	'92	44
5 or 30 nm on Si <sub>x</sub> Ge <sub>1-x</sub>	650°C/20 sec + 850 or 900°C/20 sec	PTEM of loops	elimination or reduction of all defects	'95	54
30 nm	700°C 20 min + 890°C 1 hr	PTEM of loops	EOR loops reduced	'96	55

Table 1.2. Review of studies of point defects in silicon with a TiSi<sub>2</sub> film.

neutral species such as germanium, which is often used to reduce channeling of subsequently implanted dopants.<sup>59</sup> Upon recrystallizing/activating anneals, loops form near the end-of-range (EOR) of the amorphizing implant, hence the term EOR loops. These loops are due to the interstitial supersaturation that is believed to arise from implants and recoils.<sup>4</sup> Another source of loops after implantation is from exceeding the solid solubility of an implanted dopant, which can result in an interstitial supersaturation and very high levels of stress in the substrate upon precipitation. Dislocation loops can act as a source of interstitials when silicon is annealed at high enough temperatures ( $> 900^{\circ}\text{C}$ ) that the loops become thermally unstable and begin to release interstitials into the bulk. They can also act as sinks, gettering interstitials at lower temperatures.<sup>60</sup> This gettering process is due to the difference in strain between a "free" interstitial and one that is bound by the dislocation loop.<sup>61</sup> As will be shown in this dissertation, they can also act as a sink for vacancies, resulting in loop dissolution. By changing the concentration of native point defects, they can affect dopant diffusion.

Extrinsic dislocation loops have been shown to grow under interstitial supersaturations from ion implantation and oxidation.<sup>60,62</sup> Loops can also act as "detectors" of native point defect fluxes, which can complement the information gained from measuring dopant diffusion.<sup>63</sup> Little quantitative work has been done on loop dissolution due to a supersaturation of vacancies. In this dissertation, we examine the nature of the reaction between a vacancy and an extrinsic dislocation loop, i.e. diffusion limited vs. reaction rate limited is examined. By observing dislocation loop dissolution in samples with a thin film source of vacancies, silicon nitride or titanium silicide, and comparing to loops in control samples that are annealed without a film, measurements of CyDy values in silicon with a thin film are extracted. With

an estimate of  $C_V^* D_V$ , an estimate of  $\frac{C_V}{C_V^*}$  can be made with the loop

measurements. By using the same experimental procedures to produce a point defect perturbation in silicon, the  $\frac{C_V}{C_V^*}$  values extracted from the methods

of dopant diffusion and loops can be directly compared. This is the first known directly comparable data set of point defect concentrations extracted from two different physical phenomena using the same wafer processing. It will be shown that these measurements produce excellent agreement.

### 1.5 Approach

This dissertation is divided into two main sets of experimental results. In the first set of results, the effect of titanium disilicide films on dopant diffusion in the silicon substrate is characterized and three possible mechanisms for the point defect perturbation are studied: (1) volume contraction at the interface of film due to a difference in the volume of the  $TiSi_2$  molecule and its precursor atoms; (2) stress relief in the substrate, as already discussed (Osada et al.);<sup>35</sup> and (3) the diffusing species during growth of the silicide. As explained previously, the diffusivity of boron and antimony are sensitive to the population of interstitials and vacancies, respectively. By examining their diffusion behavior in doping superlattices, which consist of delta profile doping spikes separated by undoped regions of silicon, depth profiles of the concentrations of vacancies and interstitials are obtained. The behavior of native point defects in silicon with a  $TiSi_2$  film formed in a variety of deposition and annealing conditions is examined in chapter three.

The second set of experimental results explores the effect of vacancy supersaturations in silicon on extrinsic dislocation loops. By observing antimony diffusion behavior in doping spikes on either side (depth wise) of a loop layer that is being saturated with vacancies from the surface, reactions between vacancies and loops are established to be diffusion limited and not reaction rate limited. By monitoring the enhanced dissolution of the loops in silicon with a  $\text{SiN}_x$  or  $\text{TiSi}_2$  film, estimates of the relative vacancy supersaturation are extracted in chapter four. These estimates show excellent agreement with estimates made by antimony diffusion. Conclusions and avenues of future work are discussed in chapter five.

## CHAPTER 2

### SAMPLE PREPARATION AND CHARACTERIZATION TECHNIQUES

#### 2.1 Doping superlattices

In this chapter, methods of sample preparation and characterization techniques common to the experiments in chapters three and four are discussed. This precludes repetition of the discussion in these chapters. Certain procedures not common to all the experiments are discussed in the relevant section. A lengthy discussion of the chemo-mechanical polishing procedure is undertaken in chapter three due its experimental nature and the fact that the results from that experiment explain disagreements between previous studies of native point defects by dopant diffusion in silicon with a silicide film.

##### 2.1.1 Growth and qualification of doping superlattices

There are several methods available to make dopant marker layers in silicon. A simple ion implant of the dopant and subsequent observation of its diffusion can provide information on native point defects. However, the implant itself creates a large disturbance in the native point defect concentration which must be annealed to return the crystal to equilibrium, if possible. Also, implant profiles are typically broad in width, asymmetric due

to channeling, and are not spatially separated from the surface, which makes slight perturbances in the profile difficult to detect. An epitaxial deposition of silicon can move the surface away from the implanted marker layer, but the broad profiles and the sensitivity limitations imposed by this broad profile remain. Another method is to grow marker layers by epitaxial chemical vapor deposition (CVD). This avoids the point defect perturbation created by implantation and can result in near box-shaped profiles of dopants.<sup>64</sup> However, CVD results in contamination from the precursor sources, particularly carbon, which has negative implications for measuring native point defect populations. Carbon has been shown to trap interstitials in silicon and therefore the presence of carbon in large and varying concentrations results in spurious data.<sup>65</sup> Sharp delta profiles cannot be achieved with CVD due to the inability to shut off source flow quickly. Chemical vapor deposition requires a relatively high temperature for deposition, causing diffusion of the grown-in dopant and there is a limited choice of precursor source materials.<sup>64</sup>

A method that avoids all of these problems is low temperature molecular beam epitaxy (LT-MBE). By utilizing a low growth temperature, extremely sharp delta doping profiles can be achieved. Use of elemental sources in co-evaporation limits impurities, and active carrier concentrations of  $7 \times 10^{21}$  for p type (B) and  $6 \times 10^{20}$  for n type (Sb) have been achieved, far greater than what has been achieved by other methods. Very sharp delta-doped profiles have been achieved by LT-MBE, as small as 3 nm, which is more a representation of SIMS resolution limitation than growth of the material.<sup>64</sup>

The silicon doping superlattice samples used in this study were grown by LT-MBE, by Dr. Hans -J. Gossmann of Bell Laboratories, Lucent

Technologies. All samples were grown in a custom-made MBE system with a base pressure of  $4 \times 10^{-11}$  Torr. Dopant atoms were co-evaporated from Knudsen cells while silicon atoms were evaporated using an electron beam. Float zone grown Si (100) substrates ( $\rho > 1000 \Omega \text{ cm}$ ) had a thermally grown oxide desorbed in situ by depositing 1.5 nm of Si at 800°C. A silicon buffer layer of 50 nm was first grown, followed by a doping spike 10 nm wide. Five subsequent doping spikes of the same width were grown with their centers spaced 100 nm apart, with undoped silicon grown in between. The shallowest doping spike was capped with 50 nm of silicon. Rapid thermal anneal (RTA) cycles were performed on the growing wafer for 120 sec every 30 nm during growth to prevent the growing film from turning amorphous. It has been shown that the wafers have uniform growth and doping concentration over the area of the wafer.<sup>66</sup>

The doping spikes can be doped to almost any level, from intrinsic to extrinsic. It has been shown that the intrinsic diffusivity that is extracted is not dependent on the concentration,<sup>67</sup> and so a variety of concentrations were used in this study, according to availability. Antimony doping superlattices were used only in extrinsic concentrations ( $1 \times 10^{19}/\text{cm}^3$  and higher), in order to increase the diffusion length of the dopant via concentration and electric field effects. Boron doping superlattices were used in both intrinsic ( $2 \times 10^{18}/\text{cm}^3$ ) and extrinsic ( $1 \times 10^{19}/\text{cm}^3$ ) concentrations. Boron's diffusivity is over an order of magnitude higher than antimony, and so doping superlattice concentrations as well as anneal times and temperatures were generally selected to insure adequate antimony diffusion that could be detectable by SIMS. Extrinsic and intrinsic diffusivities of the dopants are plotted in figure 2.1, using the data and methodology of Fair.<sup>58</sup>

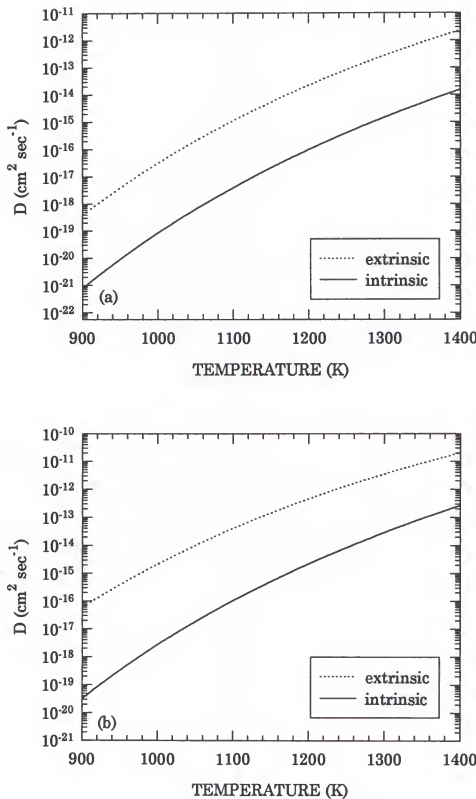


Figure 2.1. Diffusivity as a function of temperature and doping level of (a) antimony; and (b) boron. The extrinsic diffusivities assume a doping level of  $1 \times 10^{20}/\text{cm}^3$ .

As-grown doping superlattice wafers were diced into 3 x 6 mm<sup>2</sup> samples. Each as-grown wafer was tested to determine if it had an equilibrium concentration of vacancies and interstitials. Wafers were tested by annealing a sample at one short time (1 hour) and one at long time (10 hours) at 800°C in argon. If the diffusivity of antimony or boron were approximately constant with time and showed reasonable agreement with commonly accepted values taken from R.B. Fair,<sup>58</sup> the wafers were accepted as qualified for further experimentation.

#### 2.1.2 Secondary Ion Mass Spectrometry Depth Profiling and PROPHET Diffusivity Extraction

Sputtering secondary ion mass spectrometry (SIMS) was used to characterize the dopant profiles before and after processing. A 3 keV Cs<sup>+</sup> beam at an incident angle of 60° was used when tracing Sb, Ge, and O, while a 3 keV O<sub>2</sub><sup>+</sup> beam was used when tracing B. Sputtering rates were 0.3 - 1.0 nm/sec. Films were always removed by chemical etching prior to SIMS analysis. Samples that had a roughened surface from processing were polished to eliminate the possibility of surface-roughness-induced artifacts in depth profiling, as described in chapter three.

The extraction of the diffusion coefficients has been described previously by Gossmann et al., and will be summarized here.<sup>67,68</sup> The one dimensional diffusion equation is given by:

$$\frac{dc}{dt} = \frac{d}{dz} (D \frac{dc}{dz}) \quad (2.1)$$

where  $z$  is the depth into the sample,  $c$  is the dopant volume concentration, and  $D$  is the diffusivity. This equation can be solved via:

$$c(z, t) = \frac{1}{2\sqrt{\pi D t}} \int_{-\infty}^{+\infty} c(\zeta, 0) \exp\left(-\frac{(z-\zeta)^2}{4Dt}\right) d\zeta \quad (2.2)$$

where  $c(\zeta, 0)$  is the concentration at depth  $\zeta$  before diffusion and  $c(z, t)$  is the concentration after diffusion for a time  $t$  at a temperature  $T$ . Equation 2.2 is solved numerically by an iterative technique by using  $c(z, 0)$  (as-deposited SIMS depth profile of the dopant) and  $c(z, t)$  (post-processed diffused profile of the dopant). The technique varies  $D$  and  $z_0$  to get the best fit of the data. The diffusion coefficients are of the form

$$D^{\text{int}} = D_x h (1 + \beta \frac{m}{n_i}) \quad (2.3)$$

where  $m$  is the hole (in the case of boron doping) or electron (antimony doping) concentration, respectively,  $h$  is Fermi level dependent factor, and  $\beta = 3$  and  $\beta = 70 \exp\left(\frac{-0.43 \text{ eV}}{kT}\right)$  for boron and antimony, respectively. The fitting algorithm

returns  $D_x$  from which  $D^{\text{int}} = D_x (1 + \beta)$  is calculated.

The error bars on the resulting diffusivities  $D$  were generated by using a Monte Carlo approach to the two sources of error in SIMS depth profiles: statistical fluctuations in the determined concentrations and errors in the depth scale.<sup>67</sup> The error in the fluctuation of the concentration was determined by examining the fluctuation of the dopant signal in the nominally undoped sections of the wafers. The error in the depth scale was estimated to be 5%. A new  $C(z, t)$  set was generated by varying these

parameters. This was done 10 times and the mean of these values was taken as the diffusivity ( $D^{int}$ ) and the standard deviation ( $\pm\sigma$ ) as the error. The ratio of the diffusivities in the samples with films was normalized to the diffusivity of samples that were annealed without a film (control samples):  $\frac{D_{A,film}^{int}}{D_{A,control}^{int}}$ . By taking the ratio of the diffusivity of the dopant in a

sample with a film to that without a film, ratios  $\neq 1$  can be attributed to the presence of the film and quantifiable SIMS measurement error, yielding a relative error.

Systematic errors, such as that of the annealing temperature, which is estimated to be accurate to  $\pm 10^{\circ}\text{C}$ , and annealing time, which is not estimated but which includes a finite warm-up and cool-down time for the samples, and measuring dopant diffusion in silicon of varying purity, are mostly eliminated by annealing the samples (sample with a film and one without from the same wafer) concurrently and using doping superlattice samples from the same wafer. Nevertheless, these systematic errors must be considered when, for example, diffusivities of dopants from this study are compared to dopant diffusivities from other studies. For example, using the values from Fair<sup>58</sup> results in  $D_{\text{Sb}}^{int}$  ( $890^{\circ}\text{C}$ ) =  $3.26 \times 10^{-17} \text{ cm}^2/\text{sec}$  and  $D_{\text{Sb}}^{int}$  ( $900^{\circ}\text{C}$ ) =  $4.44 \times 10^{-17} \text{ cm}^2/\text{sec}$ , a  $\sim 26\%$  difference. A previous report has shown that measurements of interstitial diffusivity can vary over several orders of magnitude due to the presence of varying levels of carbon in wafers.<sup>69</sup> This would also affect the measurement of the relative interstitial concentrations. With this in mind, it is reasonable to state, for example, that  $\frac{D_{\text{B},film}^{int}}{D_{\text{B},control}^{int}} = 0.3$  indicates an interstitial depletion due to the presence of the

film in this study, while  $\frac{D_{B, \text{this study}}^{*, \text{int}}}{D_{B, \text{ref. 67}}^{*, \text{int}}} = 2$  shows reasonable agreement since

the diffusivity extractions were done by different groups using completely different processing and measuring techniques.

Since the primary measurement used in Chapter three is the ratio of the diffusivity of the dopants,  $\frac{D_{A, \text{film}}^{\text{int}}}{D_{A, \text{control}}^{\text{int}}}$ , the error for the ratio,  $\sigma_{\text{ratio}}$  was determined by:

$$\sigma_{\text{ratio}}^2 = f \left( \frac{D_{A, \text{film}}^{\text{int}}}{D_{A, \text{control}}^{\text{int}}} \right)^2 \quad (2.4)$$

$$\sigma_{\text{ratio}}^2 = \sum_{x=1}^{\infty} \left( \frac{\delta f}{\delta D_x} \right)^2 \sigma_x \quad (2.5)$$

The error on the ratio is then:

$$\sigma_{\text{ratio}} = \sqrt{\left( \frac{1}{D_{\text{control}}^2} \left( \sigma_{\text{film}}^2 + \left( \frac{D_{\text{film}}^2}{D_{\text{control}}^2} \right) \sigma_{\text{control}}^2 \right) \right)} \quad (2.6)$$

## 2.2 Transmission Electron Microscopy

Samples were examined using a JEOL 200CX operating at 200 keV. Diffraction conditions for each sample are described in each section.

Cross sectional TEM (XTEM) samples were made by dicing wafers into 0.25 mm wide strips on a Micro Automation Model 1006 high speed saw operating at 65,000 rpm. The strips were glued together with a polymer adhesive such that the surfaces of interest from each sample were in contact with each other, forming a doublet. The adhesive used was M-Line Accessories M bond 600, which was cured at 80°C for 3 hours. These strip assemblies were polished flat on both cross sectional sides using 400, 800, and 1200 grit sandpaper in succession down to a thickness of ~ 100  $\mu\text{m}$ . The assembly was dimpled on a VCR Group model D500i dimpler using 6  $\mu\text{m}$  and 1  $\mu\text{m}$  diamond paste (Buehler Inc., Metadi II) until the dimpled area was ~15  $\mu\text{m}$  thick. This specimen was then attached to a copper ring (Ted Pella Inc., 1 x 2 mm oval) with M bond 600. Samples were  $\text{Ar}^+$  ion milled in a Gatan model 600 dual ion mill operating at 1 mA current and 4 keV gun voltage. Samples were milled until a hole was obtained in the assembly in the strip area of the substrate surfaces.

Plan view TEM (PTEM) samples were prepared by cutting 2.7 mm discs out of the wafer with a Gatan model 601 ultrasonic disc cutter using SiC cutting grit. The discs were lapped to ~ 100  $\mu\text{m}$  thickness using 15  $\mu\text{m}$  and 5  $\mu\text{m}$   $\text{Al}_2\text{O}_3$  grit on a glass sheet. The discs were mounted on Teflon pedestals using Gulf Wax and the sample was completely smothered with Gulf Wax. A small hole was scribed in the Gulf Wax so that an area of the sample was exposed on one side. The disc was then drip etched with an acid solution (25% HF: 75%  $\text{HNO}_3$ ) until a small hole appeared in the sample.

### 2.3 Auger Electron Spectroscopy

Sputtering Auger Electron Spectroscopy (AES) was performed on a Perkin Elmer Phi 660 Scanning Auger Microprobe to determine the elemental composition of the annealed thin films. Sputtering was performed with an  $\text{Ar}^+$  beam at 3 keV, 100 nA, and  $30^\circ$  angle of incidence. The area sputtered depended on the sample. Thick films were sputtered at a faster rate by sputtering a smaller area, and vice versa for thinner films. Auger electrons were generated by a 30 nA, 5 keV electron beam at a  $30^\circ$  angle of incidence. The area rastered was approximately  $20 \times 20 \mu\text{m}^2$ . The particular elements traced varied with each sample and will be discussed in chapter three. Plots of the derivative of the number of electrons of a particular energy with respect to the energy,  $\frac{dN(E)}{dE}$ , were generated by surveying the film surface to choose Auger electrons of appropriate intensity.

### 2.4 Atomic Force Microscopy

Atomic Force Microscopy (AFM) samples were cleaned in an ultrasound bath of methanol for 5 minutes prior to mounting. Samples were analyzed on a Digital Instruments Nanoscope III. Tapping mode measurements were made using a silicon tip. The cantilever was tuned automatically using Digital Instruments software. The area scanned varied with each sample. Estimates of the root mean square roughness were taken from  $\Delta z$  measurements (amplitude variation).

### 2.5 Rutherford Backscattering Spectroscopy

Rutherford Backscattering Spectroscopy (RBS) was employed to determine the areal atomic densities of some the as-deposited metal or metal and silicon films. Analysis was performed using 2 MeV  ${}^4\text{He}^+$  ions at both near-incident ( $\sim 170^\circ$ ) and glancing ( $\sim 8^\circ$ ) angles. Near-incident angle analysis was only performed on single element film depositions (Ti only) to determine thickness, while both near-incident and glancing angles were used to analyze co-deposited metal and silicon films prior to annealing.

Composition analysis from the spectra was done using the RUMP<sup>TM</sup> computer program. Spectra obtained from the films were compared with spectra simulated using RUMP<sup>TM</sup>. Simulated spectra were calculated from known backscattering coefficients of the film elements and substrate using the conditions employed in obtaining real spectra (energy, ion species, angle of incidence, etc.). Thickness and composition of the film elements were varied in the simulated spectra until they matched the actual spectra.

### 2.6 Wafer Curvature

Wafer curvature of substrates with thin films were derived from high resolution x-ray diffraction measurements. X-ray rocking curves from the annealed samples were obtained from a Phillips HR-1 x-ray diffractometer with a Bonse-Hart collimator and a Bartles Monochromator. Samples were mounted in the x-ray system using beeswax to minimize any strain induced from mounting. After optimizing specimen tilt and rotation for maximum intensity, the samples were "rocked" through the (400) Bragg angle reflection. The change in peak position as a function of sample translation was then

used to evaluate wafer curvature. Derivation of the wafer curvature from this peak shift is described in greater detail in the Phillip's manual.<sup>70</sup>

## CHAPTER 3

## POINT DEFECTS IN SILICON WITH A TITANIUM DISILICIDE FILM

3.1 Introduction

The effect of the formation and anneal of a  $\text{TiSi}_2$  film on native point defects in silicon has been the subject of study for several years. Some experiments have shown that titanium silicidation results in enhanced antimony, boron, and arsenic diffusion, while others have claimed no enhanced diffusion of antimony or boron after titanium silicidation (Table 1.2). Since antimony diffuses by a pure vacancy mechanism, enhanced antimony diffusion would indicate a vacancy supersaturation.<sup>6</sup> On the other hand, enhanced boron diffusion would indicate an interstitial supersaturation.<sup>7</sup> Arsenic is thought to diffuse by a mechanism that is governed roughly equally by interstitial and vacancy diffusion and so little can be concluded from arsenic diffusion.<sup>3</sup> The extent of the estimates of the point defect perturbation, even when studies agree that a vacancy supersaturation occurs, vary over a large range.

The experiments in this chapter will establish the type of point defect perturbation that occurs in silicon annealed with a  $\text{TiSi}_2$  film by measuring antimony and boron diffusion in silicon delta doping-superlattices. While several authors have suggested potential mechanisms for how a thin film effects a change in native point defect equilibrium, none of these authors have

proved any of these mechanisms. Three of the proposed mechanisms are examined experimentally in the later sections of this chapter, with the aim of testing them. Also, the results presented in the first section of the chapter are reconciled with previous reports discussed in the second section, by showing that SIMS sputtering artifacts arising from an initially rough surface can lead to erroneous depth profiles of dopants. The morphology of the films is discussed as needed in the first section, and a complete discussion of the morphology of the co-deposited samples, which encompasses the entire range of as-deposited film compositions, is undertaken in the last section of the chapter. A lengthy discussion of morphology would only detract from a discussion of point defects, which is the main focus of this dissertation.

### 3.2 Antimony and Boron Diffusion in Silicon with Titanium as a Function of Temperature Annealed for One Hour

The goal of this experiment was to establish definitively the point defect perturbation, if any, in silicon annealed with a  $\text{TiSi}_2$  film by measuring antimony and boron diffusion in silicon doping superlattices. Samples were annealed at three temperatures to see if there was any variation in the magnitude of the effect with temperature. During the course of this experiment, a problem was encountered with sputtering through a rough surface while collecting SIMS information. This problem was rectified with a chemo-mechanical polishing procedure prior to SIMS. It was found that this phenomena could explain earlier results, and is therefore discussed in more detail in section 3.3.

### 3.2.1 Experimental procedure

Two sets of antimony and boron doping superlattices were used in this study: one which had titanium deposited on the surface with the doping spikes and another which did not. Each antimony spike had a concentration of  $1.0 \times 10^{20} /cm^3$  while each boron spike had a concentration of  $1.3 \times 10^{19} /cm^3$ . Transmission electron microscopy (TEM) and Atomic Force Microscopy (AFM) samples were made from Czochralski-grown p-type silicon (100). The TEM and AFM samples were used to study interface roughening due to silicidation and surface topography with polishing, respectively.

Prior to titanium deposition, all samples were cleaned in tri chloro ethane, acetone, methanol, de ionized water, 10:1 buffered oxide etch, and de ionized water in sequence. The samples were loaded into a sputtering chamber which was pumped down to a base pressure of  $2 \times 10^{-9}$  Torr. The chamber was backfilled with argon to a pressure of  $2 \times 10^{-3}$  Torr and 30 nm of titanium (99.995% purity) was sputtered onto the surface. Three sets of samples were annealed in forming gas (97% N<sub>2</sub> + 3% H<sub>2</sub>) for 1 hour at either 800°C, 840°C or 890°C. Forming gas was selected in an attempt to minimize oxygen intrusion into the films, but later studies would show the choice of annealing ambient to have little effect on film composition in this regard. The furnace anneals were selected to insure a reasonably large diffusion length for antimony, the only dopant that is known to diffuse by a vacancy-dominated mechanism.<sup>6</sup> Titanium disilicide C54 phase formation was confirmed by electron diffraction. Doping superlattice samples without a film were annealed concurrently at each temperature to provide a control for comparison. The silicide was removed by etching in dilute HF (25%) for 6 minutes. The samples were chemo-mechanically polished to smooth the

surface while removing minimal amounts of the underlying silicon, as shown by SIMS. The XTEM measurements were performed at 200 keV with the incident beam parallel to the [110] zone axis.

### 3.2.2 Results/Discussion

The  $\text{TiSi}_2$  films on the samples annealed at 840°C and 890°C islanded completely and all samples, including those annealed at 800°C, had significant interface roughening (Fig. 3.1). The XTEM micrograph shows a distinct bi-layer film formation. Electron diffraction (Fig. 3.2) and the AES sputtering profile (Fig. 3.3) revealed the film to be  $\sim$ 50 nm of  $\text{TiSi}_2$  and  $\sim$ 20 nm of  $\text{TiO}_{x\text{N}_{1-x}}$  on top of the  $\text{TiSi}_2$ . Overlap between the titanium (LMM) and nitrogen (KVV) lines prevented titanium and nitrogen data to be profiled concurrently, and titanium was chosen for profiling.<sup>72</sup> However, sputtering was halted several times to allow for a more accurate check by a three point method for the presence of nitrogen. Nitrogen's presence was found to coincide with that of oxygen. Due to the differing Auger sensitivity of the elements, changes in the Auger sensitivity of the elements with  $\text{TiO}_{x\text{N}_{1-x}}$ ,  $\text{TiSi}_2$ , and silicon, preferential sputtering, and the lack of standards, the peak counts of the Auger electrons of the differing elements could not be used to determine the compositions of the individual films. The  $\text{TiO}_{x\text{N}_{1-x}}$  film layer can, however, clearly be seen in the spectra, along with the  $\text{TiSi}_2$  layer. The development of a  $\text{TiO}_{x\text{N}_{1-x}}$  layer is common in processing and the bi-layer is therefore not unrepresentative of actual device processing. The formation of a thin  $\text{TiO}_{x\text{N}_{1-x}}$  is difficult to avoid due to titanium's strong affinity for both oxygen and nitrogen, even in the small concentrations that exist in the furnace gases.<sup>73</sup> Since the  $\text{TiO}_{x\text{N}_{1-x}}$  film is spatially removed from the  $\text{TiSi}_2/\text{Si}$



Figure 3.1. Cross sectional TEM micrograph of  $\text{TiSi}_2/\text{TiO}_x\text{N}_{1-x}$  films on silicon annealed  $840^\circ\text{C}/1$  hr/forming gas.

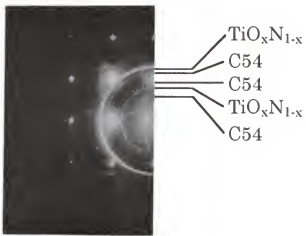


Figure 3.2. Electron diffraction pattern of  $\text{TiSi}_2/\text{TiO}_x\text{N}_{1-x}$  films on silicon annealed  $840^\circ\text{C}/1$  hr/forming gas.

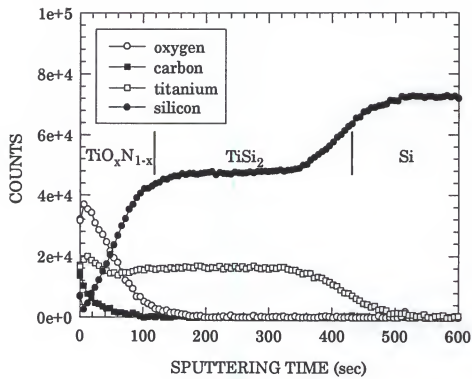


Figure 3.3. Auger spectra of the sample with  
30 nm Ti annealed 800°C/1 hr/forming gas.

interface and represents a small portion of the total film thickness, it is not significant in this study.

The interface roughness that is apparent in Figure 3.1 must be removed before accurate SIMS measurements can be made. About 110 nm of silicon was consumed by the silicide growth and subsequent etching and polishing, which was confirmed by SIMS measurements. To better quantify roughness, tapping mode AFM was performed on the wafer before any processing. A second 890°C annealed sample after the silicide had been etched but not polished was also analyzed, along with the same sample after polishing. The samples had a root mean square roughnesses of 0.12 nm, 22 nm, and 0.05 nm, respectively, showing that the polishing actually improves the surface quality of the as-received wafers. The doping superlattice samples annealed without a film were polished to the same degree to insure that any point defects introduced from polishing would be present in both sets of samples, and therefore any enhancement or retardation of diffusion in the silicided samples over the samples without a film is due only to the presence of the silicide. The chemo-mechanical polishing procedure is discussed in detail in section 3.3.

Figure 3.4 shows representative SIMS depth profiles from samples annealed at 840°C. The diffusion of antimony is enhanced while that of boron is retarded. Note that the first spikes were lost due to etching and polishing. The samples annealed at 800°C and 890°C showed similar behavior. The 800°C boron doping superlattice data is not available for a reason that will be made clear in section 3.3. The diffusivity of antimony and boron in silicided samples, normalized to the values in unsilicided samples, is shown in figure 3.5. The enhancement in  $D_{Sb}$  and retardation of  $D_B$  occurs through the deepest spike at 550 nm in both sets of samples. The relatively greater

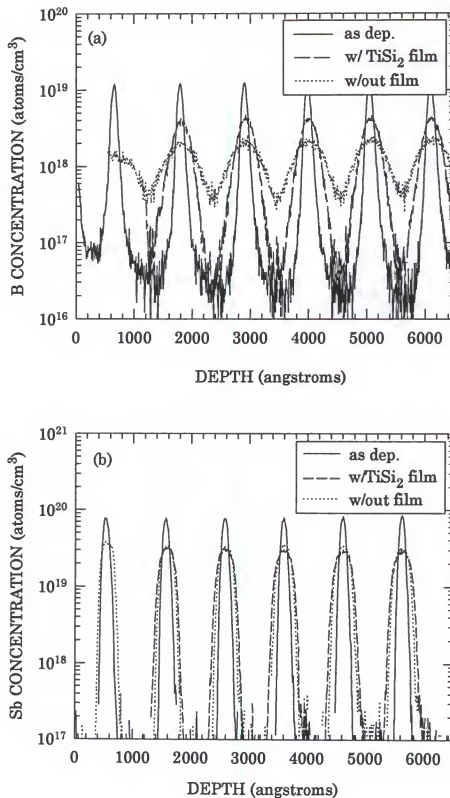


Figure 3.4. SIMS depth profiles of doping superlattices annealed 840°C/1 hr/forming gas:(a) boron; and (b) antimony.

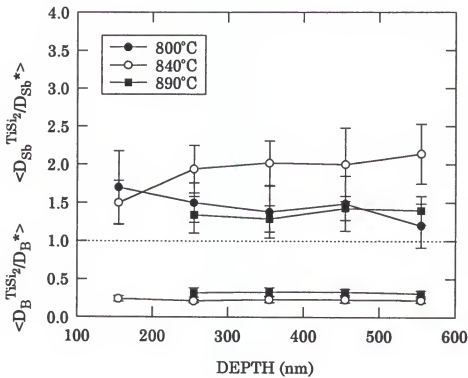


Figure 3.5. Depth profiles of normalized antimony and boron diffusivities in doping superlattices annealed for one hour at various temperatures.

variation in antimony diffusivity and larger error bars arise from the fact that antimony diffuses over an order of magnitude more slowly than boron (Fig. 2.1). Since  $D_{Sb}$  ( $D_B$ ) is proportional to the time averaged vacancy (interstitial) concentration, the results of figure 3.5 show that titanium silicidation and annealing lead to a vacancy supersaturation and interstitial undersaturation in the underlying silicon. The data demonstrates unambiguously that the presence of  $TiSi_2$  perturbs the point defect concentration in silicon.

A typical rapid thermal anneal (RTA) used to form the C54 phase of  $TiSi_2$  involves a low temperature anneal (e.g. 700°C/10 sec) to react the Ti with silicon to form the C49 phase, followed by a selective etch to remove the unreacted titanium, with a higher temperature anneal (e.g. 735°C/20 min) to convert the C49 phase to the low resistivity C54 phase.<sup>74</sup> However, this annealing sequence would result in equilibrium diffusion lengths too small to be detectable, making it impossible to measure the antimony diffusion coefficient in the control samples. Since little difference is seen in the diffusion behavior in these samples with a 90°C temperature difference, it is believed these results can be extrapolated to lower temperatures. Nevertheless, the possibility that the different morphology of  $TiSi_2$  films produced by RTA-type processing may change the point defect behavior cannot be ruled out.

*A priori*, it is difficult to discriminate between vacancy injection and vacancy supersaturation due to interstitial depletion via  $C_V C_I = C_V^* C_I^*$ . For example, a depletion of interstitials may result in an increase in the number of vacancies to maintain equilibrium. However, vacuum annealing experiments have shown that at 800°C, an interstitial undersaturation does not lead to a vacancy supersaturation even after 10 hours annealing time.<sup>18</sup> A depletion of interstitials due to a supersaturation of vacancies via I-V

recombination is unlikely since gold and platinum diffusion experiments indicate that recombination of vacancies and interstitials is inefficient at temperatures below 850°C.<sup>7,15</sup> The relatively small degree of vacancy supersaturation is incapable of increasing I-V recombination to any great extent. This indicates that the vacancy supersaturation is directly due to the presence of the TiSi<sub>2</sub> film.

If  $f_{SbV} = 1$ , the data indicates that  $\frac{C_V}{C_V^*} \sim 1.5, 1.9$ , and  $1.4$ , at 800, 840,

and 890°C, respectively. If  $f_{BI} = 1$ , the data indicates  $\frac{C_I}{C_I^*} \sim 0.23$  and  $0.32$  at

840 and 890°C, respectively. These estimates are averaged over the depth of the doping spikes. The effect of a TiSi<sub>2</sub> film on point defect equilibrium is much smaller than that in SiO<sub>2</sub> or SiN<sub>x</sub>.<sup>20,21</sup> However, the effect is still significant when considering dopant diffusion for shallow junctions in silicon devices. The effect is observed consistently over the temperature range studied and little change in this behavior is seen with temperature. Since the  $C_V^*$  value is changing drastically from 800 to 890°C (Fig. 1.3a), this indicates that the presence of the film "pins" the desired vacancy and interstitial concentrations at some value that is a multiple of equilibrium values. This will be discussed in greater detail in section 3.4 where a possible mechanism of point defect generation is evaluated.

### 3.2.3 Diffusivities of Antimony and Boron in Silicon Doping Superlattices vs. Literature Values

The preceding experiment compared antimony and boron diffusivities in silicon doping superlattices annealed with a film to those annealed without a film. This method allows the difference in diffusivities in the samples to be

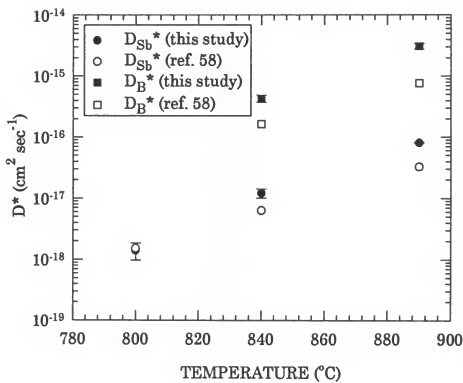


Figure 3.6. Comparison of intrinsic diffusivities from the doping superlattices and literature values.

attributed solely to the presence or absence of the film and not some inherent property of the doping superlattice. Nevertheless, it is *apropos* to compare the diffusivities of antimony and boron in the control samples without a film to literature values. Figure 3.6 compares the extracted intrinsic diffusivities (averaged over the depth) in the silicon doping superlattices annealed for one hour discussed in the previous section, with those predicted by Fair.<sup>58</sup> With the systematic errors that arise when comparing diffusivities between two studies discussed earlier, and the fact that the estimates were made almost twenty years apart, the values agree reasonably well. This indicates that the doping superlattices have "equilibrium" concentrations of point defects, and that diffusion in the superlattices reasonably approximates that of actual wafers. A simple  $\sqrt{4D^{\text{int}}t}$  calculation of the diffusion distance for antimony from the diffusivities yields 1.5 nm after 1 hour at 800°C, making it imperative that antimony in extrinsic concentrations be used in this study.

### 3.3 SIMS artifacts and Chemo-Mechanical Polishing Procedure

In this section, secondary ion mass spectrometry (SIMS) depth profile artifacts induced by surface roughness are detailed. The formation of a TiSi<sub>2</sub> film (30 nm of titanium deposited) at 800°C on a boron doping superlattice of silicon results in a rough (22.0 nm root mean square) interface between the film and silicon doping superlattice. This sample was originally part of the preceding experiment. However, the sample was mistakenly not chemo-mechanically polished prior to SIMS analysis. While this mistake reminded the author to be more careful, the results also explained prior literature results, proving that even mistaken serendipity can be the wellspring of ideas. After chemically etching off the TiSi<sub>2</sub> film, sputtering through a silicon

surface roughened by the silicide film while collecting SIMS information produces artifacts in the depth profiles of dopants. A simple chemo-mechanical polish (CMP) of the silicon smooths the surface while removing a minimal amount of silicon, as will be shown by AFM, SIMS, and TEM, resulting in accurate and consistent depth profiles.

### 3.3.1 SIMS Artifacts

Figure 3.7 shows the silicon surface after the  $\text{TiSi}_2$  has been etched off. The sample surface has a root mean square (rms) roughness of 22.0 nm. The rough surface comes from  $\text{TiSi}_2$  grains faceting to present low interfacial energy planes to silicon.<sup>41</sup> The resultant SIMS depth profiles of the boron DSL from this sample are shown in figure 3.8 as compared to the sample before the film was deposited and annealed. The annealed SIMS depth profiles are from several different areas on the same sample. Note that some silicon is consumed in the  $\text{TiSi}_2$  film and is subsequently lost when the  $\text{TiSi}_2$  is etched off. A more detailed profile of just the third doping spike is shown in figure 3.8. The three profiles are obviously inconsistent and the integrated counts of the dopants do not agree. If the underlying silicon surface is chemo-mechanically polished after the  $\text{TiSi}_2$  film has been etched but before SIMS profiling, the silicon surface is now smooth with a rms roughness of 0.1 nm (Fig. 3.9).

Using this procedure, a second sample was annealed and chemo-mechanically polished prior to SIMS analysis. This sample produced consistent and repeatable depth profiles of the dopant (fig. 3.4b). A comparison of this profile with that from the as-grown superlattice showed that only a minimal amount of silicon had been removed by the polishing

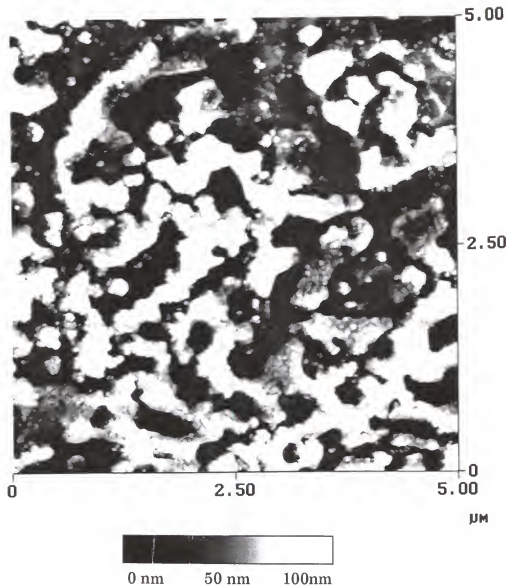


Figure 3.7. AFM micrograph of the underlying silicon surface after 30 nm Ti deposition, 800°C/1 hr/forming gas anneal, and removal of the film by chemical etching. The root mean square roughness is 22.0 nm.

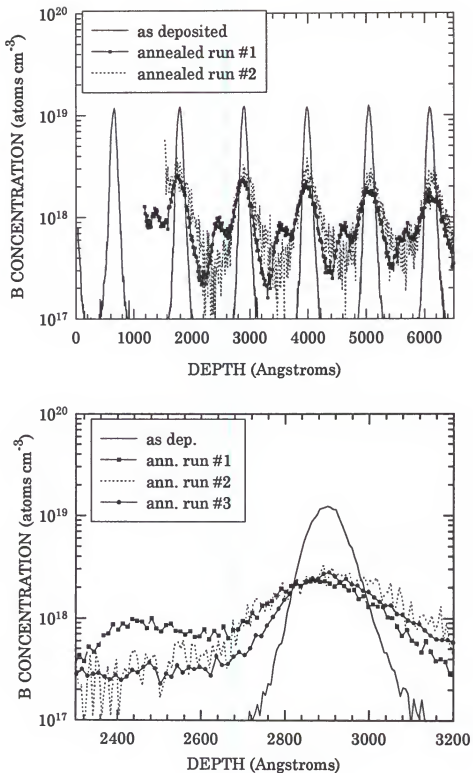


Figure 3.8. SIMS boron depth profile from the unpolished sample annealed 800°C/1 hr/forming gas: (a) complete (Si lost is from  $TiSi_2$  growth and etching); and (b) detail from figure 3.3a.

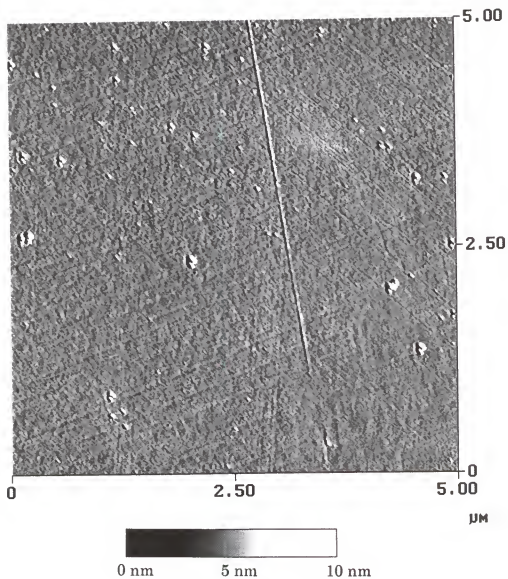


Figure 3.9. AFM micrograph of the underlying silicon surface after 30 nm Ti deposition, 800°C/1 hr/forming gas anneal, and removal of the film by chemical etching, and CMP. The root mean square roughness is 0.1 nm.

process. Note that the shallower slope on the backside of the doping spikes is not due to surface topography but is a consequence of ion-mixing effects.<sup>64,75</sup>

Ignoring the surface roughening, one could interpret the depth profiles in Figure 3.8 to show an enhancement of 10x in the diffusion of boron. A simple measure of the diffusion length at  $3 \times 10^{18}/\text{cm}^2$  in Figure 3.8 gives a  $\sqrt{4D^{\text{int}}t}$  value of 34 nm. This results in a boron diffusivity estimate of  $8.5 \times 10^{-16} \text{ cm}^2/\text{sec}$  for the unpolished sample vs.  $8.9 \times 10^{-17} \text{ cm}^2/\text{sec}$  that was measured in a sample annealed at 800°C for one hour without a TiSi<sub>2</sub> film. Hence, ignoring the surface roughening would lead one to conclude erroneously that there is an enhancement of boron diffusion in this case, whereas a retardation is actually observed (fig. 3.5). Since the apparent widening of the dopant spike due to the rough interface is temperature independent, ignoring the interface roughening would lead one to arbitrarily large enhancements by simply dropping the diffusion temperature. Since antimony has a small diffusion length in silicon, this effect is even worse for diffusion studies involving antimony.

Indeed, a recent series of papers has claimed anomalous asymmetric diffusion of antimony in doping spikes after the formation of a Pd<sub>2</sub>Si film at only 250°C for 100 minutes.<sup>76-78</sup> A comment by Ronsheim and Tejwani<sup>79</sup> on the original paper,<sup>76</sup> suggested that the depth profile may have been the result of artifacts from either the roughened surface or from sputtering-induced roughness. Honeycutt and Rozgonyi<sup>42</sup> saw similar "anomalous" diffusion behavior of antimony in silicon after formation of TiSi<sub>2</sub> film at 800°C for 5 minutes, which lead them to conclude  $\frac{\bar{D}_A}{D_A^*} = 10^7$ , where  $\bar{D}_A$  is the diffusivity of antimony in silicon with a TiSi<sub>2</sub> film and  $D_A^*$  is the diffusivity of antimony in silicon without a TiSi<sub>2</sub> film. However, this measurement was

later attributed to depth profile artifacts due to a rough interface and concluded to be erroneous.<sup>80</sup>

It is imperative that even minor amounts of interface roughness induced by the silicidation reaction be removed and the surface smoothed before SIMS depth profiling. This is true for any sputter depth profiling technique such as SIMS or Auger Spectroscopy, or for a technique such as Rutherford Backscattering, all of which rely on a uniform distance between the surface and the buried dopant that is being profiled. The results presented here, show clearly that sputtering artifacts, and not "anomalous" diffusion behavior, explain the results presented earlier.<sup>42,76-78</sup>

### 3.3.2 Chemo-Mechanical Polishing Procedure

Besides smoothing the surface, this CMP procedure can be used to remove silicon from a wafer. The procedure was developed on samples that had a buried dislocation loop layer formed in a Cz silicon (100) wafer (p type,  $5\text{-}10 \Omega \text{ cm}$ ) after an ion implant ( $1 \times 10^{15} \text{ Ge}^+ \text{ ions/cm}^2$  at 180 keV) and recrystallization anneal ( $800^\circ\text{C}$  for 1 hour in flowing  $\text{N}_2$ ). This loop layer is approximately 30 nm in width and is 240 nm deep (Fig 3.10a). The polishing agent was SYTON<sup>TM</sup> (South Bay Technology), a colloidal silica grit with an average particle size of 0.05  $\mu\text{m}$ , dispersed on a felt pad. The wafer was diced into 20 mm x 20 mm samples. Samples were attached to a South Bay Technology Model 150 lapping fixture using crystal bond. A force of 3.2 N was exerted on the samples, and the velocity was 0.2 m/s. Cross sectional TEM revealed how much silicon had been removed by the position of the loop layer relative to the surface (Fig. 3.10b). A plot of the removal rate is shown in Figure 3.11. The angle of the polished surface is estimated to be no greater

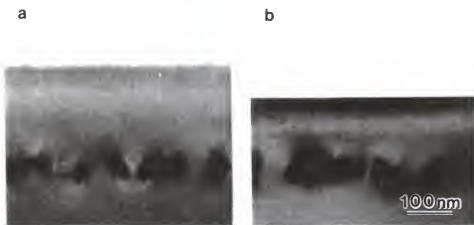


Figure 3.10. Cross sectional TEM micrographs of the dislocation loop layer. (a) prior to CMP; and (b) after CMP.

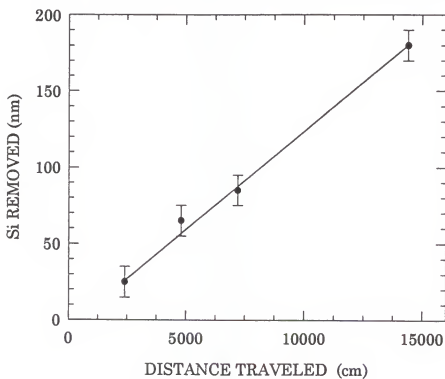


Figure 3.11. Silicon removal rate with CMP.

than 2 seconds from the initial surface. Atomic force microscopy plots on the polished surfaces are similar to Fig. 3.9, showing the surface to remain smooth even with large amounts of polishing.

### 3.4 Antimony and Boron Diffusion in Silicon with a 30 nm Titanium Film Annealed at 800°C as a Function of Time

After establishing the type and magnitude of the point defect perturbation, it is reasonable to question by what mechanism this perturbation is accomplished. Tan and Gösele<sup>33</sup> proposed that volume expansion at a growing silicon dioxide film interface is the mechanism for the interstitial supersaturation observed in the silicon substrate. The constituent elements were calculated to occupy less space than the  $\text{SiO}_2$  molecule, and this expansion was thought to be accommodated by the generation of Si interstitials. They noted however, that silicon nitride films result in a volume expansion as well, and yet result in a vacancy supersaturation. This argument is tested for vacancy supersaturations in silicon arising from the growth of  $\text{TiSi}_2$ . If volume contraction at the growing  $\text{TiSi}_2/\text{Si}$  interface causes a vacancy supersaturation, this supersaturation should occur as a "pulse" of vacancies injected during the earliest part of a high temperature anneal when the film is growing. The supersaturation of vacancies would be observed to decline with increased annealing time at the same temperature, as the "source" would be available only as long as the film was growing. This mechanism is therefore tested by annealing antimony doping superlattice samples with Ti films for various times at 800°C, and measuring how the antimony diffusivity varies with time.

### 3.4.1 Experimental

Antimony doping superlattices with a concentration  $6 \times 10^{19}/\text{cm}^3$  in each doping spike were used in this experiment. Boron doping superlattices were not used in order to conserve financial resources. Titanium (99.995% purity) was sputtered onto three samples to a thickness of 30 nm. The samples were annealed for 15, 60, and 600 minutes at 800°C in 99.95% purity argon. Doping superlattice samples without a film, one for each time, were annealed concurrently to provide a comparison (controls).

### 3.4.2 Results/Discussion

The films in this study show a range of morphology similar to the films with various thicknesses discussed above. The film annealed at 800°C for 600 minutes shows an island morphology (Fig. 3.12), while the films with shorter anneal times (15 and 60 minutes) are continuous, but with rough interfaces (Fig. 3.13). Antimony diffusion behavior is also similar to the previous study in that diffusion is enhanced in the samples annealed with titanium (figure 3.14 and 3.15). Figure 3.14 illustrates the difficulty in extracting antimony diffusivities in these annealing conditions without process simulation software such as PROPHET. The vacancy enhancement does show a slight decline with time (fig. 3.16). However, the decline is small, especially relative to the size of the error bars, and it will be shown that the magnitude of this decline is inconsistent with a "pulse," which should show a far greater difference in the relative vacancy supersaturation with the times studied. Interface roughening in the 600 minute annealed sample resulted in the first two doping spikes being lost due to etching and polishing.

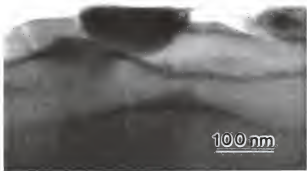


Figure 3.12. Cross sectional TEM micrograph of  $\text{TiSi}_2/\text{TiO}_x\text{N}_{1-x}$  films on silicon annealed  $800^\circ\text{C}/600$  min/argon.



Figure 3.13. Cross sectional TEM micrograph of  $\text{TiSi}_2/\text{TiO}_x\text{N}_{1-x}$  films on silicon annealed  $800^\circ\text{C}/15$  min/argon.

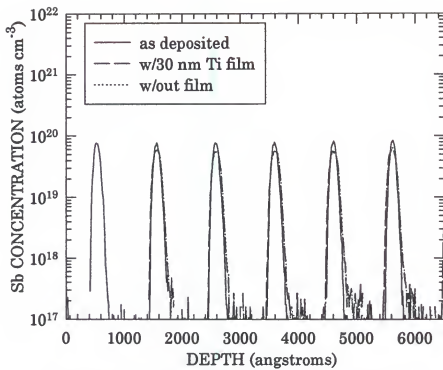


Fig. 3.14. SIMS depth profiles of antimony doping superlattices annealed 800°C/60 min/argon.

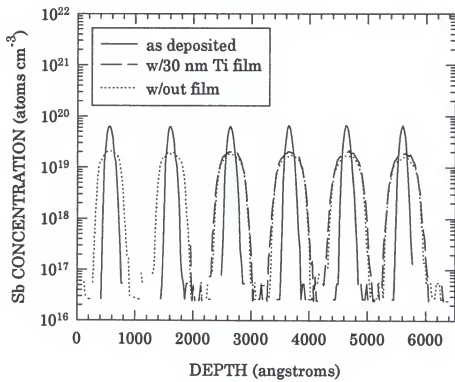


Figure 3.15. SIMS depth profiles of antimony doping superlattices annealed 800°C/600 min/argon.

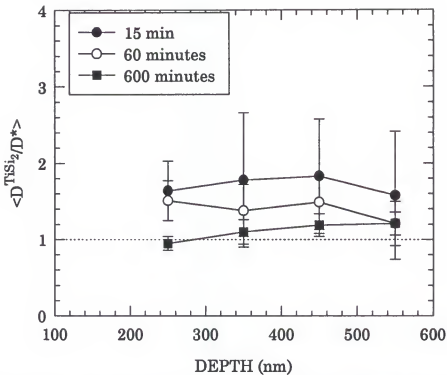


Figure 3.16. Depth profiles of normalized antimony diffusivities in doping superlattices with 30 nm of Ti annealed at 800°C for various times.

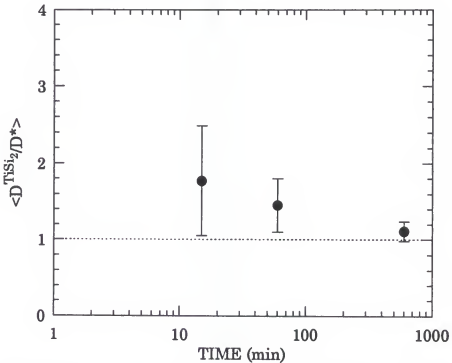


Figure 3.17. Average normalized antimony diffusivities in doping superlattices with 30 nm of Ti annealed at 800°C for various times.

A similar mechanism to that of Tan and Gösele<sup>33</sup> was proposed by Italyantsev and Kuznetsov<sup>81</sup> for vanadium disilicide (VSi<sub>2</sub>) films on silicon. A simple calculation of the relative volume contraction in TiSi<sub>2</sub> formation can be made by using density data to calculate the volume occupied by the silicide molecule and constituent atoms in the lattice.<sup>82</sup> The volume contraction is given by:

$$\Delta V = \frac{(V_{Ti} + 2V_{Si}) - V_{TiSi_2}}{(V_{Ti} + 2V_{Si})} \quad (3.1)$$

Using this equation, each molecule of TiSi<sub>2</sub> yields a 23% volume contraction. A large enhancement in D<sub>Sb</sub> in the 15 min samples should then be observed with a decay in this enhancement as point defect concentrations returned to equilibrium values with further annealing. This is not observed experimentally (Fig. 3.17). The vacancy profile of a large, finite, "pulse" of vacancies injected into the substrate during silicide growth can be modeled. If growth and vacancy injection occurs over a time period  $\tau_E$  during the anneal and  $\tau$  is the total diffusion time, the relative vacancy concentration is then:

$$\frac{C_V}{C_V^*} = \frac{1}{\tau} \int_0^\tau C_V dt = \frac{1}{\tau} \left[ \int_0^{\tau_E} E dt + \int_{\tau_E}^{\tau} dt \right] \quad (3.2)$$

where  $\tau = \tau_E + \tau_I$  and E is the "pulse" of vacancies injected. This solution is then independent of the vacancy diffusivity. By substituting the  $\frac{C_V}{C_V^*}$  values and the time for  $\tau$  in Fig. 3.17 into equation 3.2 and selecting  $\tau_E = 1$  min, representing a maximum time for film growth at 800°C, it is apparent that the observed vacancy population is inconsistent with a "pulse."

Alternatively, one could model a "pulse" as a Gaussian profile using:

$$C(x, t) = Q_0 \exp\left(\frac{-x^2}{4Dt}\right) \left(\prod Dt\right)^{-1/2} \quad (3.3)$$

where  $Q_0$  is the vacancy concentration that is initially injected,  $C(x, t)$  is the concentration at a depth  $x$  in the substrate at a time  $t$ , and  $D$  is the diffusivity of the vacancies. The value  $D(800^\circ\text{C}) = 8 \times 10^{-14} \text{ cm}^2/\text{sec}$  is used, which was measured by antimony diffusion in doping superlattices.<sup>83</sup> The observed diffusivities should vary considerably from the first spike to the last, well above the measurement error (fig. 3.18). This is not observed. Even with the drastic change in the coverage and shape of the film from islanded to continuous (Figs. 3.12 and 3.13) in the 15 to 600 minute anneals, the change point defect populations caused by the presence of  $\text{TiSi}_2$  is essentially the same in both sets of samples. These results show that the point defect flux is not a function of the growth of the silicide. The larger  $\frac{C_V}{C_V^*}$  at 15 minutes may

reflect both inaccurate depth profile data, the slow response of the point defects to higher thermal equilibrium values at  $800^\circ\text{C}$  from room temperature,<sup>16</sup> or other phenomena.

This data is in agreement with the results in section 3.2 where little temperature dependence is seen in the enhancement of antimony diffusion or retardation of boron diffusion. The estimate from Tan and Gösele<sup>7</sup> is that  $C_V^*$  is  $8.6 \times 10^{13}$  and  $4.3 \times 10^{13} \text{ vac/cm}^3$  at  $800$  and  $890^\circ\text{C}$ , respectively. If the vacancies are injected as a finite pulse that is dependent on the growth of the film,  $\frac{C_V}{C_V^*}$  should be much larger at  $800$  than  $890^\circ\text{C}$  due to the smaller value

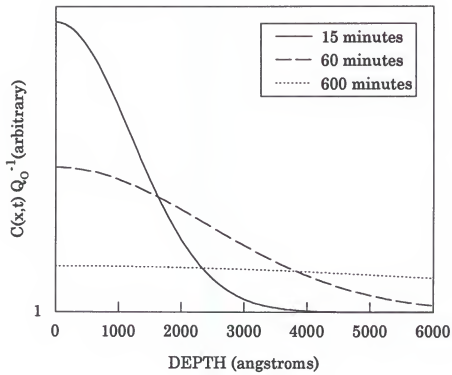


Figure 3.18. Gaussian depth profile of vacancies assuming a finite "pulse" of vacancies injected at  $t = 0$ .

of  $C_V^*$ . The results in section 3.2 show no significant change in  $\frac{C_V}{C_V^*}$  in silicon

with a  $TiSi_2$  film annealed at 800 and 890°C for one hour. This reinforces the results from this experiment showing that the vacancies are not injected as a pulse.

### 3.5 Antimony and Boron Diffusion Behavior in Silicon with Different Thicknesses of Titanium Deposited and Annealed for 1 hour at 850°C

Osada et al.<sup>35</sup> have recently proposed that  $Si_3N_4$  films effect a vacancy supersaturation in silicon by a stress compensation mechanism. They found that by depositing thicker  $Si_3N_4$  films, a greater vacancy supersaturation occurred in the underlying silicon after annealing at 1100°C. It was theorized that thicker films imposed a greater stress in the substrate via the coefficient of thermal mismatch (cte) between the film and substrate. The tensile stress in the film induces a compressive stress in the substrate, which is then relieved by Frenkel pair generation at the interface, with interstitials diffusing into the film or annihilating at the interface, and vacancies diffusing into the substrate. A supersaturation of vacancies in the substrate acts to increase the lattice constant of silicon, compensating the decrease due to the compressive stress imposed by the cte mismatch. They showed the relative vacancy supersaturation to correlate with the amount of stress, and, therefore, with film thickness.

In this section, the same reasoning is applied to titanium disilicide thin films. Like silicon nitride, titanium disilicide is under a tensile stress and results in a vacancy supersaturation in the silicon substrate. The stress compensation mechanism is investigated by varying the thickness of the

titanium films deposited on antimony doping superlattices and annealing at 850°C/1 hour/argon.

### 3.5.1 Experimental

The antimony spikes had a concentration of  $6 \times 10^{19}/\text{cm}^3$  or  $1 \times 10^{20}/\text{cm}^3$ . Prior to film deposition, all samples were cleaned by a dilute (1:20) HF dip. The samples were loaded into an ultra high vacuum MBE chamber that was pumped down to a base pressure of  $1 \times 10^{-10}$  Torr. Three doping superlattice samples (Sb concentration  $1 \times 10^{20}/\text{cm}^3$ ) had titanium (99.995% purity) evaporated by electron beam to area densities of  $1.3 \times 10^{17}$ ,  $2.3 \times 10^{17}$ , and  $3.4 \times 10^{17}$  Ti atoms/ $\text{cm}^2$ , as shown by Rutherford backscattering spectrometry (Fig. 3.19). Using the density of titanium,  $5.7 \times 10^{22}$  atoms/ $\text{cm}^3$ , this equates to as-deposited thicknesses of 22, 40, and 59 nm, respectively.<sup>82</sup> As the reaction of titanium and silicon would consume the doping spikes in the growing TiSi<sub>2</sub> for very thick films, titanium and silicon were co-evaporated to a thickness of  $\sim 680$  nm and an approximate composition of TiSi<sub>1.8</sub> (as deposited) on a fourth sample, again determined by ion scattering. Rutherford backscattering spectra showed the area densities of  $1.4 \times 10^{18}$  Ti atoms/ $\text{cm}^2$  and  $2.5 \times 10^{18}$  Si atoms/ $\text{cm}^2$  (Fig. 3.20). Assuming the rule of mixtures holds for TiSi<sub>x</sub> alloys, and the as-deposited film had the titanium crystal structure, an approximate composition of TiSi<sub>1.8</sub> is derived for the co-deposited film. It will be shown in section 3.6 that co-deposition of silicon with titanium prior to silicidation does not effect the point defect perturbation. A thin film approximately 8 nm in thickness was co-deposited on a fifth sample. Rutherford backscattering again showed area densities of  $1.6 \times 10^{16}$  Ti atoms/ $\text{cm}^2$  and  $2.9 \times 10^{16}$  Si atoms/ $\text{cm}^2$ , resulting in a composition of

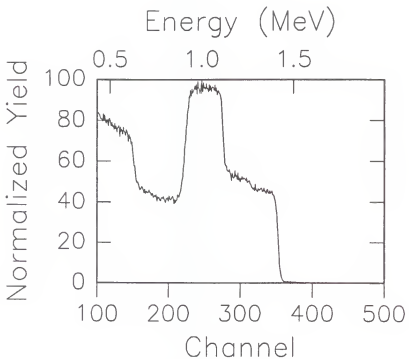


Figure 3.19. RBS spectra (glancing angle) for the co-deposited  $\text{TiSi}_{1.8}$  film with nominal 312 nm Ti thickness before annealing.

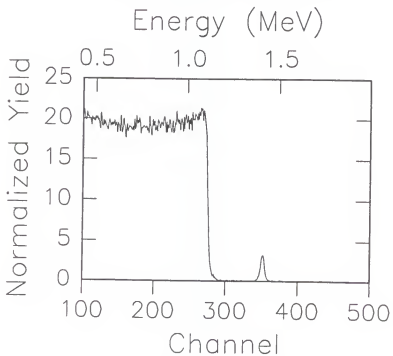


Figure 3.20 RBS spectra (glancing angle) for the co-deposited  $\text{TiSi}_{1.8}$  film with nominal 4 nm Ti thickness before annealing.

TiSi<sub>1.8</sub> for this sample. A rule of mixtures approximation yields titanium thicknesses of 312 and 4 nm for the two co-deposited samples, respectively. The samples for the stress compensation study were annealed for 60 minutes at 850°C in Ar (99.95% purity). Upon annealing, the samples formed TiSi<sub>2</sub> with approximate thicknesses of 10 and 780 nm. The doping superlattice samples for the co-deposited films had an antimony concentration of 6 x 10<sup>19</sup>/cm<sup>3</sup>.

### 3.5.2 Results/Discussion

Due to the varying thickness, the TiSi<sub>2</sub> films impose a range of stresses in the substrate during annealing. Growth of the film and continued post growth annealing results in wafer curvature with the film in tension.<sup>84</sup> The thermal stress in the substrate can be estimated by:<sup>85</sup>

$$\sigma_s \equiv 6E_s \langle \epsilon_c \rangle \Delta \left( \zeta - \frac{1}{3} \right) \quad (3.4)$$

where  $\sigma_s$  is the substrate stress,  $E_s$  is the Young's modulus of the substrate,  $\epsilon_c$  is the differential between the coefficients of thermal expansion of the substrate and film,  $\Delta$  is the layer-to-substrate thickness ratio, and  $\zeta = \frac{r_s}{t_s}$ ,

where  $r_s$  is the distance from the backside of the substrate and  $t_s$  is the thickness of the substrate. This assumes that the stress is linearly dependent on the temperature, which has been shown by Svilan et al.<sup>84</sup> Estimated stresses in the substrate at a arbitrary depth 100 nm below the interface are listed in Table 3.1 from equation (3.4).

Table 3.1. Film properties with thickness variation.

Ti thickness as deposited (nm)	deposition method	morphology (after anneal)	$\sigma_{\text{sub}}$ during anneal (@ 100 nm in dyne/cm <sup>2</sup> )
4*	co-dep.	islanded	620**
22	Ti only	islanded	4240**
40	Ti only	continuous	7700
59	Ti only	continuous	10240
312*	co-dep.	continuous	60070

\* indicates projected titanium thickness based on the rule of mixtures assumption of elemental titanium and silicon densities

\*\* based on continuous film coverage

The substrate stress varies linearly with film thickness. Therefore, the thickest film should impose on the substrate  $\sim 100$ x the stress of the thinnest film. As shown in figure 3.21, the thinner films ( $t_{\text{Ti}} < 22$  nm) have completely islanded. This should lead to a lower overall stress compared to those films ( $t_{\text{Ti}} > 22$  nm) that have continuous film coverage (fig. 3.22). Nevertheless, a stressed region of the substrate in the neighborhood of each island is not ruled out. Table 3.1 shows that the two thinnest films are discontinuous.

Representative examples of antimony depth profiles are shown in figure 3.23. The diffusivity of antimony is enhanced and the diffusivity of boron is retarded in the sample with a  $\text{TiSi}_2$  film compared to the control sample, consistent with a vacancy supersaturation and interstitial undersaturation, respectively, shown in the earlier studies. Figure 3.24 shows the diffusivities of antimony in the samples with a  $\text{TiSi}_2$  film normalized to



Figure 3.21. Cross sectional TEM micrograph of the annealed  $\text{TiSi}_{1.8}$  film on silicon with nominal 4 nm Ti thickness.



Figure 3.22. Cross sectional TEM micrograph of the annealed  $\text{TiSi}_{1.8}$  film on silicon with nominal 312 nm Ti thickness.

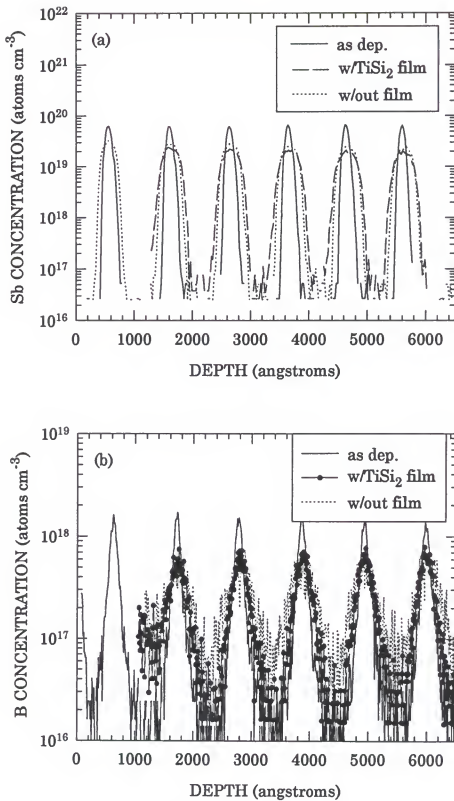


Figure 3.23. SIMS depth profiles of doping superlattices annealed 850°C/1 hr/argon with 4 nm Ti  
(a) antimony; and (b) boron.

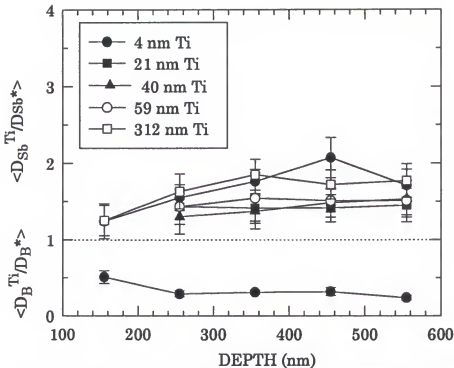


Figure 3.24. Depth profiles of normalized antimony diffusivities in doping superlattices annealed 850°C/1 hr/argon with various thicknesses of Ti.

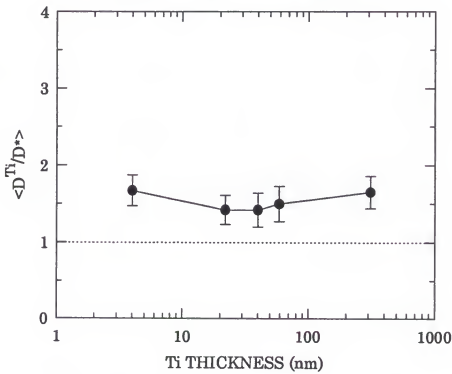


Figure 3.25. Average normalized antimony diffusivities in doping superlattices annealed 850°C/1 hr/argon with various thicknesses of Ti.

the diffusivities of dopants in the control samples that were annealed without a film. When the antimony diffusivities of the samples with various titanium thicknesses are normalized to antimony diffusivities in the samples without a film, little variation is observed (fig. 3.25). Clearly, a vacancy supersaturation that varies with the stress level in the substrate is not occurring in the samples with a  $\text{TiSi}_2$  film.

A similar effect as Osada et al.<sup>35</sup> reported, namely a large dependence of dopant diffusivity with the thickness of a deposited film, was not observed despite a similar range of film thicknesses and a more sensitive dopant marker technique in this study. The mechanism of stress relief of the substrate in the near interface region in silicon with  $\text{TiSi}_2$  films is ruled out. Two differences in experimental procedures used here vs. Osada et al. that could account for the differences between the two studies are noted: namely, their use of ion implanted boron as the marker dopant and the higher annealing temperatures ( $> 1000^\circ\text{C}$ ). Ion implantation is known to cause a larger point defect perturbation in and of itself and may effect the interstitial-vacancy (I-V) recombination process.<sup>19</sup>

In this section it has been established that point defect generation to varying stress in the substrate in silicon with a  $\text{TiSi}_2$  film. The drastic difference in morphology of the thinnest films ( $\sim 10$  nm) vs. thickest ( $\sim 780$  nm) implies that the observed vacancy supersaturation is more related to an intrinsic property of the  $\text{TiSi}_2/\text{Si}$  interface than film growth and morphology.

### 3.6 Antimony and Boron Diffusion in Silicon Annealed at 850°C for 1 hour with Co-deposited Ti + Si or Co + Si

A third mechanism that is studied is the effect of the diffusing species during film growth. All the precursor phases of  $TiSi_2$  as well as  $TiSi_2$  form by silicon diffusing into titanium.<sup>85</sup> Wen et al.<sup>47</sup> have suggested that these silicon atoms leave behind vacancies in the substrate, causing a vacancy supersaturation. The formation of  $CoSi_2$  from  $CoSi$  proceeds via diffusion of metal into the silicon substrate.<sup>87</sup> This process should therefore inject interstitials. This theory is explored by annealing  $TiSi_x$  and  $CoSi$  films with silicon contents ranging from silicon deficient ( $x = 0$ ) to silicon rich ( $x > 2.0$ ) on doping superlattices. In each case, the change in the native point defect concentration was measured after film formation and annealing. It was established in sections 3.3 and 3.4 that film growth is an unlikely source of point defect generation, since the point defect perturbation does not correlate with film thickness and does not show a strong time dependence. The experiment detailed in this section will directly determine if the diffusing species plays a role in point defect generation.

#### 3.6.1 Experimental

Each antimony spike had a concentration of  $1 \times 10^{20} /cm^3$  while each boron spike had a concentration of  $2 \times 10^{18}/cm^3$ . Prior to metal deposition, all samples were cleaned by a dilute HF (1:20) dip. The samples were loaded into an ultra high vacuum (UHV) MBE chamber that was pumped down to a base pressure of  $1 \times 10^{-10}$  Torr. Titanium or cobalt of 99.995% purity and silicon were co-evaporated in separate depositions. The mass deposition

conditions and flux were tailored to deposit the same total number of titanium atoms per unit area on each sample. Rutherford backscattering spectrometry gave compositions of Ti, TiSi<sub>0.8</sub>, TiSi<sub>2.2</sub>, and CoSi<sub>0.8</sub> respectively, and densities of  $1.1 \times 10^{17}$  Ti atoms/cm<sup>2</sup> (Ti only sample),  $1.2 \times 10^{17}$  Ti atoms/cm<sup>2</sup> and  $9.8 \times 10^{16}$  Si atoms/cm<sup>2</sup> (TiSi<sub>0.8</sub>),  $1.3 \times 10^{17}$  Ti atoms/cm<sup>2</sup> and  $2.8 \times 10^{17}$  Si atoms/cm<sup>2</sup> (TiSi<sub>2.2</sub>), and  $2.4 \times 10^{17}$  Co atoms/cm<sup>2</sup> and  $1.9 \times 10^{17}$  Si atoms/cm<sup>2</sup> (CoSi<sub>0.8</sub>). Anneals were performed for 1 hour at 850°C in 99.95% purity argon cooled by a mixture of dry ice and acetone prior to furnace entry to prevent water intrusion. The following section will describe the composition, morphology, and interface roughness of the films in more detail.

### 3.6.2 Results/Discussion

Figures 3.26a and b show representative SIMS depth profiles. The diffusivity of antimony is again enhanced in samples with a TiSi<sub>2</sub> film compared to a sample annealed at the same time without titanium while that of boron is again retarded. Figure 3.27 shows the antimony and boron intrinsic diffusivities in all the silicided samples, normalized to the diffusivities in the corresponding samples without a film. The presence of TiSi<sub>2</sub> and CoSi<sub>2</sub> films from co-deposited metal and silicon leads to a slight interstitial undersaturation and slight vacancy supersaturation in the silicon substrate. This result is independent of the silicon content of the as-deposited alloys.

Since the precursor phases of TiSi<sub>2</sub> as well as TiSi<sub>2</sub> itself form by silicon diffusion, TiSi<sub>2</sub> formed from co-deposited TiSi<sub>x</sub> with x = 0 and x = 0.8 should form completely by silicon diffusion, leaving vacancies in the silicon

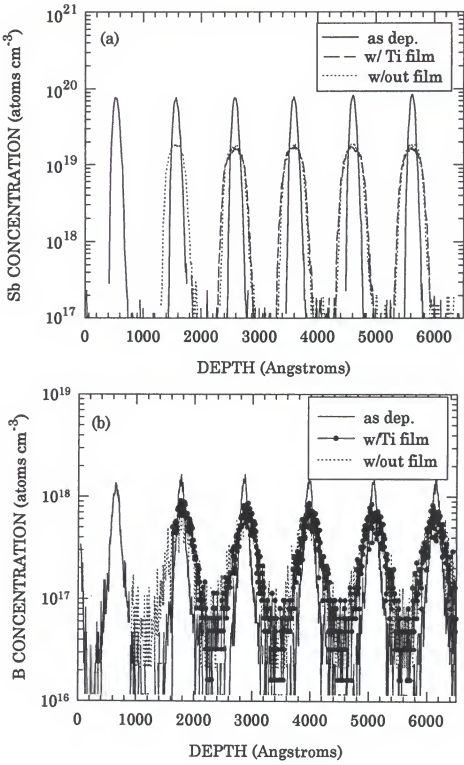


Figure 3.26. SIMS depth profiles of doping superlattices annealed 850°C/1 hr/argon with 22 nm Ti: (a) antimony; and (b) boron.

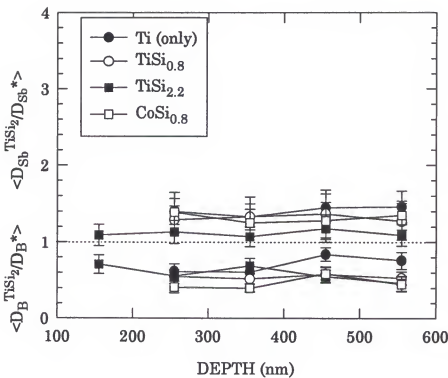


Figure 3.27. Depth profiles of normalized antimony and boron diffusivities in doping superlattices annealed 850°C/1 hr/argon.

substrate, as actually observed. However, for  $x = 2.2$ , no silicon from the substrate is consumed by the reaction, hence the point defect concentrations in the substrate should remain unchanged, contrary to the experimental observation. The two precursor phases of  $\text{CoSi}_2$ , namely  $\text{Co}_2\text{Si}$  and  $\text{CoSi}$ , form by cobalt and silicon diffusion, respectively, while  $\text{CoSi}_2$  forms by cobalt diffusion.<sup>87</sup> Thus the formation of  $\text{CoSi}_2$  starting from  $\text{CoSi}_{0.8}$  should be dominated by cobalt diffusion with a smaller amount of silicon diffusion. Given that recombination of interstitials and vacancies is slow at the annealing temperature, one would consequently expect both an interstitial and vacancy excess. However, the experiment results in an interstitial deficit. The facts that (1) the magnitude of the point defect perturbation is approximately the same for all samples; (2) growth is complete in both films in less than a minute at 850°C while the measurements were taken after a one hour anneal;<sup>38,88</sup> and (3)  $\text{TiSi}_2$  and  $\text{CoSi}_2$  have different formation kinetics and yet have the same point defect results in our samples,<sup>54,72,86,88</sup> argue strongly against the theory that the diffusing species and film growth itself are the primary mechanisms for the observed point defect perturbation.

This experiment reinforces the results of section 3.4 in showing that the reaction between titanium and silicon is not a primary mechanism for point defect generation. Another experiment by Fahey and Dutton<sup>89</sup> also indicates that the diffusing species has little to do with point defect generation. In Fahey and Dutton's experiment, silicon substrates with phosphorous or boron dopant marker layers had a  $\text{WSi}_2$  film deposited on them. These were then annealed for 30 or 60 minutes at 1100°C in oxygen, resulting the formation of an  $\text{SiO}_2$  film on top of the  $\text{WSi}_2$ . Silicon diffused from the substrate through the  $\text{WSi}_2$  film to react with the oxygen to form the oxide layer. Phosphorus and boron did not show retarded diffusion, indicating that no vacancy

supersaturation occurred, reinforcing the notion that an efflux of silicon atoms does not necessarily result in a vacancy efflux in the opposite direction.

### 3.7 Morphology of the Films from Co-deposition

In this section the microstructure of the films from the preceding section are described in more detail. The films produced several interesting characteristics, including suppression of  $TiO_xN_{1-x}$  formation despite annealing in argon ambient, and a variation in both grain size and interface roughening with co-deposition composition. These characteristics warranted a more detailed characterization as compared to the other films.

#### 3.7.1 Experimental

All samples were prepared from the same 2" (100) float zone grown Si wafer ( $\rho > 1000 \Omega \text{ cm}$ ). The wafer was diced into 3 samples  $15 \times 20 \text{ mm}^2$  and prepared according to the procedures in the preceding section. The deposition and characterization procedures of the as-deposited films has been described in section 3.6.

#### 3.7.2 Results

Films were deposited with the nominal compositions Ti, TiSi, and  $TiSi_{2.5}$ , in three separate samples, respectively. Ion scattering on the Ti (only) sample showed an areal density of  $1.1 \times 10^{17} \text{ Ti atoms/cm}^2$ . Using an atomic density value of  $5.71 \times 10^{22} \text{ Ti atoms/cm}^3$ , this results in an as-deposited film thickness of 22 nm. A direct measurement of the film

thickness via cross sectional TEM of 30 nm (Fig. 3.28) on the as-deposited Ti (only) sample indicates the as-deposited films have significant porosity. This shows that using just TEM micrographs for as-deposited thickness data is a poor indicator of final  $\text{TiSi}_2$  thicknesses. In general, predicting final  $\text{TiSi}_2$  thicknesses from as-deposited Ti or Ti + Si thicknesses and compositions was found to be difficult even when accounting for porosity using ion scattering,<sup>82</sup> as will be shown.

Accurate measures of the volume densities of the as-deposited alloys are not available. Ion scattering cannot, therefore, be used to derive the deposited film thicknesses of the alloys without an assumption of the crystal structure of the as-deposited alloy. Unfortunately, electron diffraction patterns of the as-deposited alloys were inconclusive. For the co-deposited samples, we measure area densities of  $1.2 \times 10^{17}$  Ti atoms/cm<sup>2</sup> and  $9.8 \times 10^{16}$  Si atoms/cm<sup>2</sup> (giving an as-deposited composition of  $\text{TiSi}_{0.8}$ ), and  $1.3 \times 10^{17}$  Ti atoms/cm<sup>2</sup> and  $2.7 \times 10^{17}$  Si atoms/cm<sup>2</sup> ( $\text{TiSi}_{2.2}$ ) were measured by ion scattering. The as-deposited thicknesses were 70 nm ( $\text{TiSi}_{0.8}$ ) and 90 nm ( $\text{TiSi}_{2.2}$ ), respectively, as measured by XTEM micrographs. If one takes the volume atomic density of silicon,  $5 \times 10^{22}$  atoms/cm<sup>3</sup>, and titanium,  $5.7 \times 10^{22}$  atoms/cm<sup>3</sup>, the measured area densities, and use the rule of mixtures for the compositions, we derive calculated thicknesses of 41 nm ( $\text{TiSi}_{0.8}$ ) and 78 nm ( $\text{TiSi}_{2.2}$ ) are derived. For the sample with co-deposited cobalt and silicon, an area density of  $2.4 \times 10^{17}$  Co atoms/cm<sup>2</sup> and  $1.9 \times 10^{17}$  Si atoms/cm<sup>2</sup> ( $\text{CoSi}_{0.8}$ ) was measured. Using the atomic density of cobalt,  $9.1 \times 10^{22}$  atoms/cm<sup>3</sup>, and its cubic crystal structure, a thickness of 47 nm is derived for the co-deposited  $\text{CoSi}_{0.8}$  film by ion scattering, while a XTEM measurement indicated 55 nm thickness.

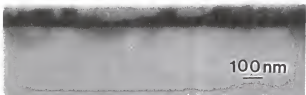


Figure 3.28. Cross sectional TEM micrograph of the as-deposited Ti (only) film on silicon.

The as-deposited films show a columnar structure typical of deposited metal films (Fig. 3.28).<sup>90</sup> This same structure was representative of all four samples. Jeon et al.<sup>38</sup> have speculated that interface roughening between the TiSi<sub>2</sub> and silicon originates from silicon selectively diffusing into this grain structure. However, as will be discussed, the size of the roughness (peak-to-valley) is much larger than the diameter of these columnar grains, indicating that this is not the origin of the roughening.

Figure 3.29 shows the Auger spectra from the annealed TiSi<sub>0.8</sub> sample, also representative of the spectra from the annealed Ti (only) sample. Overlap between the titanium (LMM) and nitrogen (KVV) lines prevented titanium and nitrogen data to be profiled concurrently, so that titanium was chosen for analysis, as previously described.<sup>72</sup> The TiO<sub>x</sub>N<sub>1-x</sub> film layer can clearly be seen in the spectra, along with the TiSi<sub>2</sub> layer. The rough TiSi<sub>2</sub>/Si interface is evident in the slow decay of the titanium signal and slow increase in the silicon signal at about 1000 seconds into the sputtering in Figure 3.29. Similar observations were made on the annealed Ti (only) sample.

The Auger spectra from the annealed TiSi<sub>2.2</sub> sample is shown in figure 3.30. It confirms that little if any TiO<sub>x</sub>N<sub>1-x</sub> formed on top of the TiSi<sub>2</sub>. It also indicates that at least some of the "excess" deposited silicon lies on top of the TiSi<sub>2</sub> film. A quantification of how much of the "excess" silicon exists on top of the TiSi<sub>2</sub> film is not possible. The relatively steeper decay in the titanium signal and steeper increase in the silicon signal indicate the interface was not as rough as in the other two samples, confirmed by AFM.

The Auger spectra from the annealed CoSi<sub>0.8</sub> (as-deposited) sample is shown in figure 3.31. The spectra, along with the cross sectional TEM micrograph (Fig. 3.32), indicates no other species is present in significant

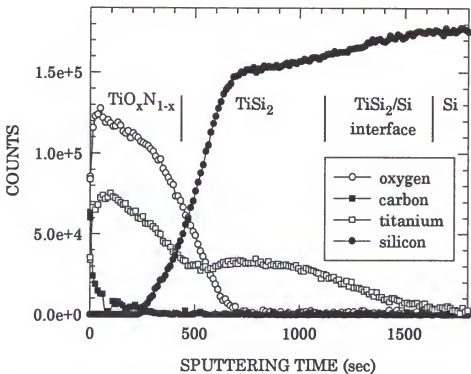


Figure 3.29. Auger electron spectra of the annealed  $\text{TiSi}_{0.8}$  film.

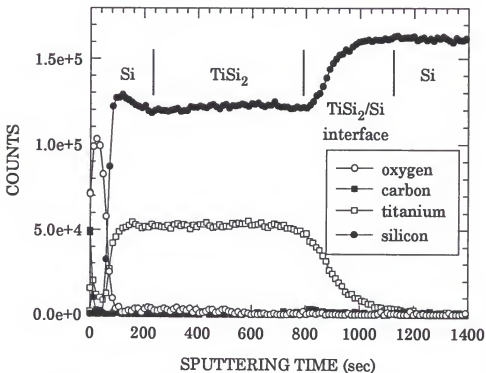


Figure 3.30. Auger electron spectra annealed  $\text{TiSi}_{2.2}$  sample.

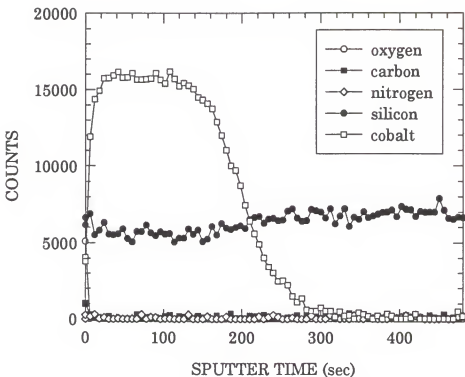


Figure 3.31. Auger electron spectra profile of the annealed  $\text{CoSi}_{0.8}$  sample.



Figure 3.32. Cross sectional TEM micrograph of the annealed  $\text{CoSi}_{0.8}$  film on silicon.

quantity in the film other than cobalt and silicon. Cobalt is not as reactive as titanium with ambient or other gases.

Representative cross sections of each of the three  $\text{TiSi}_2$  films after annealing are shown in figure 3.33. All the samples show severe roughening at the  $\text{TiSi}_2/\text{Si}$  interface. The annealed Ti (only) sample (Fig. 3.33a) and  $\text{TiSi}_{0.8}$  sample (Fig. 3.33b) both show a distinct bi-layer film formation. The top film was shown by AES and electron diffraction to be  $\text{TiO}_{x}\text{N}_{1-x}$  (cubic), while the bottom film was C54 phase  $\text{TiSi}_2$ . Due to the small thickness of the poly silicon film, the annealed  $\text{TiSi}_{2.2}$  film does not distinctly show the bi-layer film structure. However, the Auger spectra and PTEM micrograph (to be discussed later) for this sample show definitively a poly silicon film on the surface. This indicates that either the poly silicon film is very thin or discontinuous, or both. Silicide thicknesses for the annealed films could not be accurately measured because of the extreme roughness at the interface. The  $\text{CoSi}_2$  film (Fig. 3.32) clearly shows the large grain size as well as the roughening of the interface due to grain boundary wetting.

By using the amount of titanium deposited, one can calculate how much  $\text{TiSi}_2$  should form based on the data from Murarka.<sup>82</sup> The sample with Ti only should produce a  $\text{TiSi}_2$  thickness of 55 nm, while the co-deposited samples should produce 62 nm ( $\text{TiSi}_{0.8}$ ) and 70 nm ( $\text{TiSi}_{2.2}$ ) thick layers. Some of the titanium is consumed in the  $\text{TiO}_{x}\text{N}_{1-x}$  film in the Ti and  $\text{TiSi}_{0.8}$  samples, reducing the amount of titanium available to form  $\text{TiSi}_2$ . The  $\text{CoSi}_{0.8}$  (as-deposited) sample should form approximately 93 nm of  $\text{CoSi}_2$  with the area density measurements made by ion scattering. The actual  $\text{CoSi}_2$  thickness is  $> 120$  nm, indicating the deposited thicknesses cannot be used to predict final silicide thicknesses.

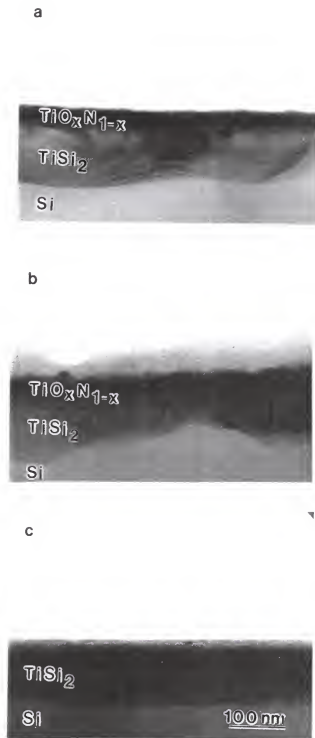


Figure 3.33. Cross sectional TEM micrographs of the annealed films: (a)  $\text{Ti}$  (only); (b)  $\text{TiSi}_{0.8}$ ; and (c)  $\text{TiSi}_{2.2}$ .

Atomic force microscopy showed that the  $\text{TiSi}_2$  films from the annealed Ti (only) and  $\text{TiSi}_{0.8}$  samples have approximately the same degree of roughening at the  $\text{TiSi}_2/\text{Si}$  interface, confirming the XTEM and AES observations. A representative plot of the underlying silicon surface from the annealed Ti (only) sample (Figure 3.34) shows the characteristic shape caused by grain boundary roughening.<sup>42</sup> The annealed  $\text{TiSi}_{2.2}$  sample showed reduced roughening at the interface as compared to the other samples (see Table 3.2).

Table 3.2 Surface roughness measurements of the annealed co-deposited samples.

composition before annealing	$\text{TiSi}_2/\text{Si}$ roughness after annealing (nm)
Ti	30.0
$\text{TiSi}_{0.8}$	27.2
$\text{TiSi}_{2.2}$	8.3

The grain sizes of the films were measured by plan view TEM. Figure 3.35 shows the grain structure of the films in the annealed Ti (only) sample. The  $\text{TiO}_x\text{N}_{1-x}$  film has a fine, equiaxed grain structure with grain sizes on the order of 10 - 40 nm (Fig. 3.35a). The  $\text{TiSi}_2$  grains are elongated platelets, and are approximately 200 - 500 nm (Fig. 3.35b). The  $\text{TiSi}_2$  grains from the annealed  $\text{TiSi}_{0.8}$  sample had a similar microstructure after annealing. The  $\text{TiSi}_2$  grains from the annealed  $\text{TiSi}_{2.2}$  sample (Fig. 3.36b) were somewhat larger in size (200 - 1,000 nm) compared to the other samples, but had the same elongated platelet structure. Note the presence of twins within the  $\text{TiSi}_2$  grains in both the micrographs. The poly silicon film was also revealed by PTEM (Fig. 3.36a), and the grains were on the order of 20 - 30 nm in size.

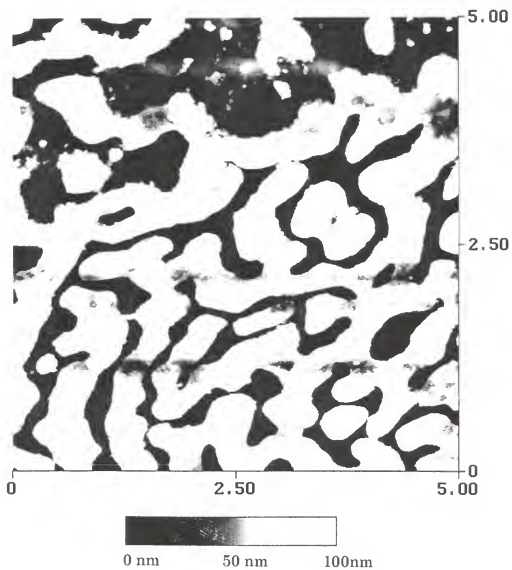


Figure 3.34. AFM micrograph of the underlying silicon surface after deposition of Ti (22 nm nominal), 850°C/1 hr/argon anneal, and removal of the film by chemical etching. The root mean square roughness is 30.0 nm.

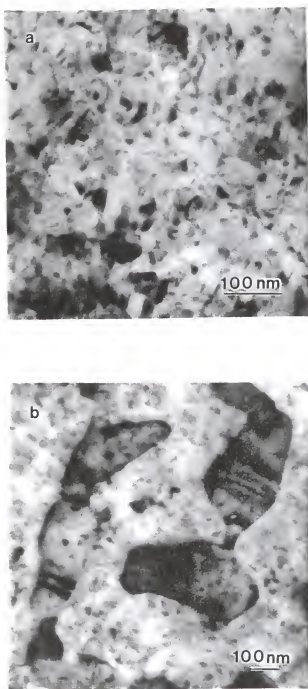


Figure 3.35. Plan view TEM micrographs of the annealed films on the annealed Ti (only) sample: (a) TiO<sub>x</sub>N<sub>1-x</sub> film; and (b) TiSi<sub>2</sub> film.

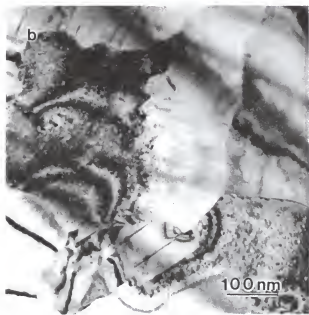
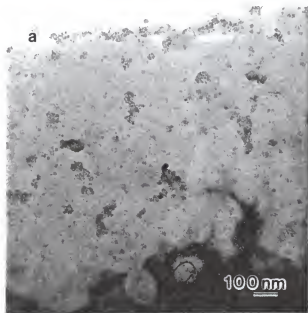


Figure 3.36. Plan view TEM micrographs of the annealed films on the annealed  $\text{TiSi}_{2.2}$  sample: (a) poly Si film; and (b)  $\text{TiSi}_2$  film.

By etching from the backside of the wafer, one can able to image both the  $\text{TiO}_x\text{N}_{1-x}$  or poly Si film and the  $\text{TiSi}_2$  film (Figure 3.37). The  $\text{TiSi}_2$  was imaged in area 1 while the  $\text{TiO}_x\text{N}_{1-x}$  or poly silicon images were acquired from area 2.

Residual wafer flexure was measured in the samples after annealing through the technique described in the Phillip's manual.<sup>70</sup> Table 3.3 shows the measured wafer curvatures from the three samples.

Table 3.3 Residual wafer curvature of the annealed co-deposited films.

composition before annealing	wafer curvature after annealing (m)
Ti	53.4
$\text{TiSi}_{0.8}$	238.3
$\text{TiSi}_{2.2}$	30.9

The two samples with  $x < 2$  ( $\text{TiSi}_x$ ) showed a smaller residual wafer curvature, indicating that the substrate had a small residual stress, while the Si-rich ( $x > 2$ ) composition had a large residual wafer curvature indicating large stress in the substrate.

### 3.7.3 Discussion

Only the "silicon-deficient" ( $x < 2$ ) compositions formed a top film of  $\text{TiO}_x\text{N}_{1-x}$ . This is explained by the need for silicon to diffuse across the growing silicide film to form more  $\text{TiSi}_2$ ,<sup>72</sup> allowing time for the competing  $\text{Ti} + \text{O} + \text{N} \rightarrow \text{TiO}_x\text{N}_{1-x}$  reaction to occur in the Ti and  $\text{TiSi}_{0.8}$  (as-deposited) samples. The "silicon-rich" sample (as-deposited) had only to crystallize into the C54  $\text{TiSi}_2$  phase with minimal diffusion distances for silicon.

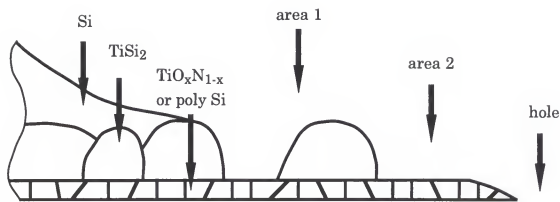


Figure 3.37. Schematic cross section of a plan view TEM sample.

The observation that the surface film is  $\text{TiO}_x\text{N}_{1-x}$  and not TiN is based on the AES profiles and electron diffraction data. Oxygen was shown to be prevalent throughout the top film and had not, therefore, been "snowplowed" to the interface.<sup>72</sup> Electron diffraction showed that the film has the cubic structure of TiN, indicating that oxygen is substituting on nitrogen sites (Fig. 3.2). It is possible that the oxygen is present in some other form, such as  $\text{TiO}_2$ , in such small amounts that it was not evident in the electron diffraction patterns. Desu and Taylor<sup>73</sup> found that annealing titanium on silicon in argon at 950°C results in a TiN and not  $\text{TiO}_x\text{N}_{1-x}$  film on top of  $\text{TiSi}_2$ . Jongste et al.<sup>91</sup> also found oxygen in between TiN and  $\text{TiSi}_2$  when titanium films on silicon were annealed at 700°C in  $\text{N}_2$ . Morgan et al.<sup>72</sup> however, found that  $\text{TiO}_x\text{N}_{1-x}$  forms on top of C54  $\text{TiSi}_2$  when annealed above 800°C, sometimes with a small amount of silicon on the surface, in agreement with these findings. It is possible that the purity of the gases in the annealing ambient can explain the differences in composition in the different studies. Jongste et al.<sup>91</sup> also showed that when titanium films are capped with silicon, only  $\text{TiSi}_2$  and no TiN forms upon annealing, similar to the annealed  $\text{TiSi}_{2.2}$  sample in this study.

The film on top of the  $\text{TiSi}_2$  film in the annealed  $\text{TiSi}_{2.2}$  sample is identified as poly silicon, based on the AES profile and the grain structure (Figure 3.34a). This finding shows that at least some of the "excess" silicon has diffused to the free surface of the  $\text{TiSi}_2$  film. The data in section 3.5 has shown that this sample does not result in a larger supersaturation of vacancies in the silicon substrate than in the other samples. Honeycutt et al.<sup>53</sup> speculated that silicon diffusing across the grain boundaries of  $\text{TiSi}_2$  films can be responsible for a continued vacancy injection, which these results,

contradict. No real difference was seen in the point defect behavior in the underlying silicon despite the large difference in grain sizes of the films.

The reduced interface roughening in the annealed  $\text{TiSi}_{2.2}$  sample cannot be explained by the difference in grain size in this sample as compared to the others. Indeed, one would expect that a larger grain size would produce more severe roughening, as interface roughening is due to faceting of the grains.

One can only speculate as to why the  $\text{TiSi}_2$  grains in the "silicon-rich" sample after annealing are larger than in the other samples. It is possible grain growth may have been more rapid in this sample due to the readily available silicon or that the  $\text{TiO}_x\text{N}_{1-x}$  layer in the other samples acts to somehow retard grain growth. Since some titanium is consumed in the  $\text{TiO}_x\text{N}_{1-x}$  film, the  $\text{TiSi}_{2.2}$  (as-deposited) sample has a thicker  $\text{TiSi}_2$  film after annealing which could encourage the growth of larger grains.

Svilan et al.<sup>84</sup> have shown that  $\text{TiSi}_2$  film formation results in a residual tensile stress after annealing. All of these samples also showed a positive residual tensile stress in the film. The difference in wafer curvature is in rough agreement with a previous study by Murarka and Fraser.<sup>92</sup> Murarka and Fraser showed that "excess" silicon deposited with titanium leads to less tensile stress when the phase changes from  $\text{Ti} + \text{Si}$  to  $\text{TiSi}_2$ . They speculated that as the "excess" silicon reaches a critical value, silicon interstitials in the  $\text{TiSi}_2$  lattice create a compressive stress. Also, since Murarka and Fraser determined the Si:Ti ratio by sputtering parameters, which is known to be inaccurate for composition determination, the actual composition of their samples may have been different from what they reported. Shor and Pelleg<sup>93</sup> postulated that a  $\text{TiO}_x\text{N}_{1-x}$  film acts to counteract the residual tensile stress of the  $\text{TiSi}_2$  film, which this work

supports. Since no experimental determination of the amount of strain that a silicon interstitial exerts on the  $\text{TiSi}_2$  lattice has been made and it is not possible to quantify how much of the excess silicon has diffused to the free surface, *a priori* either theory cannot be confirmed. Based on the wafer curvature on these samples, the high degree of curvature seen in the  $\text{TiSi}_{2.2}$  (as-deposited) sample after annealing is believed due to the absence of a  $\text{TiO}_x\text{N}_{1-x}$  film.

### 3.8 Summary

The series of experiments reported in this chapter have established that the formation and anneal of a  $\text{TiSi}_2$  film results in a slight vacancy supersaturation and interstitial undersaturation in the underlying silicon at temperatures ranging from 800 to 890°C. The vacancy supersaturation is approximately  $\frac{C_V}{C_V^*} \sim 1.5$  and the interstitial undersaturation is approximately  $\frac{C_I}{C_I^*} \sim 0.3$  after annealing for 1 hour at 840°C and was generally unchanged in the temperature range 800 to 890°C. The vacancy supersaturation was found to be independent of film thickness and at least partially continuous with longer annealing times at 800°C. Initial composition of the film ( $\text{TiSi}_x$  with  $0 \leq x < 3$ ) was found not to have a major influence on the point defect perturbation. With these results, three proposed mechanisms of point defect generation in silicon with a  $\text{TiSi}_2$  film were discarded: volume contraction at the  $\text{TiSi}_2/\text{Si}$  interface, stress compensation in the substrate, and the diffusing species during film growth. Earlier conflicting reports of a huge vacancy supersaturation caused by  $\text{TiSi}_2$  film

growth were explained by SIMS depth profile artifacts produced by sputtering through a rough interface.

## CHAPTER 4

### EXTRINSIC DISLOCATION LOOP BEHAVIOR IN SILICON WITH A SILICON NITRIDE OR TITANIUM DISILICIDE FILM

#### 4.1 Introduction

End-of-range (EOR) dislocation loops are typically observed in ion implanted silicon at doses above the amorphization threshold.<sup>4</sup> These loops are thermally stable up to about 950°C, when they begin to dissolve and supply interstitials to the bulk.<sup>60</sup> Below 950°C, they are relatively stable. It has been shown that loops can act as "detectors" of interstitial supersaturations due to ion implantation and oxidation by capturing excess interstitial fluxes and increasing in size.<sup>62,94</sup> This growth can be measured by TEM.

In this chapter, the accelerated dissolution of dislocation loops will be used as a detector of vacancy supersaturations due to the presence of silicon nitride or titanium disilicide films. It will be established in the first section that vacancy-loop combinations do not have a significant energy barrier, are essentially diffusion rate limited, and are therefore accurate measures of the vacancy flux. The second and third sections measure loop dissolution in silicon with a thermally grown silicon nitride film and titanium disilicide film, respectively. Measurements of the relative vacancy supersaturation is extracted from enhanced loop dissolution, and these values are compared to the values measured by antimony diffusion.

#### 4.2 Antimony and Boron Diffusion Behavior in Ge<sup>+</sup> implanted Silicon Annealed in NH<sub>3</sub>

In this experiment, doping superlattice samples were implanted with Ge<sup>+</sup> and annealed (anneal #1) to form end-of-range loops. Some of the samples were then further annealed (anneal #2) in NH<sub>3</sub> to form a silicon nitride film, which provides a source of vacancies to the substrate. Dopant diffusivities were extracted in the doping spikes and compared to one another above and below the loop layer, relative to the surface. Other doping superlattice samples were implanted, but anneal #2 was performed in argon (inert - no vacancy injection), while other samples were not implanted but has similar anneals.

##### 4.2.1 Experimental

The first set of antimony doping superlattice samples were implanted to a dose of  $1 \times 10^{15}/\text{cm}^2$  with Ge<sup>+</sup> at an energy of 140 keV and 7° tilt. The beam current was held to less than  $1 \mu\text{A}/\text{cm}^2$  to minimize wafer heating. The samples were cleaned by a dilute HF (1:20) dip prior to furnace entry. The samples were annealed at 800°C for 60 minutes in N<sub>2</sub> (99.999% purity) to recrystallize the amorphized region and form the loop layer (anneal #1). Samples were further annealed at 910°C for 30 minutes in flowing NH<sub>3</sub> (99.9995% purity - anneal #2). A second set of implanted samples had an identical anneal #1, but had anneal #2 done in argon (99.95% purity) at the same time and temperature as the first set of samples. A third set of samples received no implant but were annealed under the same conditions as

the first set of samples. A list of samples and annealing sequence is provided in Table 4.1.

Table 4.1. Sample description for section 4.2.

sample id	dopant	implant	anneal #1	anneal #2
Sb1	Sb	no	800°C/1 hr/N <sub>2</sub>	910°C/0.5 hr/Ar
Sb2	"	no	"	910°C/0.5 hr/NH <sub>3</sub>
Sb3	"	yes	"	910°C/0.5 hr/Ar
Sb4	"	yes	"	910°C/0.5 hr/NH <sub>3</sub>
B1	B	no	"	910°C/0.5 hr/Ar
B2	"	no	"	910°C/0.5 hr/NH <sub>3</sub>
B3	"	yes	"	910°C/0.5 hr/Ar
B4	"	yes	"	910°C/0.5 hr/NH <sub>3</sub>

#### 4.2.2 Results/Discussion

The SIMS depth profiles of antimony and boron from the samples without an implant are shown in figure 4.1. The diffusion of antimony is clearly enhanced in sample Sb2 annealed in NH<sub>3</sub> compared to sample Sb1 annealed in argon, with  $\frac{D_{Sb}^{int,NH_3}}{D_{Sb}^{int,Ar}} \sim 4$ . This indicates a vacancy

supersaturation due to the NH<sub>3</sub> ambient. Boron's diffusion is retarded, with

$$\frac{D_B^{int,NH_3}}{D_B^{int,Ar}} \sim 0.5$$
, indicating an interstitial undersaturation due to the NH<sub>3</sub> ambient. These values are in agreement with previous measurements by

Mogi et al.<sup>83</sup>

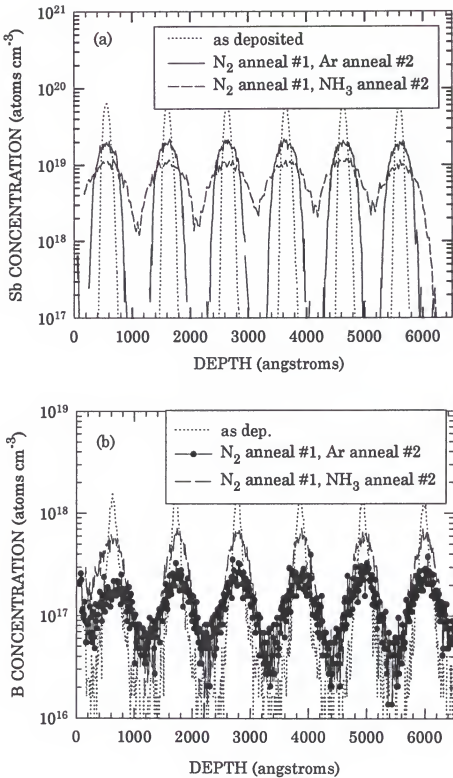


Figure 4.1. SIMS depth profiles of doping superlattices annealed without an implant. (a) antimony; and (b) boron.

Figure 4.2 shows antimony and boron SIMS depth profiles in the samples that were implanted. It is apparent that the  $\text{Ge}^+$  implant has resulted in a vacancy undersaturation in both sets of samples when compared to the set that did not receive an implant. Antimony diffusion is severely retarded in both samples compared to the samples that did not receive an implant ( $\frac{D_{\text{Sb}}^{\text{int, implant}}}{D_{\text{Sb}}^{\text{int, no implant}}} \sim 0.1$ ). There are two possible reasons for this

behavior. One possibility is that the vacancy undersaturation is a response to the interstitial supersaturation caused by the implant. The vacancy undersaturation could be a result of satisfying the equilibrium condition  $C_V C_I = C_V^* C_I^*$  with vacancies recombining with interstitials to maintain equilibrium. The 910°C "film anneal" temperature is in the range where I-V recombination is thought to be efficient.<sup>7,15</sup> Another possibility is that the presence of germanium causes a vacancy undersaturation. A recent report by Larsen and Kringshøj<sup>95</sup> found that antimony diffusion was enhanced in  $\text{Si}_{1-x}\text{Ge}_x$  alloys with increasing germanium content. Germanium should then act to increase antimony diffusion which is opposite to the behavior observed. While the  $\text{Si}_{1-x}\text{Ge}_x$  alloys examined by Larsen and Kringshøj had much higher germanium contents than the ion implanted samples examined in this work, it appears more likely that the first explanation is responsible for the behavior observed. Figure 4.2b shows the SIMS depth profiles of boron in an implanted sample. The sample that was implanted has a large interstitial supersaturation. The profile has flattened (i.e. boron has diffused very far) and it is impossible to extract a diffusivity for boron in either of the implanted samples. It is interesting to note that the higher concentration of boron at 160 nm, is coincident with the loop layer. Boron appears to be

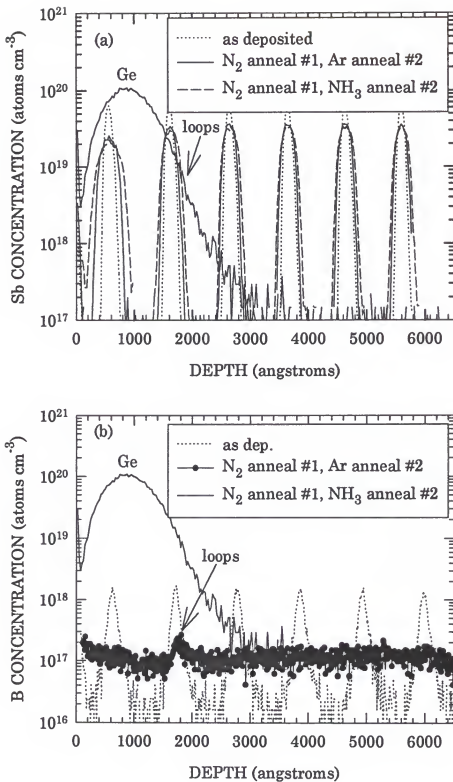


Figure 4.2. SIMS depth profiles of doping superlattices annealed with an implant. (a) antimony; and (b) boron.

segregating to the loops to a small degree, becoming immobile when it is in the loops, in line with previous results.<sup>96</sup>

Even with the vacancy undersaturation, the efficiency of the loops in capturing vacancies can be evaluated. Figure 4.2a shows antimony diffusion behavior when the second film anneal is done in NH<sub>3</sub> instead of argon. As can be clearly seen, antimony diffuses much more in the shallowest spike above the loop layer than in the spikes deeper than the loop layer. Comparing the normalized antimony diffusivities (figure 4.3) shows that the first spike has  $\sim 4x$  the diffusivity of the deeper spikes. This indicates the loops are capturing most of the vacancies produced.

A random walk model for vacancy diffusion would indicate that a significant fraction of the vacancies should diffuse through the loop layer without recombining, given that the loop area coverage in the (100) plane is  $\sim 30\%$ . That this does not happen shows that in fact there is some attraction between the vacancies and the loops that encourages recombination. The opposite strain states of the defects serves as that attractive force.<sup>61</sup> Previous work by Park and Law<sup>97,98</sup> estimated the pressure that existed around an extrinsic dislocation loop layer and found that it could in fact attract interstitials due to the net reduction in overall strain from a "free" interstitial joining the loop. This was confirmed in an experiment similar to this one by Listebarger et al.<sup>62</sup> and Chao et al.<sup>99</sup> Their work showed that interstitial-extrinsic dislocation loop combinations are diffusion limited. This work shows that vacancy-extrinsic dislocation loop combination is also diffusion limited.

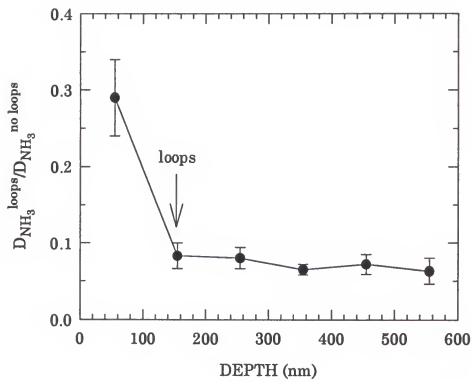


Figure 4.3. Normalized antimony diffusivities in loop samples with anneal #2 in NH<sub>3</sub>.

#### 4.3 Extrinsic Dislocation Loop Behavior in Silicon with a Thermally Grown Silicon Nitride Film

In this experiment, the behavior of pre-existing extrinsic dislocation loops in silicon samples annealed in either argon or  $\text{NH}_3$  at 810 and 910°C was studied. Samples annealed in  $\text{NH}_3$  form a silicon nitride ( $\text{SiN}_x$ ) film. Through observation of the dislocation loop behavior, insight can be gained as to how the population of point defects changes during a particular processing step.

It has been established in the preceding section and by others that the growth of a thermal  $\text{SiN}_x$  film results in a vacancy supersaturation and an interstitial undersaturation in the underlying silicon.<sup>6,21,83</sup> In a previous study, Mogi et al.<sup>83</sup> showed that the growth and anneal of a silicon nitride film on silicon resulted in  $\frac{C_V}{C_V^*} \sim 5$  and  $\frac{C_I}{C_I^*} \sim 0.2$  at a temperature of 910°C.

These values were determined by measuring the diffusivity of antimony and boron in silicon doping superlattices. The primary quantity measured in the dopant marker experiments is the relative supersaturation or undersaturation of point defects. In principle, the act of detection requires point defect - dopant binding energies be taken into account. While it has been shown in doping superlattices of boron that the act of detection by itself does not perturb the point defect population,<sup>67</sup> the dislocation loop method eliminates the need to even consider this.

The primary quantity measured is the *flux* of point defects introduced by a processing step such as thin film formation on the substrate surface. However, one must account for the fraction of loop dissolution/growth caused by a change in the population of both kinds of point defect. For example, loop dissolution can be attributed to vacancy supersaturation or interstitial

undersaturation.<sup>100</sup> While this problem can be ignored for studies in which the change in population of one point defect far exceeds that of the other, as occurs after ion implantation,<sup>19</sup> it cannot be ignored for studies in which the relative changes in the point defect populations are smaller and similar in magnitude, as is the case here.

#### 4.3.1 Experimental

A Czochralski grown p-type silicon wafer ( $\rho < 100 \Omega\text{-cm}$ ) was implanted with 140 keV Ge<sup>+</sup> ions to a dose of  $1 \times 10^{15} \text{ cm}^{-2}$  in order to amorphize the Si. The beam current was kept below  $1 \mu\text{A cm}^{-2}$  to limit possible wafer heating. The wafer was annealed in flowing N<sub>2</sub> (99.999% purity) at 800°C for 1 hour to recrystallize the amorphized region and form the EOR loops. Annealing under these conditions has been previously shown to return the point defect population to equilibrium after the disturbance caused by ion implantation.<sup>61</sup> The annealed wafer was diced and cleaned by a dilute HF (1:20) dip just prior to furnace entry. Half the samples were annealed in a quartz tube furnace with flowing NH<sub>3</sub> (99.9995% purity) at one atmosphere, with 25 standard cm<sup>3</sup>/sec gas flow at temperatures of 810°C and 910°C and times ranging from 30 to 180 minutes. The second set of samples were annealed in argon (99.95% purity) for the same times and temperatures, and were used as controls.

Quantitative analysis of the dislocation loops was performed using weak beam dark field (g<sub>220</sub>) PTEM micrographs. All the loops were measured in a representative area of  $\sim 1 \mu\text{m}^2$  in each sample. Loop diameters were measured in increments of 5 nm from 10 to 70 nm by measuring the longest axis on the loop. The total number of loops of each size was multiplied by the

area of that size loop and the area added to get the total area of the loops. Previous experiments have shown the loops tend to lie on {111} planes.<sup>2,9</sup> The net density of silicon interstitials bound by the loops in each sample was calculated by multiplying the area bound by the loops by  $1.6 \times 10^{15}/\text{cm}^2$ . The details of the analysis, as well as error measurements, have been described in greater detail by Listebarger et al.<sup>62</sup>

#### 4.3.2 Results/Discussion

A typical XTEM micrograph of the film and loop layer is shown in figure 4.4. The dislocation loop layer is approximately 160 nm below the surface and the layer is 30 nm wide. The thickness of the film was measured to be 4 nm from the sample annealed at 910°C for 180 minutes (fig. 4.5). This provides a maximum for the thicknesses of all films grown since it had the longest time and highest temperature anneal. Little variation of the thickness was seen in samples annealed at 810°C for the shorter times. This is in agreement with previous results on thermally grown nitride films.<sup>101</sup>

##### 4.3.2.1 Loop Distributions

The samples are divided into those that were annealed in NH<sub>3</sub> (nitrided) and those that were annealed in argon (controls - no film). Plan view TEM micrographs of the dislocation loop evolution during anneal in NH<sub>3</sub> and Ar are shown in figure 4.6. The loops show an increase in average size and a decrease in density in both sets of samples with temperature and annealing time. The size distributions of the loops are plotted in figures 4.7 and 4.8. The loops in the 810°C Ar annealed samples do not show significant



Figure 4.4. Cross sectional TEM (bright field,  $g_{220}$ ) micrograph of the loop layer and silicon nitride film.

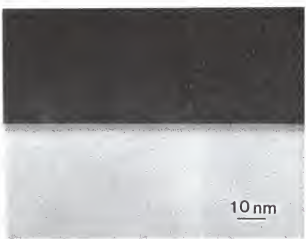


Figure 4.5. Cross sectional high magnification TEM (bright field,  $g_{220}$ ) micrograph of the silicon nitride film. Sample has been annealed  $910^{\circ}\text{C}/3$  hrs/ $\text{NH}_3$ .

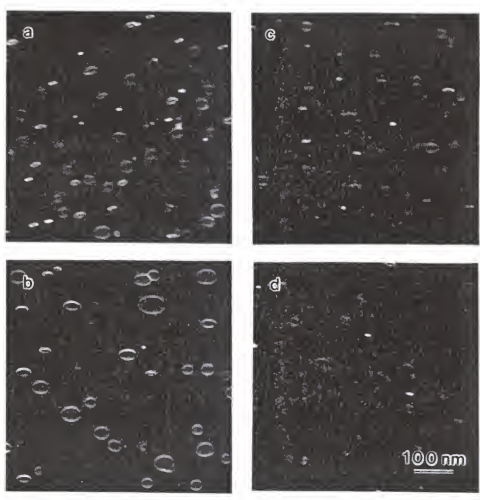


Figure 4.6. Plan view TEM (weak beam dark field,  $g_{220}$ ) micrographs in samples annealed in various conditions. (a) 910°C/0.5 hr/Ar; (b) 910°C/3 hrs/Ar; (c) 910°C/0.5 hr/NH<sub>3</sub>; and (d) 910°C/3 hrs/NH<sub>3</sub>.

coarsening (fig. 4.7a). The relatively small shift in the peak density of loop sizes from 20 to 25 nm in the 30 minute to 180 minute anneal, respectively, is indicative of this. The loops in the 910°C Ar anneal show a more distinctive shift to larger sizes with annealing. While the shift to larger loop sizes is subtle, the number of interstitials bound in the larger loops increases rapidly due to the  $r^2$  dependence. The reduction in the amount of loops with the most common size diameter from figures 4.7a to 4.8a and 4.7b to 4.8b indicates non thermal dissolution of the loops is occurring in the samples annealed in NH<sub>3</sub>. While the loop density at the peak of the distribution decreases with time, the loop diameter corresponding to the peak increases.<sup>102</sup>

Little thermal dissolution of the loops is occurring at 810°C and 910°C in the argon annealed samples, as observed by the constancy of the net interstitials bound by the loops (fig. 4.9). The peak height shows a large statistical error associated with it and no conclusion can be drawn from it. However, the integrated area under the peak shows unequivocally that thermal dissolution is not occurring in the control samples. Also, it can be concluded that the loops are in a coarsening regime. The nitrided samples show a net decrease in interstitials bound by the loops. A comparison of the loop distribution between argon and NH<sub>3</sub> annealed samples shows that nitridation results in loop dissolution. Loop coarsening in the nitrided samples must then compete with non-thermal loop dissolution. In order to estimate the extent of coarsening, the weighted average loop radii (normalized to the density of interstitials bound by a particular size loop) is shown in figures 4.10a and b. The weighted average loop radii is calculated by:

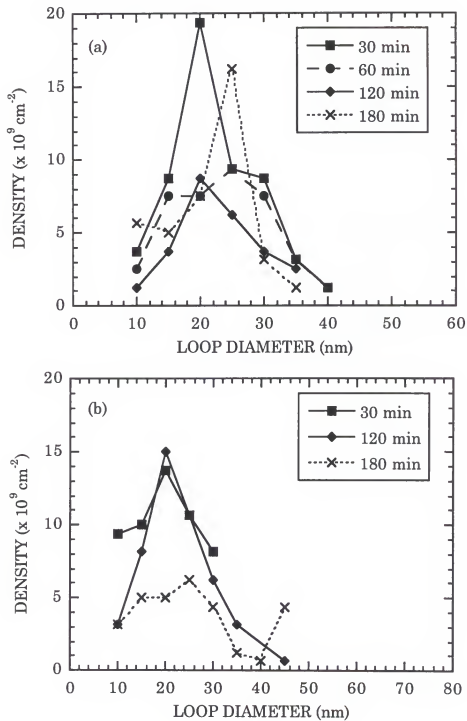


Figure 4.7. Size distributions of the loops in samples annealed in argon. (a) 810°C; and (b) 910°C.

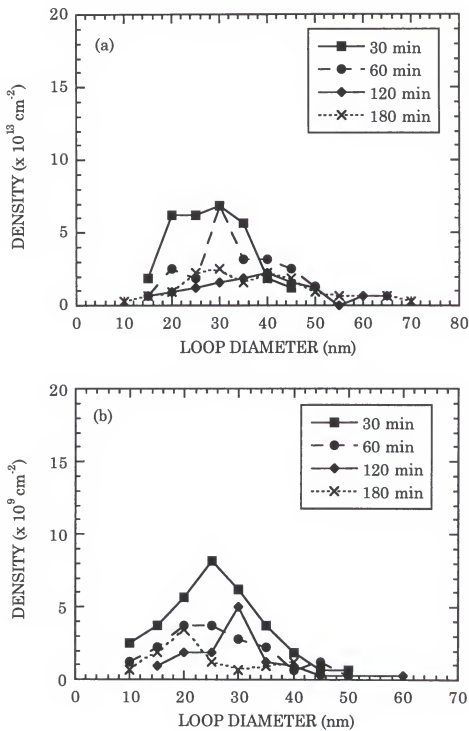


Figure 4.8. Size distributions of the loops in samples annealed in  $\text{NH}_3$ . (a) 810°C; and (b) 910°C.

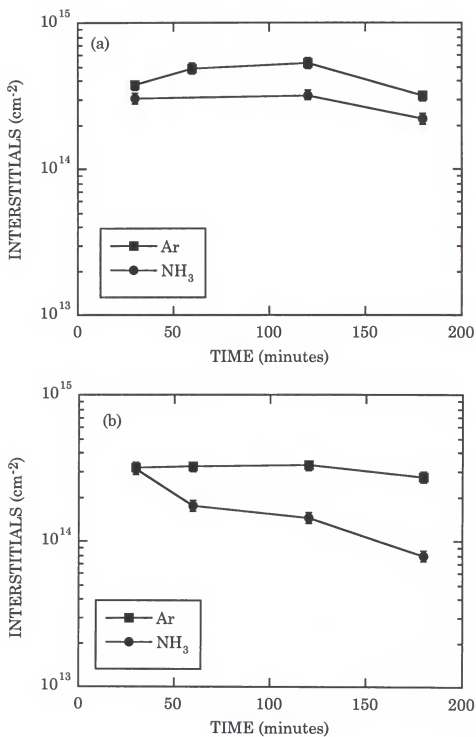


Figure 4.9. Net interstitials bound by the loops annealed at (a)  $810^\circ\text{C}$ ; and (b)  $910^\circ\text{C}$ .

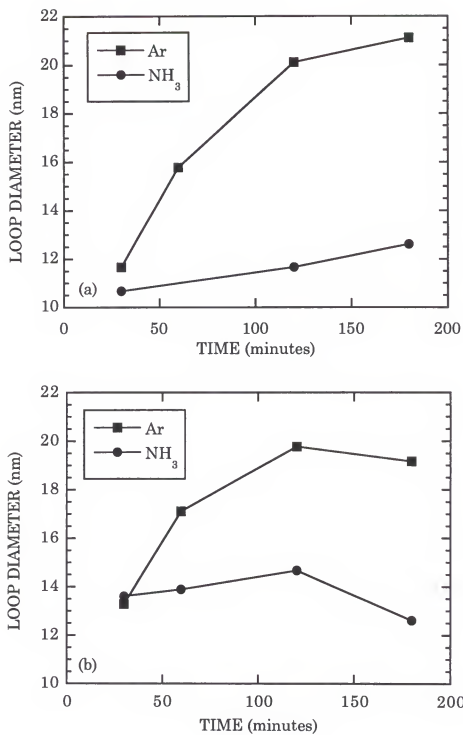


Figure 4.10. Average loop diameter normalized by the area of each loop in samples annealed at (a) 810°C; and (b) 910°C.

$$r_{\text{weighted}} = \sqrt{\frac{\sum n_i r_i^2}{\sum n_i}} \quad (4.1)$$

where  $n_i$  is the area density of loops with a radius  $r_i$ . This method normalizes the loop radius by the amount of interstitials bound by the loops of each size. The figures show that the loops in the control samples annealed in argon coarsen to a greater extent than the loops in the samples annealed in  $\text{NH}_3$  at both anneal temperatures, which again demonstrates that loop dissolution in the nitrided samples dominates over coarsening. The dissolution can be explained by vacancy supersaturation and/or interstitial undersaturation caused by the presence of the nitride film.

#### 4.3.2.2 Point Defect - Loop Interaction

Extrinsic loop dissolution via point defects can occur by a vacancy supersaturation and/or interstitial depletion.<sup>100</sup> Each case is examined individually.

##### 1. Vacancy supersaturation

By assuming that a flux,  $\Phi$ , of vacancies from the  $\text{SiN}_x$  film to the bulk is completely captured and annihilated by the loops and that all loop dissolution is due to loop-vacancy interaction, one can integrate the flux over the distance via:

$$\int_0^d \Phi dx = (C_V - C_V^*) D_V \quad (4.2)$$

where  $\Phi$  is the number of interstitials lost by the loops per unit area and time,  $d$  is the distance from the interface to the loop layer,  $(C_V - C_V^*)$  is the supersaturation of vacancies above equilibrium, and  $D_V$  is the diffusivity of vacancies. This calculation assumes a constant flux over time and a negligible free interstitial (I)- free vacancy (V) recombination. It was shown that vacancy - dislocation loop recombination is diffusion limited rather than reaction rate limited in the first section. The expression for  $\Phi$  is then:

$$\Phi = \frac{\text{interstitials}_{\text{loops}}^{\text{Ar}} - \text{interstitials}_{\text{loops}}^{\text{NH}_3}}{\text{time}} \quad (4.3)$$

A schematic of the vacancy profile is shown in figure 4.11a. The average integrated  $\Phi$  value is shown in Table 4.2.

Table 4.2. Comparison of point defect values measured by the loop method and antimony diffusion.

910°C (60 min)	
$\int_0^d \Phi dx$ (this study)	$(6.4 \pm 1.7) \times 10^5 \left( \frac{\text{vac}}{\text{cm} \cdot \text{sec}} \right)$
$C_V^* D_V$ (ref. 7)	$2.0 \times 10^5 \left( \frac{\text{vac}}{\text{cm} \cdot \text{sec}} \right)$
$\frac{C_V}{C_V^*}$ (ref. 83)	$3.8 \pm 1.4$
$\frac{C_V}{C_V^*}$ (this study)	$4.2 \pm 0.9$

A slight decline in integrated  $\Phi$  values is found with time at 910°C as shown in figure 4.12, and is in agreement with the results of Mogi et al.,<sup>83</sup> who did

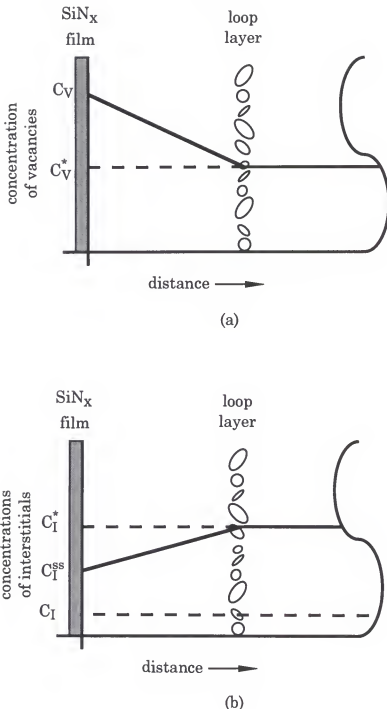


Figure 4.11. Schematic of the point defect profiles in loop samples. (a) vacancy; and (b) interstitial.

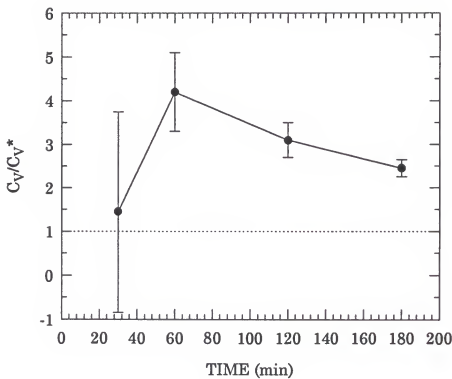


Figure 4.12. Extracted  $C_V/C_V^*$  values by the loop method in silicon annealed  $910^\circ\text{C}/\text{NH}_3$  for various times.

not find a significant change in the enhancement of  $D_{Sb}$  with continued annealing at 810 and 910°C.

Using a  $C_V^* D_V$  value from the estimates by Tan and Gösele,<sup>7</sup> the loop results are now compared to those found by antimony diffusion in the previous study by Mogi et al.<sup>83</sup> The analysis is limited to the 910°C annealed samples because they are the only directly comparable data set. Using the integrated flux values and the  $C_V^* D_V$  estimates, a value for  $\frac{C_V}{C_V^*}$  is extracted (Table 4.2). The  $\frac{C_V}{C_V^*}$  values from the two methods show excellent agreement.

Since the methods used to estimate vacancy supersaturations were based on completely different physical phenomena, confidence in the values extracted is high. This is useful in light of the fact that reported literature values for point defect parameters, for example, interstitial diffusivities, extend over several orders of magnitude.<sup>103</sup> Hence it is concluded that loop dissolution in silicon can be explained by a vacancy supersaturation on the order of  $\frac{C_V}{C_V^*} \sim 4.2$  in an  $NH_3$  ambient after a one hour anneal at 910°C.

## 2. Interstitial undersaturation

The situation is more complex for an interstitial undersaturation-induced dislocation loop shrinkage. In this case, interstitials are leaving the loops to replenish an undersaturation in the area between the loops and  $SiN_x/Si$  interface, so the integrated flux values measure the rate at which interstitials are supplied to this region. In analogy to the vacancy-induced loss, it is assumed that (1) the lost interstitials by the loops are due solely to the interstitial undersaturation in the near-surface region, and (2) negligible

I-V recombination. With assumption (1), it would appear at first glance that one could measure a  $\frac{C_I}{C_I^*}$  value in direct analogy to the measurement of  $\frac{C_V}{C_V^*}$ .

Nevertheless, a  $\frac{C_I}{C_I^*}$  value cannot be extracted because the relative strength of

surface recombination vs. the ability of the loops to supply interstitials is not known. While the interface attempts to maintain a value of  $C_I^s$ , the loops attempt to supply interstitials to achieve equilibrium,  $C_I^*$ . The actual value of  $C_I$  at the interface is therefore some concentration  $C_I^{ss}$ , where  $C_I \leq C_I^{ss} \leq C_I^*$ . Figure 4.10b shows a schematic of depth profiles of the interstitial population and captures the difficulty in measuring a true  $C_I$  in this system by using dislocation loops. Even if a flat profile for the interstitial concentration is assumed in the near-surface region, a value for  $\frac{C_I}{C_I^*}$  cannot be

derived because  $C_I^{ss}$  is unknown.

Through several indirect observations it is concluded that interstitial undersaturation-induced loop dissolution can be disregarded. The number of interstitials bound by the loops is approximately constant, even with a rise in temperature from 700 to 840°C, indicating that the loops are not supplying a significant amount of interstitials to account for the increase in  $C_I^*$ . An estimate by Tan and Gösele<sup>8</sup> yields  $C_I^*(810^\circ\text{C}) = 3 \times 10^9/\text{cm}^3$  and  $C_I^*(910^\circ\text{C}) = 9 \times 10^{10}/\text{cm}^3$ . This substantial increase must instead be supplied by surface or bulk processes. An estimate of the magnitude of interstitial undersaturation-induced loop dissolution can be made from the values of loop growth in an interstitial supersaturation. It is noted that by using doping superlattices, the previous study by Mogi et al.<sup>36</sup> measured  $\frac{C_I}{C_I^*} \sim 0.2$  with

annealing in NH<sub>3</sub> at 910°C. A previous report by Park et al.<sup>94</sup> studied the

growth of extrinsic dislocation loops in silicon during dry oxidation of the surface. The relative supersaturation of interstitials at 900°C was estimated to be  $\frac{C_I}{C_I^*} \sim 10$ . With 1000% more interstitials present than at

equilibrium, the number of interstitials bound by the loops increases by 60%, from  $3.5 \times 10^{14}/\text{cm}^2$  to  $5.5 \times 10^{14}/\text{cm}^2$ , after 1 hour at 900°C. Given the relative magnitude of these values, we would therefore expect that a depletion of 80% of the original interstitial population to contribute little to the measured loop dissolution. Lastly, an interstitial leaving the loop experiences a larger barrier than an interstitial combining with a loop. Previous reports have shown little barrier to interstitial-loop combinations,<sup>63,98</sup> but the estimate by Park et al.<sup>94</sup> indicates that this is not the case for interstitials leaving the loop. Interstitials leaving the loop experience a pressure difference due to the tension surrounding the loop, which acts as a barrier for loop dissolution.

#### 4.4 Extrinsic Dislocation Loop Behavior in Silicon with a Titanium Disilicide Film

This experiment measures dislocation loop dissolution in silicon annealed with a  $\text{TiSi}_2$  film through the examination of extrinsic dislocation loops. Loop behavior in silicon annealed with and without a thermally grown  $\text{TiSi}_2$  film is compared. By studying the net density of interstitials bound by the loops, the degree of enhanced loop dissolution in samples with a  $\text{TiSi}_2$  film can again be explained by the supersaturation of vacancies.

#### 4.4.1 Experimental

A Czochralski grown p-type Si wafer ( $\rho < 100 \Omega\text{-cm}$ ) was implanted with 140 keV  $\text{Ge}^+$  ions to a dose of  $5 \times 10^{14} \text{ cm}^{-2}$  in order to amorphize the Si. The beam current was kept below  $1 \mu\text{A}/\text{cm}^2$  to limit possible dose-rate effects. The wafer was annealed in flowing  $\text{N}_2$  (99.999% purity) at  $800^\circ\text{C}$  for 1 hour to recrystallize the amorphized region and form the EOR loops. The wafer was cleaned in TCA, methanol, acetone, de-ionized (DI) water, Buffered Oxide Etch (10:1), and DI water in that sequence, to remove organic debris and the native oxide. The wafer was diced into two halves, with one half immediately loaded in an electron beam deposition chamber which was pumped down to a vacuum better than  $5 \times 10^{-6}$  Torr. Titanium (99.9% purity) was then evaporated onto the sample to a thickness of 30 nm. Both halves were immediately placed in a furnace in flowing forming gas (97%  $\text{N}_2$  + 3%  $\text{H}_2$ ) and annealed at  $700^\circ\text{C}$  for 20 minutes to form the silicide on the half with titanium. The halves were subsequently diced and annealed in forming gas at 700 to  $890^\circ\text{C}$  for 1 to 4 hours to get significant point defect diffusion to the loop layer from the  $\text{TiSi}_2/\text{Si}$  interface. Samples with loops but without titanium were annealed concurrently and used as control specimens. Samples for plan view TEM (PTEM) were prepared after the  $\text{TiSi}_2$  film was removed by dipping in dilute HF (25%) for several minutes. Quantitative analysis of the dislocation loops was performed using the method described in the previous section.

#### 4.4.2 Results and Discussion

Figure 4.13 shows the typical microstructure of a sample with a silicide film. The distance from the  $\text{TiSi}_2/\text{Si}$  interface to the loops is approximately

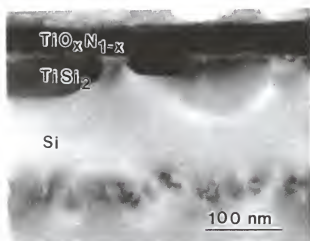


Figure 4.13. Cross sectional TEM (bright field,  $g_{220}$ ) micrograph of the loop layer and  $\text{TiSi}_2$  film.

120 nm. It was again confirmed by electron diffraction and Auger Electron Spectroscopy that the 700°C 20 minute anneal produced C54 TiSi<sub>2</sub> film with a TiO<sub>x</sub>N<sub>1-x</sub> film on top. Representative PTEM micrographs of the loops are shown in figure 4.14.

To calculate the effect of the TiSi<sub>2</sub> film on point defects, the net density of interstitials bound by the loops in the samples with a TiSi<sub>2</sub> film was subtracted from the net density of interstitials bound by the loops in the control samples (no TiSi<sub>2</sub> film), the same method used in the preceding section. Figure 4.15 shows that the loops in the silicided samples are losing interstitials at an enhanced rate at 840 and 890°C. Both sets of samples annealed at 700°C show the same amount of interstitials bound by the loops. This is attributed to the smaller value of vacancy diffusivity, and therefore, further discussion is confined to the 840 and 890°C samples. While net shrinkage of the loops is smaller than in the preceding experiment, it is consistent and becomes more obvious with longer annealing times. The increased loss of interstitials shows that the TiSi<sub>2</sub> film is enhancing the dissolution of the loops. Note that the loss of interstitials is greater in the 890°C samples than the 840°C samples. The four hour 890°C anneal result is attributed to measurement error. The trend of continuing enhanced dissolution in the samples with a TiSi<sub>2</sub> film is apparent.

By assuming that a flux of vacancies from the TiSi<sub>2</sub> film is completely captured and annihilated by the loops, a value for the CyD<sub>v</sub> product is derived by using equation 4.3 and the previously discussed assumptions. The values for  $\Phi$  are given by:

$$\Phi = \frac{\text{interstitials}_{\text{loops}}^{\text{TiSi}_2} - \text{interstitials}_{\text{loops}}^{\text{no film}}}{\text{time}} \quad (4.4)$$

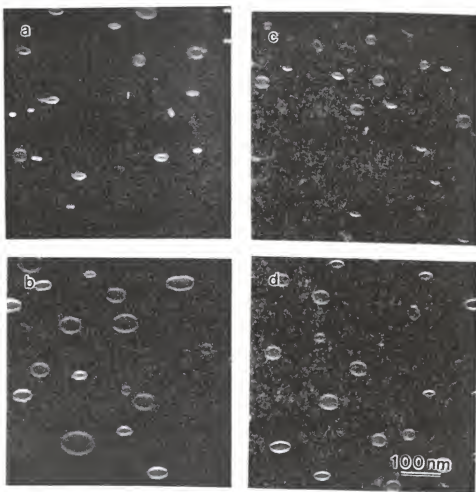


Figure 4.14 Plan view TEM (weak beam dark field,  $g_{220}$ ) micrographs of the loops annealed at various times. (a) no film, 890°C/1 hr/forming gas; (b) no film, 890°C/4 hrs/forming gas; (c) TiSi<sub>2</sub> film, 890°C/1 hr/forming gas; and (d) TiSi<sub>2</sub> film, 890°C/4 hrs/forming gas.

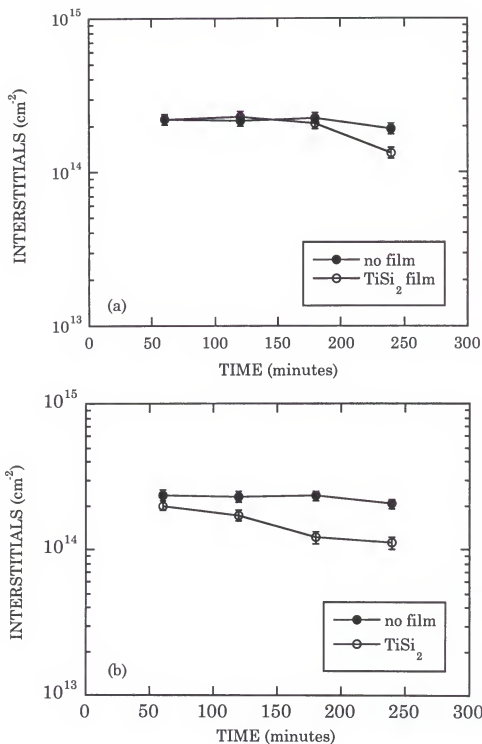


Figure 4.15. Net interstitials bound by the loops annealed at (a) 840°C; and (b) 890°C.

The integrated  $\Phi$  values are listed in Table 4.3. Since the 840°C one and two hour anneals did not show a loss of interstitials, those samples are not considered. The greater dissolution of the loops in the 890°C annealed samples is explained by the larger  $D_V$  value.

Table 4.3. Comparison of point defect values in silicon annealed with a TiSi<sub>2</sub> film measured by the loop method and antimony diffusion.

	890°C (60 min)
$\int_0^d \Phi dx$ (this study)	$(1.1 \pm 1.2) \times 10^5 \left( \frac{\text{vac}}{\text{cm} \cdot \text{sec}} \right)$
$C_V^* D_V$ (ref. 7)	$1.0 \times 10^5 \left( \frac{\text{vac}}{\text{cm} \cdot \text{sec}} \right)$
$\frac{C_V}{C_V^*}$ (Sb diff.)	$1.3 \pm 0.2$
$\frac{C_V}{C_V^*}$ (loops)	$2.1 \pm 1.2$

By again using Tan and Gösele's<sup>7</sup> estimates for the  $C_V^* D_V$  product, the relative vacancy supersaturations are extracted and shown in figure 4.16. These again show good agreement with the results of chapter three using antimony diffusion (Table 4.3). Similar to SIMS measurements, it is expected that the shorter anneal time and lower anneal temperature samples will result in less accurate measurements because of the smaller vacancy flux measured by loop dissolution, which probably accounts for the larger  $\frac{C_V}{C_V^*}$  values measured at 840°C by the loop method. It is noted that in chapter three, the samples received a single anneal, whereas in this study, the samples are first annealed at a lower temperature to form the silicide and

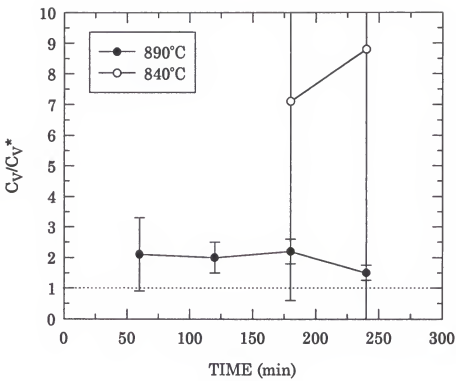


Figure 4.16. Extracted  $C_V/C_V^*$  values by the loop method in silicon with 30 nm titanium annealed for various times and temperatures in forming gas.

then given a higher temperature anneal. Cross sectional TEM showed the morphology of the films to be the same in both cases.

This accelerated dislocation loop dissolution is in broad agreement with the results of earlier loop studies.<sup>50-52</sup> Complete elimination of the loops was not observed in any of the samples. The continued loss of interstitials from loops in the silicided samples at 890°C with time indicates that the non equilibrium point defect flux from the TiSi<sub>2</sub>/Si interface is at least partially continuous long after TiSi<sub>2</sub> growth is complete, which again indicates that the presence of the film and not its growth alters the point defect population. This is in agreement with the results of chapter three, section 5, where the enhancement in antimony diffusivity was inconsistent with a "pulse" of vacancies created at growth.

#### 4.5 Conclusion

By forming an extrinsic dislocation loop layer in antimony doping superlattices and annealing in NH<sub>3</sub>, it was shown that the loops effectively capture most of the vacancies produced by the resulting silicon nitride film. This indicates that vacancy/extrinsic dislocation loop interaction in silicon are diffusion limited and not reaction rate limited. Accelerated dislocation loop dissolution in silicon annealed in NH<sub>3</sub> or with a TiSi<sub>2</sub> film was also studied. Extracted  $\frac{C_V}{C_V^*}$  values by the loop method showed good agreement with earlier measurements made by antimony diffusion.

## CHAPTER 5

### CONCLUSIONS AND FUTURE WORK

#### 5.1 Conclusions

In order to maintain the pace of decreasing device dimensions in silicon microelectronics, the semiconductor manufacturing industry must be able to accurately predict and control dopant diffusion. Dopant diffusion can be understood only with a thorough knowledge of the point defect population in silicon, as well as the sources and sinks of point defects with each processing step. A better understanding of the mechanisms of point defect perturbances will allow the development of physically-based computer models that will be truly predictive.

This dissertation has focussed on two point defect phenomena: dopant diffusion and enhanced extrinsic dislocation loop dissolution in silicon annealed with a  $\text{TiSi}_2$  film. Titanium disilicide films are the most commonly used ohmic contacts in advanced silicon MOSFET devices. Since the silicidation reaction anneal is the final step in "front end processing" and the film is in intimate contact with the highly doped source and drain regions of the device, the film's effect on point defects is of both practical and scientific interest. The study of extrinsic dislocation loops provides another method to study point defects, and, in this case, can verify and complement the information from dopant diffusion.

### 5.1.1 Mechanisms of Point Defect Generation in Silicon with a TiSi<sub>2</sub> Film

In chapter three, the effects of the growth and anneal of TiSi<sub>2</sub> films on dopant diffusion were studied. By annealing titanium films on silicon doping superlattices for 800, 840, or 890°C/1 hour/forming gas, TiSi<sub>2</sub> films were formed. By measuring enhanced antimony diffusion and retarded boron diffusion, it was established that a vacancy supersaturation and interstitial undersaturation were caused by the presence of the film. After a 840°C/1 hour/forming gas anneal of 30 nm of titanium on silicon, a vacancy supersaturation of  $\frac{C_V}{C_V^*} \sim 1.5$  and  $\frac{C_I}{C_I^*} \sim 0.3$  was measured in the underlying silicon substrate. It was found that SIMS depth profile artifacts caused by sputtering through the rough silicide/silicon interface could explain earlier reports of "anomalous" diffusion results in silicon with a silicide film. This problem was avoided in this work by chemo-mechanically polishing the silicon surface prior to SIMS analysis.

Three proposed mechanisms of how a TiSi<sub>2</sub> film effects this point defect perturbation were tested experimentally. The possibility that volume contraction at the TiSi<sub>2</sub>/Si interface is the mechanism for the vacancy supersaturation was tested by annealing antimony doping superlattices with 30 nm of titanium for 800°C/15, 60, or 600 minutes/argon. The volume contraction mechanism requires that the vacancy supersaturation be injected as a "pulse" during film growth, which is complete in less than one minute at 800°C. This should result in a strong time and depth dependence of enhanced antimony diffusion (i.e. the shallowest doping spikes should show greater diffusion than the deeper ones), which was not observed experimentally. The

same dependence, to a lesser degree, would have been observed with the temperature variation (800-890°C), and this was not.

Stress compensation in the substrate was tested by annealing different thicknesses of titanium, ranging from 4 to 312 nm, on antimony and boron doping superlattices for 850°C/1 hour/argon. The range of  $\text{TiSi}_2$  film thicknesses produced imposed a range of substrate stresses during the anneal via mismatches in the coefficient of thermal expansion mismatches between the film and substrate. If lattice compression in the substrate was relieved by a vacancy supersaturation, the enhancement in antimony diffusion should be proportional to the substrate stress, and therefore film thickness. Since this was not observed experimentally, stress compensation in the substrate was discarded as a mechanism for the point defect generation. The drastic difference in morphology of the thinnest films (~10 nm) vs. thickest (~780 nm) and short time anneals (15 minutes) vs. longer anneals (600 minutes) implies that the observed vacancy supersaturation is more related to the intrinsic property of the  $\text{TiSi}_2/\text{Si}$  interface than film growth and morphology.

The diffusing species mechanism holds that if an efflux of silicon into titanium is required for film growth, the diffusing silicon atoms must leave behind vacancies in the substrate. The diffusion of cobalt into silicon during  $\text{CoSi}_2$  formation should then result in an interstitial supersaturation from silicon atoms being knocked off lattice sites by the metal. This mechanism was tested by depositing  $\text{Ti} + \text{Si}$  and  $\text{Co} + \text{Si}$  on antimony and boron doping superlattices and annealing 850°C/1 hour/forming gas to form  $\text{TiSi}_2$  and  $\text{CoSi}_2$ , respectively. Since the precursor phases of  $\text{TiSi}_2$  as well as  $\text{TiSi}_2$  itself form by silicon diffusion,  $\text{TiSi}_2$  formed from co-deposited  $\text{TiSi}_x$  with  $x = 0$  and  $x = 0.8$  should form completely by silicon diffusion, leaving vacancies in the silicon substrate, as actually observed. However, for  $x = 2.2$ , no silicon from

the substrate is consumed by the reaction, hence the point defect concentrations in the substrate should remain unchanged. The formation of  $\text{CoSi}_2$  starting from  $\text{CoSi}_{0.8}$  should be dominated by cobalt diffusion with a smaller amount of silicon diffusion. The magnitude of the point defect perturbation was approximately the same for all samples indicating that this is not the mechanism. It also reinforces the notion that growth of the film from the reaction of titanium + silicon is not a primary factor in the point defect perturbation.

### 5.1.2 Extrinsic Dislocation Loop Behavior in Silicon with a $\text{SiN}_x$ or $\text{TiSi}_2$ Film

In chapter four, the effect of  $\text{SiN}_x$  and  $\text{TiSi}_2$  thin films on pre-existing extrinsic dislocation loops in silicon was examined. It was established that there was no significant barrier to vacancy/loop reactions. This was shown by forming a loop layer in between two antimony doping spikes of a superlattice and then measuring enhanced diffusion in the spikes after an anneal in  $\text{NH}_3$ , which forms a  $\text{SiN}_x$  film on the silicon. Since a large enhancement was observed in the spike in between the film and loop layer and a much smaller enhancement was observed in the deeper spikes below the loop layer, most of the vacancies had reacted with the loops.

Loop behavior was then examined quantitatively analyzing PTEM micrographs after annealing in  $\text{NH}_3$  (nitride forming) or argon environments. Formation and anneal of a  $\text{SiN}_x$  film on silicon that has a pre-existing layer of extrinsic dislocation loops from a previous ion implantation and anneal results in enhanced dissolution of the loops compared to loop samples annealed in argon. By assuming that enhanced loop dissolution is due to recombination with the supersaturation of vacancies, a vacancy

supersaturation of  $\frac{C_V}{C_V^*} = 4.2$  after a 910°C/1 hr/NH<sub>3</sub> anneal was measured.

This shows excellent agreement with the vacancy supersaturation estimate of  $\frac{C_V}{C_V^*} = 3.8$  measured by antimony diffusion in doping superlattices.

Formation and annealing of a TiSi<sub>2</sub> film on silicon that has a layer of extrinsic dislocation loops from previous ion implantation results in enhanced dissolution of the loops compared to silicon without a TiSi<sub>2</sub> film. The continued enhanced dissolution of the loops with time at annealing temperatures indicates that the point defect perturbation at the TiSi<sub>2</sub>/Si interface is at least partially continuous with time, in agreement with the results of chapter three. The extracted value of the vacancy supersaturation,  $\frac{C_V}{C_V^*} = 2.2$  after 890°C/1 hr/forming gas anneal, is in good agreement with the

estimate by enhanced antimony diffusion in chapter three.

## 5.2 Future Work

This work has definitively established how annealing silicon with a TiSi<sub>2</sub> film affects point defect equilibrium. It has also examined three proposed mechanisms for how this perturbation is accomplished. All of them proved not to be a primary mechanism. While this exploration has had a value unto itself, namely, it prevents further propagation of false theories and provides some insight into more plausible mechanisms, discovery of the mechanism by which a TiSi<sub>2</sub> film perturbs native point defect equilibrium in the underlying silicon substrate remains a valuable goal of research. Several areas of further work are briefly discussed here.

### (1) Extended defects in the film as source of point defects

A potential area of experimental interest is the changing morphology and/or composition of the film. While it was noted that the type and degree of the point defect perturbation did not seem to vary with the varying degree of islanding in the film, it is possible that this continuing evolution of the film morphology may be a mechanism of the point defect perturbation in a more subtle, indirect manner. An interface that shows increased roughening with time leading to islanding with time means that there is significant change in the film. Though the diffusion of the film elements was eliminated as a source of point defects, extended defects within the film that terminate at the film/crystal interface could be a source or sink of point defects.<sup>104</sup> Threading dislocations, twin boundaries, and grain boundary triple points, all of which move and change as the film changes macroscopically could be the source of a continuous point defect perturbation. Their evolution or dissolution with annealing time could be a source of point defect generation in the substrate in the defects terminate or continue through the interface. Though it is not possible to grow  $TiSi_2$  epitaxially on silicon because of the different crystal structures, it is possible to grow  $CoSi_2$  epitaxially. It was established in chapter three that growth and anneal of  $CoSi_2$  films result in a vacancy supersaturation and interstitial undersaturation of the same magnitude as  $TiSi_2$ . Though the morphology of the  $CoSi_2$  films was not examined in detail in this study, other studies show it to contain extended defects when annealed.<sup>104</sup> If one grows epitaxial single crystal  $CoSi_2$  without extended defects on silicon doping superlattices, one could determine the relative effect of epitaxial defect-free  $CoSi_2$  vs. poly  $CoSi_2$  on native point defects.

#### (2) Native vacancy behavior in silicon amorphized with a silicon implant

The work in this study used a Ge<sup>+</sup> amorphizing implant to study vacancy/dislocation loop interaction. It would be of interest to see if different amorphizing species resulted in the same point defect behavior observed with Ge<sup>+</sup>. It would also be of interest to study diffusion behavior in regrown silicon vs. non amorphized silicon to see if regrowth results in the same population of defects.

#### (3) Dislocation loop behavior in silicon during a vacuum anneal

It has been noted that a vacuum anneal of silicon results in a large interstitial undersaturation and no change in vacancy equilibrium population. This assymetric change in point defect population could allow the study of interstitial undersaturation induced loop dissolution without the complication of a vacancy undersaturation.

#### (4) Two dimensional dopant profiling

While the work in this study used one dimensional profiling, the development of improved resolution two dimensional techniques such as backscattered electron imaging and scanned probe microscopy may allow accurate two dimensional dopant profiling around actual thin film structures as found in devices. This would be of enormous practical as well as theoretical benefit to the point defect community.

## REFERENCES

1. K. Maex, Phys. Tod. **8**, 35 (1995).
2. Semiconductor Industry Association, *The National Technology Roadmap for Semiconductors* (SIA, San Jose, 1995).
3. P.M. Fahey, P.B. Griffin, and J.D. Plummer, Rev. Mod. Phys. **61**, 289 (1989).
4. K.S. Jones, S. Prussin, and E.R. Weber, Appl. Phys. A **45**, 1 (1988).
5. S.M. Hu and S. Schmidt, J. Appl. Phys. **39**, 4272 (1968).
6. P. Fahey, G. Barbuscia, M. Moslehi, and R.W. Dutton, Appl. Phys. Lett. **46**, 784 (1985).
7. T.Y. Tan and U. Gösele, Appl. Phys. A **37**, 1 (1985).
8. H.-J. Gossmann, C.S. Rafferty, H.S. Luftman, F.C. Unterwald, T. Boone, and J.M. Poate, Appl. Phys. Lett. **63**, 639 (1993).
9. M. Fujinami, A. Tsuge, and K. Tanaka, J. Appl. Phys. **79**, 9017 (1996).
10. S. Dannefaer, P. Mascher, and D. Kerr, Phys. Rev. Lett. **56**, 2195 (1986).
11. K. Taniguchi, D.A. Antoniadis, and Y. Matsushita, Appl. Phys. Lett. **42**, 961 (1983).
12. G.B. Bronner and J.D. Plummer, J. of Appl. Phys. **61**, 5286 (1987).
13. C. Boit, F. Lau, and R. Sittig, Appl. Phys. A **50**, 197 (1990).
14. M.E. Law, IEEE Trans. CAD **10**, 1125 (1991).

15. H. Zimmermann and H. Ryssel, *Appl. Phys. A* **55**, 121 (1992).
16. W.T.C. Fang, T.T. Fang, P.B. Griffin, and J.D. Plummer, *Appl. Phys. Lett.* **68**, 2085 (1996).
17. G.W. Rubloff, K. Hofmann, M. Liehr, and D. R. Young, *Phys. Rev. Lett.* **58**, 2379 (1987).
18. H.-J. Gossman, C.S. Rafferty, F.C. Unterwald, T. Boone, T.K. Mogi, M.O. Thompson, and H.S. Luftman, *Appl. Phys. Lett.* **67**, 1558 (1995).
19. P.A. Packan, PhD Thesis, Stanford University, 1991.
20. P.A. Packan and J.D. Plummer, *J. Appl. Phys.* **68**, 4327 (1990).
21. S.T. Ahn, H.W. Kennel, J.D. Plummer, and W.A. Tiller, *J. Appl. Phys.* **64**, 4914 (1988).
22. S.B. Herner, K.S. Jones, H.-J. Gossman, J.M. Poate, and H.S. Luftman, *Appl. Phys. Lett.* **68**, 1687 (1996).
23. K.S. Jones, H.G. Robinson, J. Listebarger, J. Chen, J. Liu, B. Herner, H. Park, M.E. Law, D. Sieloff, and J.A. Slinkman, *Nucl. Instr. Meth. Phys. Res. B* **96**, 196 (1995).
24. D.J. Eaglesham, P.A. Stolk, H.-J. Gossman, and J.M. Poate, *Appl. Phys. Lett.* **65**, 2305 (1994).
25. S. Prussin, D.I. Margolese, and R.N. Tauber, *J. Appl. Phys.* **57**, 180 (1985).
26. O. W. Holland, J. D. Budai, and B. Nielsen, *Phys. Rev. B.*, in press (1996).
27. D.R. Lim, C.S. Rafferty, and F.P. Klemens, *Appl. Phys. Lett.* **67**, 2302 (1995).
28. D. Eaglesham, *Phys. Tod.* **8**, 1 (1995).
29. V. Krishnamoorthy, B. Beaudet, and K.S. Jones, in press.
30. S.M. Hu, *J. Appl. Phys.* **45**, 1567 (1974).

31. W.A. Tiller, *J. Electrochem. Soc.* **138**, 689 (1981).
32. S.T. Dunham, and J.D. Plummer, *J. Appl. Phys.* **59**, 2551 (1986).
33. T.Y. Tan and U. Gösele, *Appl. Phys. Lett.* **39**, 86 (1981).
34. P. Fahey, R.W. Dutton, and M. Moslehi, *Appl. Phys. Lett.* **43**, 683 (1983).
35. K. Osada, Y. Zaitsu, S. Matsumoto, M. Yoshida, E. Arai, and T. Abe, *J. Electrochem. Soc.* **142**, 202 (1995).
36. T.K. Mogi, H.-J. Gossman, D.J. Eaglesham, C.S. Rafferty, H.S. Luftman, F.C. Unterwald, T. Boone, J.M. Poate, and M.O. Thompson, *Proc. Electrochem. Soc. 1995* (The Electrochemical Society), p. 145.
37. K. Maex, *Mat. Sci. Eng. Rep.* **R11**, 53 (1993).
38. H. Jeon, C.A. Sukow, J.W. Honeycutt, G.A. Rozgonyi, and R.J. Nemanich, *J. Appl. Phys.* **71**, 4269 (1992).
39. R.W. Mann, G.L. Miles, T.A. Knotts, D.W. Rakowski, L.A. Clevenger, J.M.E. Harper, F.M. D'Heurle, and C. Cabral, Jr., *Appl. Phys. Lett.* **67**, 3729 (1995).
40. R.T. Tung, *Appl. Phys. Lett.* **68**, 1933 (1996).
41. C.A. Sukow and R.J. Nemanich, *J. Mat. Res.* **9**, 1214 (1994).
42. J.W. Honeycutt and G.A. Rozgonyi, *Appl. Phys. Lett.* **58**, 1302 (1991).
43. C.M. Osburn, T. Brat, D Sharma, D Griffis, S. Corcoran, S. Lin, W.-K. Chu, and N. Parikh, *J. Electrochem. Soc.* **135**, 1490 (1988).
44. H. Jiang, C. M. Osburn, Z.-G. Xiao, G. McGuire, and G. A. Rozgonyi, *J. Electrochem. Soc.* **139**, 211 (1992).
45. M. Wittmer and K.N. Tu, *Phys. Rev. B* **29**, 2010 (1984).
46. T. Brat, C.M. Osburn, T. Finstad, J. Liu, and B. Ellington, *J. Electrochem. Soc.* **133**, 1451 (1986).

47. D.S. Wen, P.L. Smith, C.M. Osburn, and G.A. Rozgonyi, *Appl. Phys. Lett.* **51**, 1182 (1987).
48. D.S. Wen, P. Smith, C. M. Osburn, and G. A. Rozgonyi, *J. Electrochem. Soc.* **136**, 466 (1989).
49. M.H. Wang, W. Lur, H.C. Cheng, and L.J. Chen, *Mat. Res. Soc. Symp. Proc.*, p. 93.
50. W. Lur, J.Y. Cheng, C.H. Chu, M.H. Wang, T.C. Lee, Y.J. Wann, W.Y. Chao, and L.J. Chen, *Nucl. Instr. Meth. Phys. Res.* **B39**, 297 (1989).
51. W. Lur and L.J. Chen, *J. Appl. Phys.* **66**, 3604 (1989).
52. K. Maex, *Appl. Surf. Sci.* **53**, 328 (1991).
53. J.W. Honeycutt, J. Ravi, and G.A. Rozgonyi, *Mat. Res. Soc. Sym. Proc.* **262**, 701 (1992).
54. K.K. Larsen, F.L. Via, S. Lombardo, and V. Raneri, *Appl. Phys. Lett.* **67**, 2931 (1995).
55. S.B. Herner, V. Krishnamoorthy, and K.S. Jones, *Appl. Surf. Sci.*, in press (1996).
56. D. Mathiot, *Appl. Phys. Lett.* **58**, 131 (1991).
57. M. Wittmer, P. Fahey, G.J. Scilla, S.S. Iyer, and M. Tejwani, *Phys. Rev. Lett.* **66**, 632 (1991).
58. R.B. Fair, in *Impurity Doping Processes in Silicon*, edited by F.F.Y. Wang (North holland, Amsterdam, 1981) p.315.
59. J.R. Pfiester, J. R. Pfiester and P. B. Griffin, *Appl. Phys. Lett.* **52**, 471 (1988).
60. J. Liu, MS Thesis, University of Florida, 1994.
61. R.H. Thompson, Jr., V. Krishnamoorthy, J. Liu, and K.S. Jones, *Mat. Res. Soc. Symp. Proc.* **378**, (1995).
62. J.K. Listebarger, K.S. Jones, and J.A. Slinkman, *J. Appl. Phys.* **73**, 4815 (1993).

63. J. K. Listebarger, H.G. Robinson, K.S. Jones, M.E. Law, D.D. Sieloff, J.A. Slinkman, and T.O. Sedgwick, *J. Appl. Phys.* **78**, 2298 (1995).
64. H.-J. Gossman and E.F. Schubert, *Crit. Rev. Sol. St. Mat. Sci.* **18**, 1 (1993).
65. P.A. Stolk, H.-J. Gossman, D.J. Eaglesham, D.C. Jacobson, J.M. Poate, and H.S. Luftman, *Appl. Phys. Lett.* **66**, 568 (1995).
66. H.-J. Gossman, F.C. Unterwald, and H.S. Luftman, *J. Appl. Phys.* **73**, 8237 (1993).
67. H.-J. Gossman, G.H. Gilmer, C.S. Rafferty, F.C. Unterwald, T. Boone, J.M. Poate, H.S. Luftman, and W. Frank, *J. Appl. Phys.* **77**, 1948 (1995).
68. H.-J. Gossman, A.M. Vrendenberg, C.S. Rafferty, H.S. Luftman, F.C. Unterwald, D.C. Jacobson, T. Boone, and J.M. Poate, *J. Appl. Phys.* **74**, 3150 (1993).
69. M.R. Pinto, D.M. Boulin, C.S. Rafferty, R.K. Smith, W.M. Coughran, Jr., I.C. Kizilyali, and M.J. Thoma, *IEDM* **92**, 923 (1992).
70. H.-J. Gossman, P.A. Stolk, D.J. Eaglesham, C.S. Rafferty, and J.M. Poate, *Appl. Phys. Lett.* **67**, 3135 (1995).
71. Phillips High Resolution Diffractometer Instruction Manual, 2nd edition, 1989.
72. A.E. Morgan, E.K. Broadbent, and A.H. Reader, *Mat. Res. Soc. Sym. Proc.* **52**, 279 (1986).
73. S.B. Desu and J.A. Taylor, *J. Am. Ceram. Soc.* **73**, 509 (1990).
74. K.L. Saenger, J.C. Cabral, L.A. Clevenger, R.A. Roy, and S. Wind, *J. Appl. Phys.* **78**, 7040 (1995).
75. N.L. Matthey, M.G. Dowsett, E.H.C. Parker, T.E. Whall, S. Taylor, and J.F. Zhang, *Appl. Phys. Lett.* **57**, 1648 (1990).
76. M. Wittmer, P. Fahey, G.J. Scilla, S.S. Iyer, and M. Tejwani, *Phys. Rev. Lett.* **66**, 632 (1991).

77. M. Wittmer, P. Fahey, J. Cotte, S.S. Iyer, and G.J. Scilla, *Phys. Rev. B* **45**, 11383 (1992).
78. M. Wittmer, P. Fahey, G.J. Scilla, and S.S. Iyer, *Phys. Rev. Lett.* **71**, 948 (1993).
79. P.A. Ronsheim and M. Tejwani, *Phys. Rev. Lett.* **71**, 947 (1993).
80. J.W. Honeycutt, PhD Thesis, North Carolina State University, 1992.
81. A.G. Italyantsev and A. Y. Kuznetsov, *Appl. Surf. Sci.* **73**, 203 (1993).
82. S. P. Murarka, *Silicides for VLSI Applications* (Academic, New York, 1983).
83. T.K. Mogi, H.-J. Gossmann, C.S. Rafferty, H.S. Luftman, F.C. Unterwald, T. Boone, M.O. Thompson, and J.M. Poate, *Mat. Res. Soc. Sym. Proc.* **355**, 157 (1995).
84. V. Svilan, J.M.E. Harper, C.C. Cabral, Jr., and L.A. Clevenger, *Mat. Res. Soc. Sym. Proc.*, (1994).
85. J. Vilms and D. Kerps, *J. Appl. Phys.* **53**, 1536 (1982).
86. Chu, W.K., Lau, S.S., Mayer, J.W., Muller, H., & Tu, K.N., *Thin Solid Films* **25**, 393 (1975).
87. G. J. Van Gurp and C. Lagnereis, *J. Appl. Phys.* **46**, 4301 (1975).
88. Z.G. Xiao, J.W. Honeycutt, and G.A. Rozgonyi, *Mat. Res. Soc. Sym. Proc.* **260**, 429 (1992).
89. P. Fahey and R.W. Dutton, *Appl. Phys. Lett.* **52**, 1092 (1988).
90. R.J. Messier, *J. Vac. Sci. Technol. A* **4**, 490 (1986).
91. J.F. Jongste, F.E. Prins, G.C.A.M. Janssen, and S. Radelaar, *Appl. Surf. Sci.* **38**, 57 (1989).
92. S.P. Murarka and D.B. Fraser, *J. Appl. Phys.* **51**, 350 (1980).
93. Y. Shor and J. Pelleg, *Mat. Res. Soc. Symp. Proc.* **402**, 107 (1996).

94. H. Park, K.S. Jones, and M.E. Law, *J. Electrochem. Soc.* **141**, 759 (1994).
95. A.N. Larsen and P. Krinhej, *Appl. Phys. Lett.* **68**, 2684 (1996).
96. Y. Kim, H. Z. Massoud, and R. B. Fair, *Appl. Phys. Lett.* **53**, 2197 (1988).
97. H. Park and M.E. Law, *J. Appl. Phys.* **72**, 3431 (1992).
98. H. Park, H. Robinson, K. S. Jones, and M. E. Law, *Appl. Phys. Lett.* **65**, 436 (1994).
99. H.S. Chao, P.B. Griffin, and J.D. Plummer, *Appl. Phys. Lett.* **68**, 3570 (1996).
100. B.L. Eyre and D.M. Maher, *Phil. Mag.* **24**, 767 (1971).
101. M.M. Moslehi and K.C. Saraswat, *IEEE Trans. Electron Devices* **ED-32**, 106 (1985).
102. G.Z. Pan, K.N. Tu, and S. Prussin, *Appl. Phys. Lett.* **68**, 1654 (1996).
103. H.-J. Gossmann, C.S. Rafferty, P.A. Stolk, D.J. Eaglesham, G.H. Gilmer, J.M. Poate, H.-H. Vuong, T.K. Mogi, and M.O. Thompson, *Mat. Res. Soc. Sym. Proc.* **389**, 3 (1995).
104. D. J. Eaglesham, R. T. Tung, J. P. Sullivan, and F. Schrey, *Appl. Phys. Lett.* **73**, 4064 (1993).

## BIOGRAPHICAL SKETCH

Brad Herner received his Bachelor of Science degree in materials science and engineering from the University of California at Berkeley in December, 1989. The author then worked as a process engineer with Lockheed Aeronautical Systems Company in Burbank, California, in the development of aluminum alloys for aircraft. He returned to school at the Pennsylvania State University at University Park, where he earned an Master of Science degree in engineering science. His M.S. thesis was on doping and processing of high dielectric constant ceramic materials. He proceeded to the University of Florida where he earned his Doctor of Philosophy in materials science and engineering in December, 1996. He has authored or coauthored 14 scientific publications.

I certify that I have read this study and that in my opinion it conforms to acceptable standards of scholarly presentation and is fully adequate, in scope and quality, as a dissertation for the degree of Doctor of Philosophy.



---

Kevin S. Jones, Chairman  
Associate Professor of Materials  
Science and Engineering

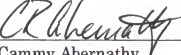
I certify that I have read this study and that in my opinion it conforms to acceptable standards of scholarly presentation and is fully adequate, in scope and quality, as a dissertation for the degree of Doctor of Philosophy.



---

Stephen S. Pearton  
Professor of Materials Science and  
Engineering

I certify that I have read this study and that in my opinion it conforms to acceptable standards of scholarly presentation and is fully adequate, in scope and quality, as a dissertation for the degree of Doctor of Philosophy.



---

Cammy Abernathy  
Professor of Materials Science and  
Engineering

I certify that I have read this study and that in my opinion it conforms to acceptable standards of scholarly presentation and is fully adequate, in scope and quality, as a dissertation for the degree of Doctor of Philosophy.



---

Rajiv Singh  
Associate Professor of Materials  
Science and Engineering

I certify that I have read this study and that in my opinion it conforms to acceptable standards of scholarly presentation and is fully adequate, in scope and quality, as a dissertation for the degree of Doctor of Philosophy.

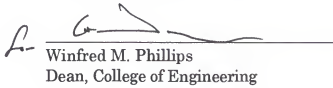


---

Mark E. Law  
Associate Professor of Electrical and  
Computer Engineering

This dissertation was submitted to the Graduate Faculty of the College of Engineering and to the Graduate School and was accepted as partial fulfillment of the requirements for the degree of Doctor of Philosophy.

December 1996



---

Winfred M. Phillips  
Dean, College of Engineering

---

Karen A. Holbrook  
Dean, Graduate School